

**Texas A&M University  
Mechanical Engineering Department  
Turbomachinery Laboratory  
Tribology Group**

**EXPERIMENTAL RESPONSE OF AN OPEN ENDS SFD  
VERSUS A SEALED ENDS SFD**

Research Progress Report to the TAMU Turbomachinery Research  
Consortium

**TRC-SFD-01-2016**

by

**Sung-Hwa Jeung**

Research Assistant

**Luis San Andrés**

Mast-Childs Chair Professor

Principal Investigator

May 2016

**LINEAR-NONLINEAR FORCE COEFFICIENTS FOR SQUEEZE FILM DAMPERS**

TRC Project, TEES #400124-00099

## EXECUTIVE SUMMARY

### EXPERIMENTAL RESPONSE OF AN OPEN ENDS SFD VERSUS A SEALED ENDS SFD

SUNG-HWA JEUNG & LUIS SAN ANDRES, MAY 2016

High performance turbomachinery must endure severe dynamic loads with large amplitude journal motions at the bearing supports. Well-engineered SFDs provide adequate damping to ameliorate rotor vibrations and ensure system reliability. Open ends SFDs have shown to be prone to air ingestion under large amplitude whirl rotor motions and high excitation frequency while demanding of a large flowrate, all undesirable qualities. Piston ring seals are commonly installed in aircraft SFDs to amplify the available damping while reducing the oil through flowrate and avoiding air ingestion.

The experimental work in 2015-2016 investigates the dynamic forced performance of a simple SFD configuration, a single short land ( $L/D=0.2$ ) with 3 orifices ( $\phi=2.5$  mm), its ends either open or sealed, in response to single and sine-sweep frequency dynamic load excitations and impact loads. The test configurations *A* and *B* have clearance 0.254 mm and 0.267 mm, respectively.

The piston ring end seals are effective in reducing side leakage; thus the sealed SFD provides damping coefficient 11-13 times larger and added mass coefficients eleven times larger than those in the open ends configuration. Comparison of force coefficients between two sealed ends dampers differing in seal flow conductance ( $\bar{C}_{seal-1}=0.63\bar{C}_{seal-2}$ ) shows that the tight seal with ~47% larger flow resistance  $\bar{C}_{seal-1}$  provides ~20% larger damping at large orbit amplitude motion  $r/c_A=0.6$  than the sealed ends damper with smaller flow resistance. Upon increasing the lubricant supply pressure four times ( $P_{in-1}\sim 0.69\rightarrow P_{in-2}\sim 2.76$  barg) for the sealed ends SFD with  $\bar{C}_{seal-1}$ , the SFD added mass coefficients show a large increase with increasing orbit amplitude motion  $r$  whereas the SFD direct damping coefficients do not show a significant increase with  $r$ .

Experiments with a sine-sweep frequency dynamic load confirmed findings made in prior measurements, namely SFD force coefficients identities from tests with a low rate of change in excitation frequency ( $\alpha$ ) agree with the coefficients obtained from a single-frequency dynamic load over the same test conditions.

The test system transient responses due to a single impact show the peak amplitude of motion ( $Z_{MAX}$ ) is proportional to the magnitude of applied load ( $F_{MAX}$ ). The identified system damping ratio ( $\zeta$ ) is proportional to the peak dynamic displacement as a system that is linear would show. The sealed ends SFD provides ten to fifteen times larger damping ratio than the open ends configuration.

## Table of Contents

TABLE OF CONTENTS	4
NOMENCLATURE	5
INTRODUCTION	7
LITERATURE REVIEW	9
DESCRIPTION OF THE EXPERIMENTAL FACILITY AND TEST DAMPER	13
FLOW RATE MEASUREMENTS UNDER A STATIC CONDITION	19
DESCRIPTION OF SINGLE FREQUENCY DYNAMIC LOAD	23
SINGLE FREQUENCY DYNAMIC LOAD EXPERIMENTAL RESULTS	28
DESCRIPTION OF SINE-SWEEP FREQUENCY DYNAMIC LOAD TESTS	68
SINE-SWEEP FREQUENCY DYNAMIC LOAD EXPERIMENT RESULTS	75
FURTHER MEASUREMENT: RESPONSE DUE TO SINGLE IMPACT LOAD	81
SINGLE IMPACT LOAD EXPERIMENT RESULTS	84
CONCLUSIONS AND RECOMMENDATIONS	95
ACKNOWLEDGEMENT	97
REFERENCES	97
APPENDIX A. DESCRIPTION OF TEST SYSTEM AND COMPONENTS	100
APPENDIX B. MEASUREMENT OF LUBRICANT PHYSICAL PROPERTIES	103
APPENDIX C. IDENTIFICATION OF (DRY) TEST SYSTEM STRUCTURE PARAMETERS	105
APPENDIX D. UNCERTAINTY IN IDENTIFIED FORCE COEFFICIENTS	107

## Nomenclature

$a_{a(t), (a=X,Y)}$	Acceleration of bearing cartridge [m/s <sup>2</sup> ]
$c$	Nominal radial clearance [ $\mu\text{m}$ ]
$C_{\alpha\beta, (\alpha,\beta=X,Y)}$	SFD damping coefficients [N·s/m]
$C_S$	Dry structure damping coefficient [N·s/m]
$D$	Journal diameter [m]
$e_s$	Static eccentricity (along 45°) [m]
$F_{a(t), (a=X,Y)}$	Components of the applied dynamic load amplitude [N]
$F_s$	Static load [N]
$f$	Excitation frequency [Hz]
$f_n$	Test system natural frequency [Hz]
$f_{start}, f_{end}$	Start and end frequencies for sine-sweep frequency range [Hz]
$H_{\alpha\beta, (\alpha,\beta=X,Y)}$	Measured system complex stiffness [MN/m]
$H$	Lubricant film thickness [ $\mu\text{m}$ ]
$I$	$\sqrt{-1}$ . Imaginary unit
$K_{\alpha\beta, (\alpha,\beta=X,Y)}$	SFD stiffness coefficients [N/m]
$K_S$	Structural support stiffness [N/m]
$L$	Film land length [m]
$M_{\alpha\beta, (\alpha,\beta=X,Y)}$	SFD added mass coefficients [kg]
$M_S$	Dry structure added mass coefficient [kg]
$M_{BC}$	Bearing cartridge mass [kg]
$n$	Number of impacts [-]
$P_{in}$	Static oil pressure at journal inlet [Pa(g)]
$P$	Dynamic pressure in film land [Pa]
$Q_{in}$	Lubricant flow rate [LPM]
$r$	Orbit amplitude [m]
$R$	Journal radius, $R= \frac{1}{2} D$ [m]
$t$	Time [s]
$t_{IMP}$	Typical duration of impact [s]
$T_r$	Force transmissibility ratio [-]
$T^*$	Elapsed time of sine-sweep frequency dynamic load excitation [s]
$\Delta f/\Delta t$	Sweep frequency ramp rate, $(f_{end}-f_{start})/T^*$ [Hz/s]
$X, Y, \bar{X}, \bar{Y}$	Coordinate systems
$x(t), y(t)$	Relative displacement of BC respect to the journal along X and Y direction [m]
$Z_s$	$e_s \cos(\frac{1}{4}\pi)$ . Static displacement along X,Y [m]
$Z_{X,Y}$	Bearing cartridge displacements along X and Y [m]
$Z^{dyn}$	$(Z-Z_s)$ . Dynamic displacement of BC along impact load direction, [m]
$\beta$	Slope of peak dynamic displacement vs. peak load, $\bar{Z}_{MAX}^{dyn}/c$ vs. $\bar{F}_{MAX}/(LD)$ [1/Pa]
$\xi$	Damping ratio [-]
$\delta$	Logarithmic decrement, $2\pi\xi/\sqrt{1-\xi^2}$ [-]
$\rho, \mu$	Oil density [kg/m <sup>3</sup> ] and viscosity [Pa·s]

$\Theta$	Circumferential angular coordinate [rad]
$\omega$	Excitation frequency ( $\omega=2\pi f$ ) [rad/s]

### Vectors and matrices

$\bar{\mathbf{a}}_{(\omega)}$	Vector of accelerations $\{a_{X(\omega)}, a_{Y(\omega)}\}^T$ in the frequency domain [m/s <sup>2</sup> ]
$\mathbf{C}$	Matrix of damping coefficients [N·s/m]
$\mathbf{K}$	Matrix of stiffness coefficients [N/m]
$\bar{\mathbf{F}}_{(\omega)}$	Vector of dynamic loads $\{F_{X(\omega)}, F_{Y(\omega)}\}^T$ in the frequency domain [N]
$\bar{\mathbf{H}}_{(\omega)}$	$\mathbf{K} - \omega^2\mathbf{M} + i\omega\mathbf{C}$ Matrix of dynamic stiffness coefficients in the frequency domain [N/m]
$\mathbf{M}$	Matrix of added mass coefficients [kg]
$\bar{\mathbf{z}}_{(\omega)}$	Vector of relative displacements $\{x_{(\omega)}, y_{(\omega)}\}^T$ in the frequency domain [m]

### Subscripts

BC	Bearing cartridge
CCW	Counter-clockwise
CW	Clockwise
$L$	Lubricated system
$S$	Structure
$s$	Static

### Acronyms

DAQ	Data acquisition
DFT	Discrete Fourier Transform
FRF	Frequency Response Function
SFD	Squeeze Film Damper

## Introduction

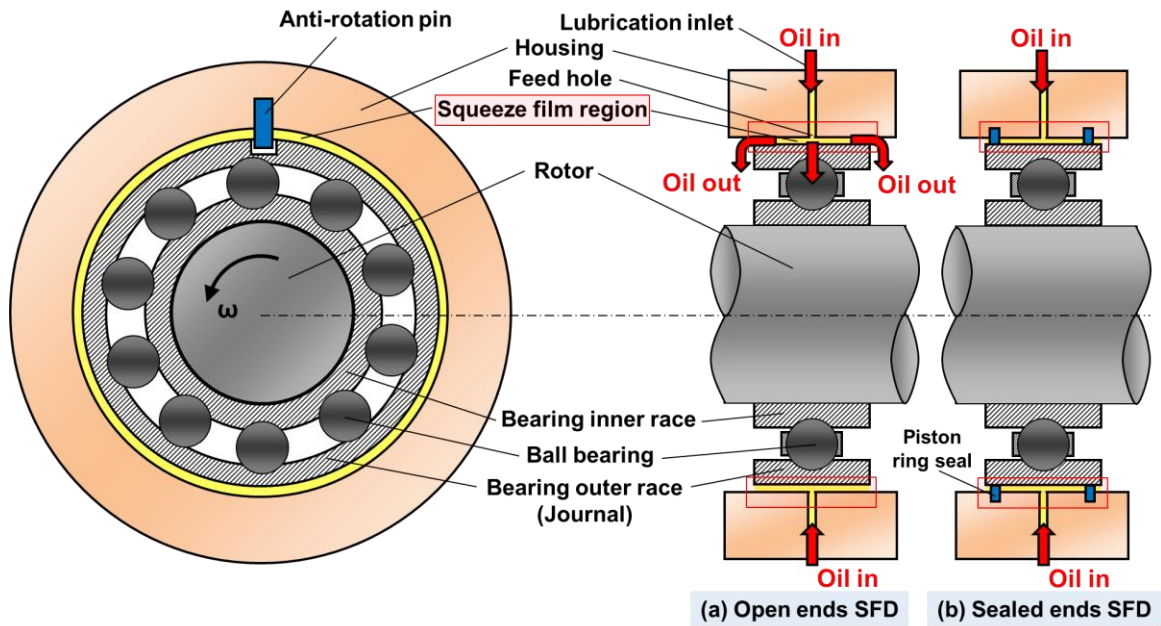
With higher power density and improved efficiency, modern rotating machinery operate at increasingly higher rotational speeds. As a result, bearing supports experience large dynamic loads and must withstand significant large amplitude motions. A Squeeze Film Damper (SFD) aids to reduce rotor synchronous vibration response as the system crosses its critical speeds. Thus, aircraft engines and high-speed compressors implement SFDs to dissipate mechanical energy produced by rotor motion; and along with a flexible support, lead to lower transmitted forces [1,2].

Figure 1 depicts schematic views of an open ends SFD and a sealed ends SFD, both in series with a ball bearing supported rotor. The annular gap between the two cylinders (housing and outer race of ball bearing) contains the film of lubricant that is squeezed during operation. An anti-rotation pin or a squirrel cage prevents the outer race of ball bearing from rotating. Unlike a journal bearing, SFDs do not rotate, but whirl (or precess) in response to rotor vibrations and squeeze the film land to generate a hydrodynamic pressure [1]. A SFD with its journal whirling with frequency  $\omega$  and amplitude  $r$  produces twice a reaction force that for a hydrodynamic journal bearing with its journal spinning with angular speed  $\Omega = \omega$  and static eccentricity  $e = r$ . The generation of a large hydrodynamic pressure uniquely distinguishes the forced performance of SFDs from that of a simple hydrodynamic journal bearing [3].

The forced performance of SFDs depends largely upon the damper geometry, lubricant viscosity, supply and operating conditions, and sealing devices (piston ring and O-ring) among other factors. There are unlimited feasible geometric configurations of SFDs and thus numerous researchers have poured countless efforts to determine the characteristics and forced performance of various SFDs. Traditionally, SFDs configured with a central feed groove have been profusely investigated [4]. Presently the need of a simpler SFD design to save space and weight in aircraft engines has led to research in ultra-short SFDs; that is, damper with length to diameter ratio  $L/D=0.2$  or less [3,5,6].

Compared to SFDs with the circumferential feeding groove arrangement, dampers with orifice feed holes impinging directly into the film land simplify SFD design and save space and weight. This feed mechanism in SFDs, however, is prone to air ingestion

when undergoing large amplitude journal motions during dynamic operation [3]. Air entrainment, which degrades the damping force by preventing the generation of squeeze film pressure, can be substantially reduced by installing sealing devices such as piston ring seals or O-rings at the end of the film lands (see Figure 1(b)). Note that O-rings have a temperature limit of 130°C and thus aircraft engines do not use them. Installation of piston ring end seals not only prevents air entrainment, but also amplifies the damping capability of SFD with and lowers the required lubricant flow rate [4].



**Figure 1. Schematic views of hole-fed SFDs with: (a) open ends and (b) sealed ends [1].**

Jet engines inevitably experience arduous transient events due to maneuver loads and sudden shock loads such as during hard landings and takeoffs. During these transient events, the engine support structure is subjected to too large transmitted forces that could over time foster fatigue on the centralizing spring (squirrel cage) of a SFD. Adequate damping to ameliorate rotor vibrations is paramount to ensure system integrity and reliability. Certifying the reliable operation of turbomachinery calls for a detailed characterization of SFD forced performance under these stringent operating conditions.

The present work extend prior research [3,5-7] on short length SFDs ( $L/D=0.2$ ) configured with feed holes and present an experimental analysis of open and sealed ends

SFDs, respectively. Comprehensive dynamic load tests on the SFD will allow characterization of the forced performance of the SFD not only undergoing circular whirl motions, but also in response to various arduous transient event such as in hard landings and takeoffs. Full detail of the experimental results and test dampers' geometry will serve as benchmark test data and will advance the knowledge of SFDs.

## Literature review

The following literature review covers sealed end SFDs and SFDs undergoing transient dynamic loads.

### *Sealed ends SFDs*

Industry demands well-engineered SFDs with a low footprint to reduce cost, maintenance, weight, and space while pushing for higher operating shaft speeds to increase power output. While open ends SFDs are prone to air ingestion under specific operating conditions, e.g., large amplitude whirl motion and high excitation frequency while demanding of a large through flowrate [8]. End seals amplify the available damping while reducing the flowrate and reducing air ingestion.

Piston ring seals, end plates and O-rings are commonly used to seal the SFD which increases the damping capability of SFDs while using less lubricant supply. Levesley and Holmes [9] compare experimentally the performance of sealed ends SFDs with different sealing arrangements, in particular with a piston ring seal and an end plate seal. The authors reveal that the piston ring seals provide a larger damping than does the end plate seal. The performance of sealed ends SFD is largely dependent on the seal conductance, which is the inverse of the hydraulic resistance ( $1/R$ ), and must be empirically determined. In general, the SFD direct and added mass coefficients increase with decreasing side leakage and clearance gap of a sealing device [10], yet, a too tightly sealed SFD may lock the rotor bearing system and rendering a SFD ineffective [4].

Miyachi et al. [11] present the experimental SFD damping coefficients for damper with various seal configurations, i.e., O-ring seal, piston ring seal, and simple side seal. With increasing lubricant supply pressure from 1 bar(g) to 4 bar(g), the damping coefficients increase twofold for the piston ring sealed SFD while those of O-ring sealed

SFD do not show a significant difference. This difference may be due to the difference in flow resistant of each seal, however, the value is not specified.

De Santiago and San Andrés [12] evaluate the damping coefficients of an end plate sealed integral SFD (ISFD) supporting an imbalanced rotor. The ISFD damping coefficients are determined from the synchronous rotor amplitude motion at the first critical speed with differing various imbalances. A tightly sealed ISFD with seal clearance of 0.076 mm offers a minimal increase in the damping coefficients compared to an ISFD with seal gap of 0.127 mm. This was explained by the fact that a larger restriction of the leakage results in an increasing lubricant temperature that lowers the oil viscosity.

Arghir and Defaye [13] investigate the SFD radial and tangential forces for sealed ends damper with two types of piston ring seals. The first pair of piston ring consists of one slit while the second pair has seven openings circumferentially. The second type of piston rings leaks 3.1 times more than those of first pair with only one slit. Note that leakage flow evacuates heat generation by the squeeze effect. The piston ring sealed damper with seven openings at each end eliminates the hydrostatic effect caused by a localized leakage which results in ~20% decrease of tangential force than those with one slit.

Meng et al. [14] present experimentally the trend of serrated piston ring sealed SFD tangential (damping) force and radial (inertia) force versus lubricant supply pressure and versus lubricant temperature. The serrated piston ring consists of a number of minute dent-like grooves ( $r_g=0.79$  mm) spaced  $5^\circ$  apart along the circumference of a ring. These small grooves allow a sufficient amount of lubricant flow. With increasing supply pressure, tangential and radial forces increase. With oil temperature rise, tangential force increases somewhat. The authors' further note that the partially sealed SFD is more prone to oil cavitation than an open ends SFD by trapping the air bubbles in the damper land, which leads to a smaller generation of tangential (damping) forces.

Recently, San Andrés and Seshagiri [15] experimentally quantify the dynamic forced performance of piston ring sealed SFD with a central feed groove. The test results are thoroughly correlated with those of an identical damper with open ends [16]. As expected, the piston ring seals effectively increase the pressure in the film lands by

restricting the oil leakage. Subsequently, the sealed end SFD produces more than twice the amount of SFD damping and inertia than those from the open ends SFD. The experimental identified SFD force coefficients are compared against the prediction [7] using an empirically determined seal end flow conductance. Experimental and predicted SFD coefficients match closely when also accounting for the effective groove depth as in Refs. [17,18].

### ***SFDs undergoing transient dynamic loads***

Researchers have studied the forced response of a SFD subjected to (sudden) transient events. In general, these studies can be categorized by the source of the excitation; that is, by a transient event due to the unbalance response of a rotor, in particular for a blade loss event [19-23]; or by the movements of bearing support bases, especially for a seismic excitation or impact loads [6,24-28].

Refs. [19-22], deliver relevant numerical studies that characterize the transient nonlinear response of an aero-engine experiencing a blade loss event. Only a few works [19-21], however, have further validated the studies against experimental data. These experimental studies show that an increasing unbalance force could lead to a large transmissibility ( $T_r > 1$ ), rendering the SFD ineffective and leading to premature bearing failure. In Ref.[21], increasing the oil supply pressure to a sealed ends SFD from 3.4 bar to 5.5 bar reduces substantially the amplitude motion of the rotor.

San Andrés et al. [23] present measurements of an open ends SFD dynamic performance for a transient event with sine-sweep frequency at a constant angular acceleration. Identified SFD force coefficients from a sine-sweep frequency dynamic load with a low angular acceleration ( $\alpha = 6.5$  Hz/s) show a good agreement with those from a single-frequency dynamic load over the same test conditions. The same cannot be said, however, for coefficients identified from a dynamic load with too fast angular acceleration. This is because a too-fast change in frequency prevents the system from achieving a quasi-steady-state response at a discrete or particular frequency, hence the system does not displace as needed for the accurate calculation of complex stiffnesses in the frequency domain.

Hori and Kato [24] study the seismic response of a turbomachine in an effort to answer the major question of whether a rotor-bearing support can withstand an earthquake, another example of a transient load. Roberts et al. [25,26] utilize a linear model of the squeeze-film to determine the SFD force coefficients, damping and inertia, from a freely decaying transient response experimental data. The damping and inertial coefficients are validated against the predictions and found to be independent of a frequency of vibration.

Lee et al. [27] demonstrate both analytically and experimentally that a transient response of the rotor-bearing system is sensitive to the time duration of an external shock. These numerical analyses gauge the robustness of rotating machinery withstanding an external shock.

Most recently, San Andrés and Jeung [6,28] performed measurements of the transient response of a single-land open ends SFD due to large impact loads. The measurements show that a large change in speed ( $a_r \gg 0$ ) induces large fluid inertia force comparable to the purely viscous force with increasing impact loads. A large increase in SFD inertia coefficients ( $M$ ) leads to a moderate increase in the test system damping ratio since  $\xi \sim C/M$ . Interestingly enough, Ref.[28] shows experimentally that the presence of fluid inertia tends to reduce the peak system dynamic response.

## Description of the Experimental Facility and Test Damper

Figure 2 shows a photograph and a top view schematic of the current SFD test rig assembly. The test rig consists of three main components: a SFD test bearing, two electromagnetic shakers and a hydraulic static loader. The two orthogonally placed shakers and the static loader,  $45^\circ$  away from each shaker, are firmly mounted on an iron table. The static loader enables displacement of the BC to various static eccentricity conditions while the shakers, via slender stingers connected BC, enable dynamic displacement of the BC.

Figure 3 shows the main components of the SFD test bearing. The SFD support structure consists of flexural rods attached to the BC on one end and attached to the rigid pedestal on the other. The number of rods can be changed to increase or decrease the structural stiffness and serve to replicate a squirrel cage (elastic) support. The actual SFD consists of an interchangeable test journal bolted to the journal base which is itself rigidly fastened to the pedestal. Meanwhile, the annular gap between the outer surface of the test journal and the inner circumference of the BC constitutes the film land. This configuration allows the test journal to be easily exchanged without major variation in the instrumentations. Appendix A details the measurement of the SFD component dimensions.

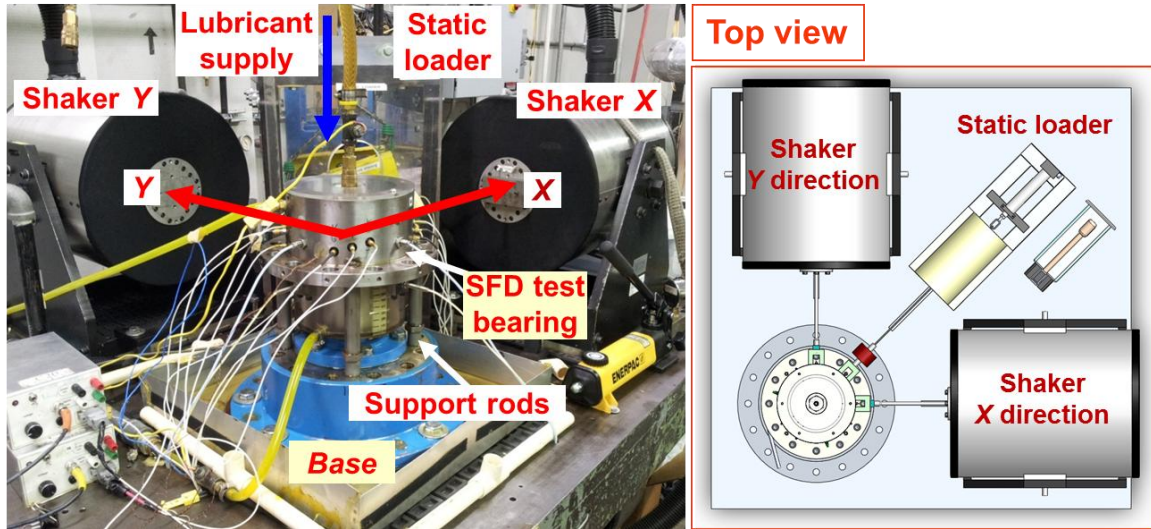


Figure 2. Picture and top view of SFD test rig with electromagnetic shakers and static loader.

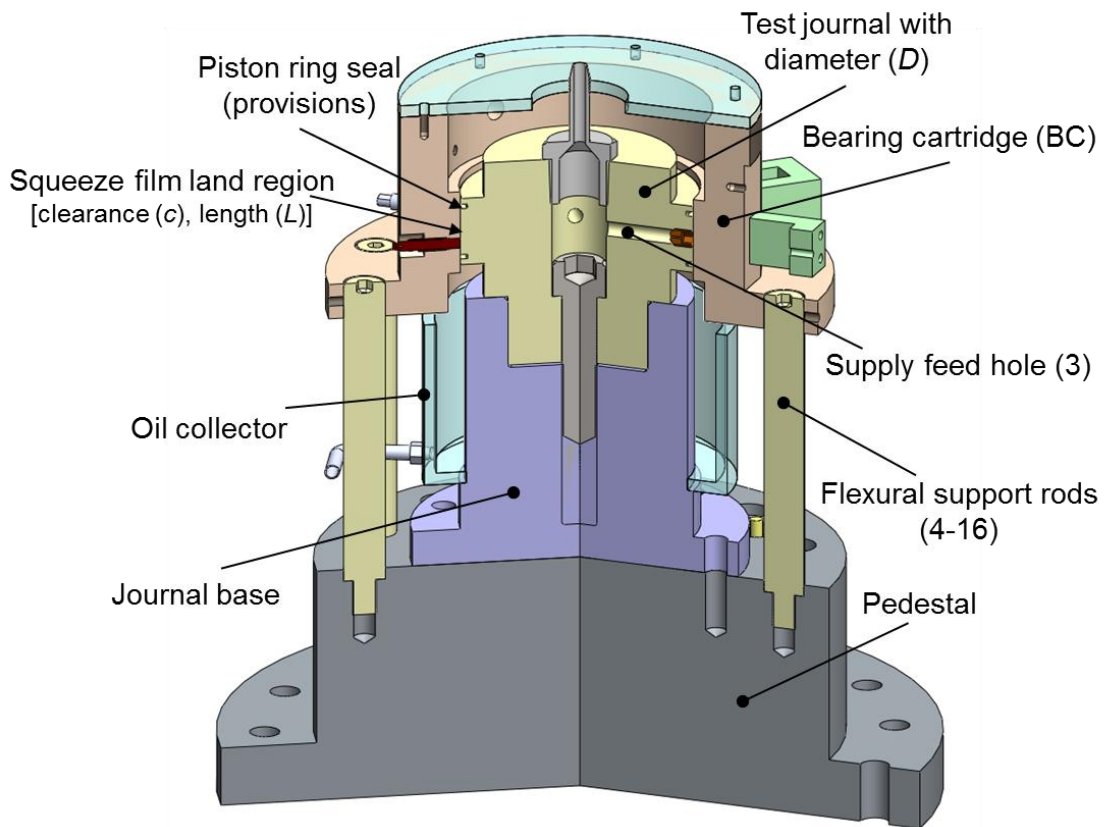


Figure 3. Schematic showing overview of SFD test bearing section (cut-section view). Damper A installed [5].

Figure 4 shows a cross-section view of the SFD test rig with a 127 mm outer diameter journal and also illustrates the path of lubricant flow through the system. Light lubricant, ISO VG2 is supplied into the SFD through a hole in the top of the stationary journal via an external oil pump gear. Oil is forced through three orifices ( $\phi = 2.54$  mm) spaced  $120^\circ$  apart in the journal and flows into the mid axial plane of the squeeze film land ( $z=0$ ). The lubricant exits through the top and bottom ends of the bottom film lands to ambient pressure and discharges to oil collecting chambers. The oil collectors hold the oil and a return pump moves the oil to a reservoir tank where it is recycled through the system. Appendix B presents the measurements of lubricant viscosity versus temperature.

Figure 5 depicts views of test dampers A and B for visual comparison, and Table 1 shows the dimensions of the two test dampers. Note that the nominal radial clearance for dampers A and B is  $c_A = 0.254$  mm (10 mil) and  $c_B = 0.267$  mm (10.5 mil), respectively. The two dampers have the same axial film length  $L = 25.4$  mm (1 in). However, the journal in damper A includes, at the top and bottom sides of the film land, end grooves for installation of piston ring end seals. The end grooves have a width and depth equal to 2.5 mm and 3.8 mm ( $\sim 15c_A$ ), respectively. The end lips have a width equal to 3.3 mm (see inset) and chamfered edges make a small clearance  $\sim 1c_A$  to  $4c_A$  with the BC inner diameter. The total oil wetted length for damper A ( $L_{A-tot}$ ) equals 36.8 mm (1.45 in). Note that the effective film length for open ends damper A,  $L_{eff} = 29.7$  mm, is larger than the design film land length  $L = 25.4$  mm and shorter than the actual wetted length,  $L_{tot} > L_{eff} > L$ . A curve fitting of the measured dynamic pressure profile estimates the effective film land  $L_{eff}$ . See Ref.[5] for details.

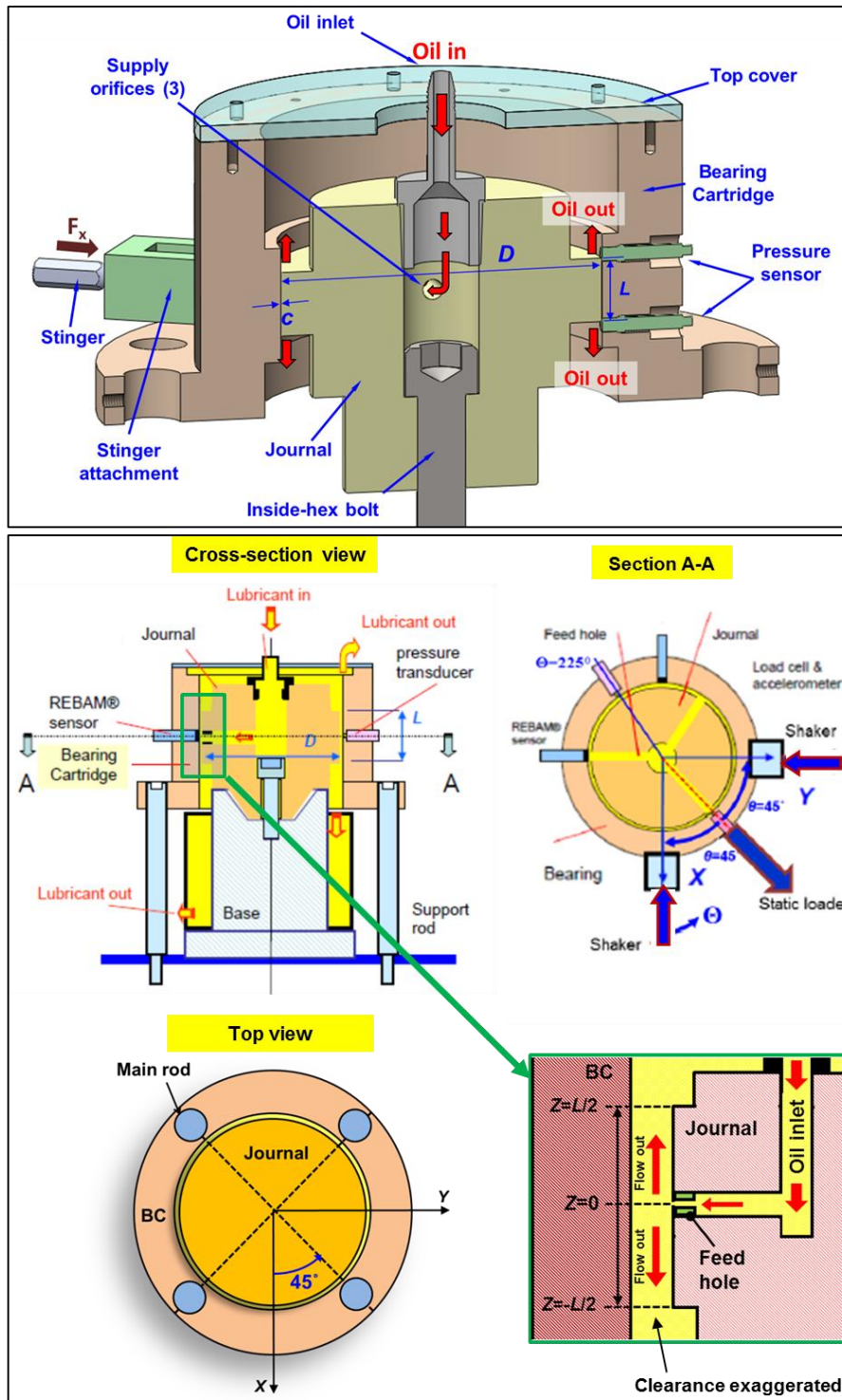


Figure 4. Cross-section view of SFD test section with physical dimensions ( $L=25.4$  mm,  $D=127$  mm,  $c_B=0.267$  mm) and lubricant flow path. Damper B installed.

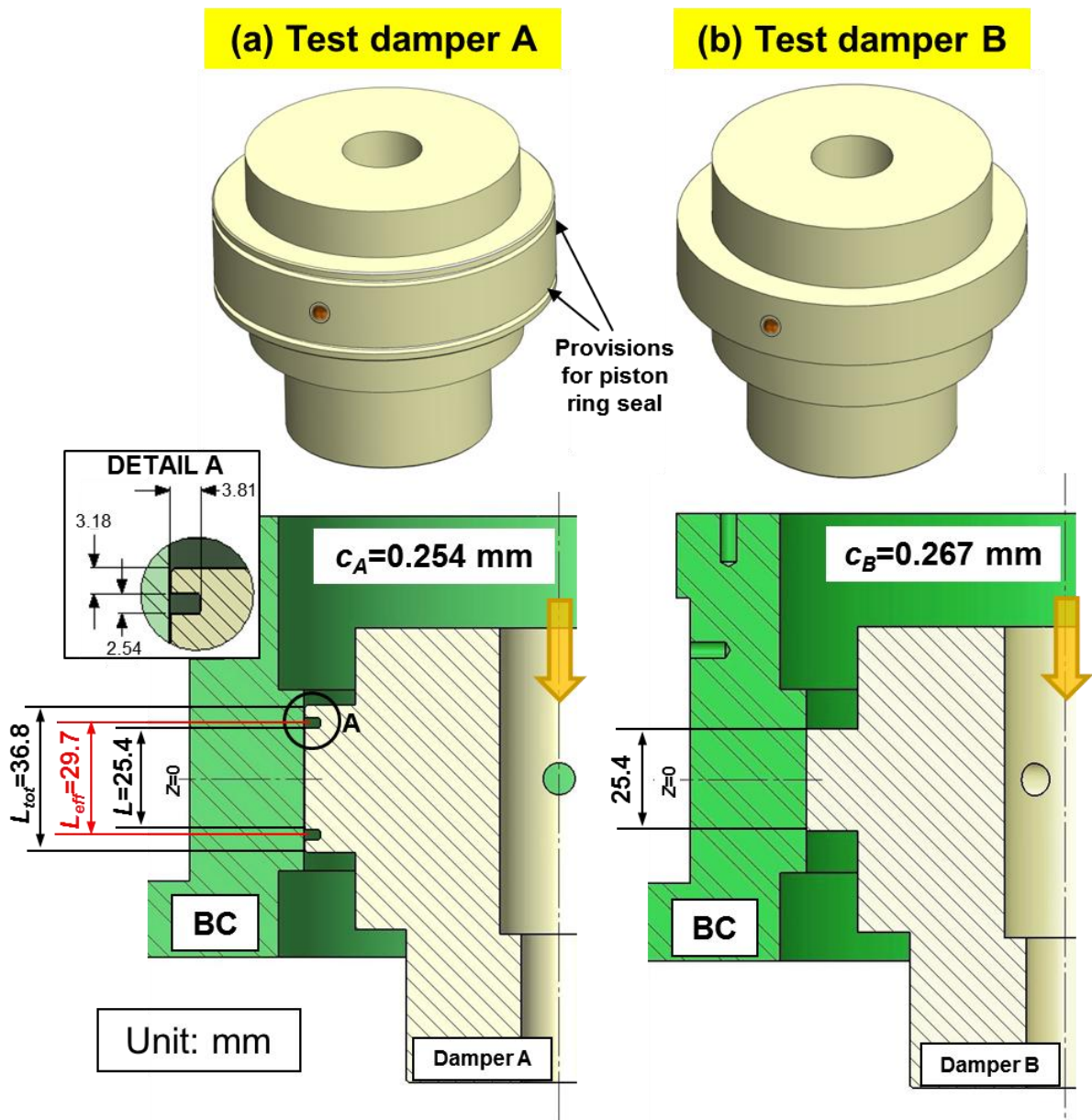
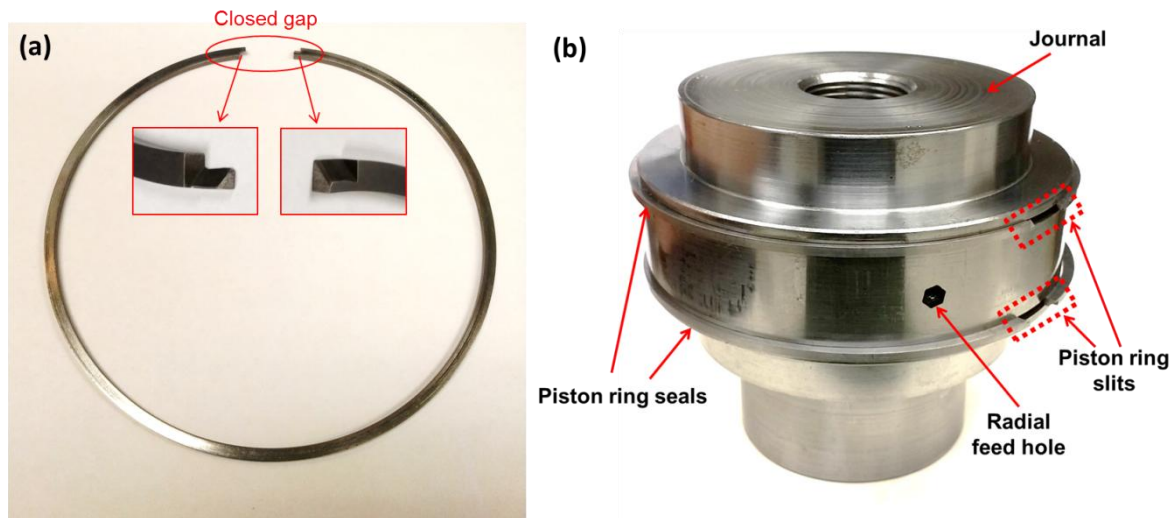


Figure 5. Test damper A ( $c_A=0.254 \text{ mm}$ ) with end grooves for installation of piston rings, and damper B ( $c_B=0.267 \text{ mm}$ ) without end grooves. Film land length 25.4 mm ( $L/D=0.2$ ).

**Table 1. Critical dimensions for test dampers A and B ( $L/D=0.2$ )**

Damper Type	Film land length, $L$ (mm)	Damper diameter, $D$ (mm)	Radial clearance, $c$ (mm)	Ends condition	End Grooves	Groove Width, $L_G$ (mm)	Groove Depth, $D_G$ (mm)
A	25.4	127	0.254	Open, Sealed	Yes	2.5	3.8
B			0.267	Open	No	-	-

Figure 6 shows (a) a piston ring (PR) and (b) the journal with the piston rings installed. The piston rings outer diameter, when closed, equals to the ID of the BC; that is  $127.16 \text{ mm} \pm 0.01 \text{ mm}$ . Note that there exists a radial gap of 0.46 mm between the piston rings ID and the journal end groove OD. Figure 7 shows a schematic view of the installed piston rings and the angular location of the feedholes in the journal. A PR slit is  $60^\circ$  away from adjacent feedholes to minimize the lubricant leakage.



**Figure 6. (a) Photograph of piston ring seal (dimensions are proprietary) and (b) piston ring seals installed in the end grooves of the journal.**

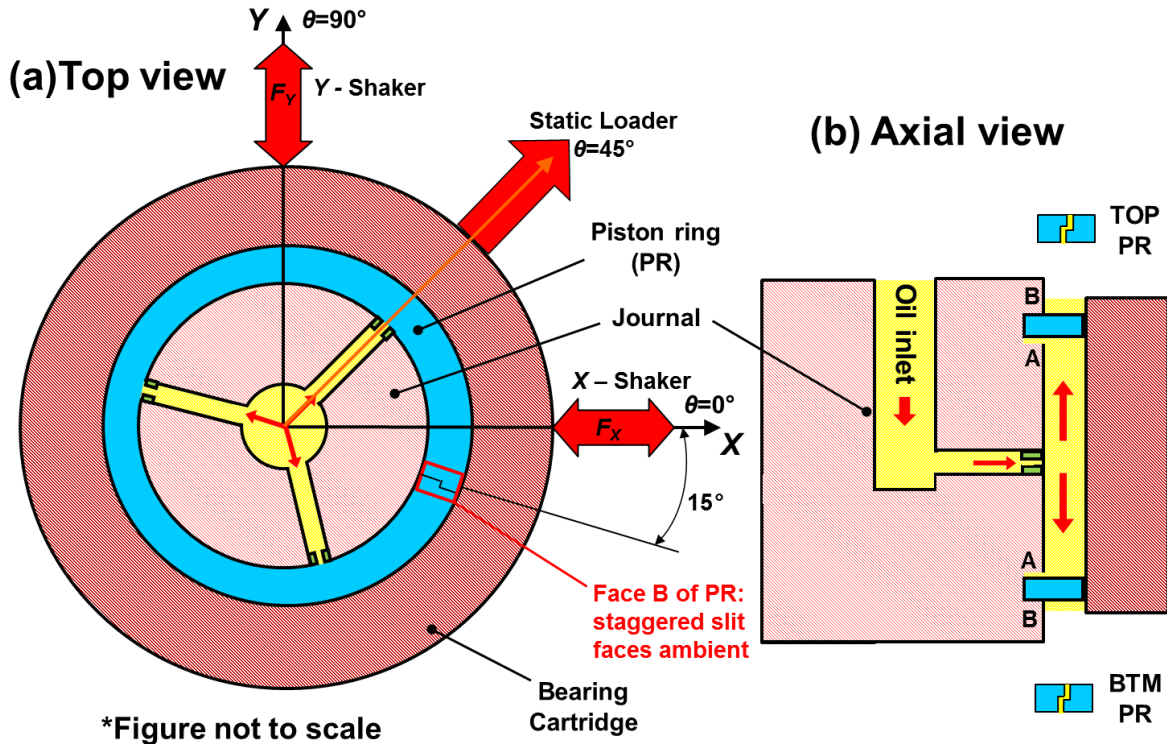


Figure 7. Piston ring (a) circumferential and (b) axial installation orientation.

## Flow Rate Measurements Under a Static Condition

This section presents the characterization of the flow conductance ( $C$ ) for the open ends SFD as well as the flow conductance for the piston rings (PR) in the sealed ends SFD. The sealed ends damper performance depends largely on its flow conductance (later, see Fig. 29).

Figure 8 depicts a hydraulic circuit representing the lubricant flow path and flow resistances ( $R$ ). Lubricant flows into the damper film land through three uniformly spaced orifices with flow resistance ( $R_o$ ). The oil then flows through the top and bottom land sections of the SFD. The journal with 12.7 mm (0.5 inch) film land, above and below the feedholes, has flow resistances,  $R_{TL}$  and  $R_{BL}$ , and the piston rings have flow resistances  $R_{TS}$  and  $R_{BS}$ . Sub-indices  $T$  and  $B$  denote the top and bottom land sections of the damper.

A pressure gauge displays the inlet pressure ( $P_{in}$ ) of the lubricant before it enters the SFD test rig. A flow meter records the inlet flow rate ( $Q_{in}$ ) while the outlet flow rate through the top and bottom sections ( $Q_T$  and  $Q_B$ ) are determined via the time required to

fill a known volume in the oil collector beneath the BC. For a damper with a uniform clearance (BC and journal perfectly centered and aligned), the ratio of bottom land flow to inlet flow must equal 50%,  $Q_B/Q_{in}=0.50$ .

For the top and bottom film land sections, the flow resistance and end seal fluidic resistances ( $R$ ) are in series. Hence, a simple hydraulic analysis gives

$$Q_{in} = \frac{P_{in} - P_s}{(R_o/n)} = Q_T + Q_B \quad (1)$$

$$Q_T = \frac{P_s - P_a}{R_{TL} + R_{TS}} = \frac{P_s}{R_T} = C_T P_s; \quad Q_B = \frac{P_s - P_a}{R_{BL} + R_{BS}} = \frac{P_s}{R_B} = C_B P_{in} = \frac{P_s - P_a}{R_T}$$

Above,  $C_T$  and  $C_B$  denote flow conductances ( $1/C=R$ ) and  $P_a=0$  is ambient pressure.

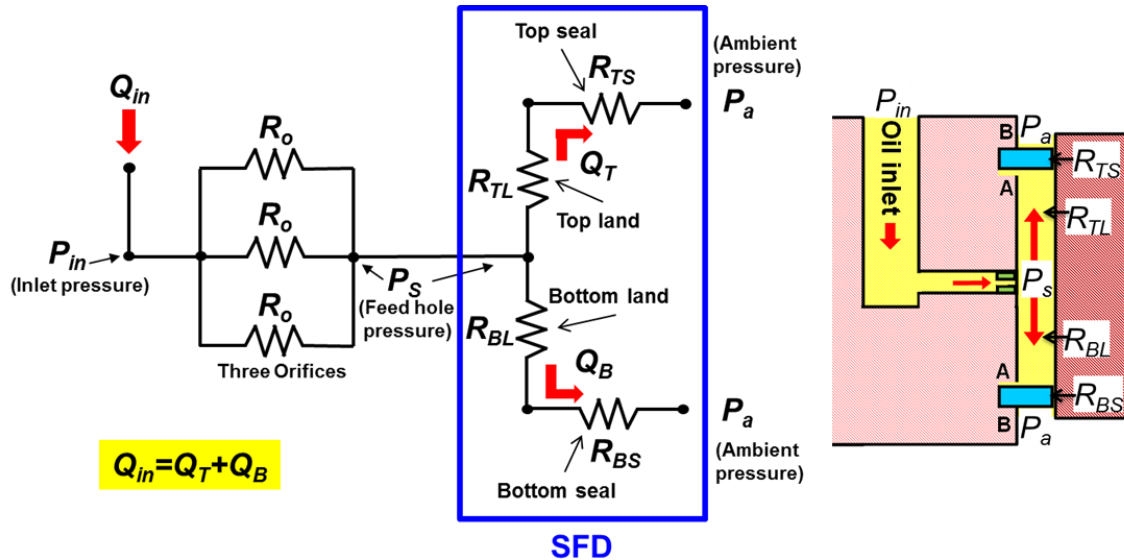


Figure 8. Flow diagram with hydraulic resistances for a sealed ends SFD.

Table 2 lists the recorded inlet pressure ( $P_{in}$ ), supply ( $Q_{in}$ ), top ( $Q_T$ ) and bottom ( $Q_B$ ) flow rates, the ratio  $Q_B/Q_{in}$ , and the calculated bottom flow conductance ( $C_B$ ). The measurements correspond to both open and sealed ends SFDs. Moreover, the recorded  $Q_{in}$  and  $P_{in}$  for estimation of the orifice conductance  $C_o=1/R_o$  are also listed. Figure 9 depicts graphically the flow rate measured in both open and sealed ends SFD versus supply pressure ( $P_{in}$ ). Note that pressure at the feed hole  $P_s$  is estimated based on Eq.(1).

For an open ends damper A with  $c_A=0.254$  mm, the flow conductances of the top and bottom lands are:

$$C_{TL} = \frac{1}{R_{TL}} = 8.43 \frac{\text{LPM}}{\text{bar}} \quad \text{and} \quad C_{BL} = \frac{1}{R_{BL}} = 9.59 \frac{\text{LPM}}{\text{bar}} \quad (2)$$

Both top and bottom film lands offer similar flow conductances, albeit bottom land offers 14% larger conductance ( $C_{BL}/C_{TL}=1.14$ ). The difference is most likely due to the uncertainty in the measurement of the flow through the bottom side of the damper ( $\pm 5\%$ ) and the journal and indicating the BC may not have been perfectly aligned. Notice that the conductance of the three orifices is  $3C_o = 30.20 \text{ LPM}/\text{bar}$ .

For the top and bottom ends sealed damper A, the flow resistances (and conductances) are calculated as

$$\begin{aligned} R_{TS} &\cong \frac{1}{C_{TS}} = \frac{1}{C_T} - \frac{1}{C_{TL}} = 1.62 \frac{\text{bar}}{\text{LPM}} \rightarrow C_{TS} = \frac{1}{R_{TS}} = 0.62 \frac{\text{LPM}}{\text{bar}} \\ R_{BS} &\cong \frac{1}{C_{BS}} = \frac{1}{C_B} - \frac{1}{C_{BL}} = 2.03 \frac{\text{bar}}{\text{LPM}} \rightarrow C_{BS} = \frac{1}{R_{BS}} = 0.49 \frac{\text{LPM}}{\text{bar}} \end{aligned} \quad (3)$$

The average end seal conductance is  $C_{ave-S1} = \frac{C_{TS} + C_{BS}}{2} = 0.56 \frac{\text{LPM}}{\text{bar}}$  which is  $\sim 6.2\%$  that of the open ends SFD with an identical radial clearance.

The end seal flow conductance ( $\bar{C}_{seal-1}$ ) per unit circumference length is

$$\bar{C}_{seal-1} = \frac{0.56 \frac{\text{LPM}}{\text{bar}}}{\pi D} = 2.34 \cdot 10^{-4} \frac{\text{mm}^2}{\text{s} \cdot \text{Pa}} \quad (4)$$

Similarly, another pair of seals' flow conductance is estimated as  $C_{ave-S2}=0.89$  LPM/bar that is  $\sim 60\%$  larger flow conductance than the damper sealed with  $C_{ave-S1}$ , i.e.,  $C_{ave-S2}=1.6 \cdot C_{ave-S1}$ . See Table 2(c) for details. Note that second pair of piston rings has larger clearance for ring slit than the first pair (dimensions are not specified due to its proprietary design).

Later, a set of experiments consists of circular dynamic load excitations with two pairs of piston seals ( $C_{ave-S1}$  and  $C_{ave-S2}$ ), respectively.

Table 2. Feed pressure and lubricant flow rate for (a) three feed holes, (b): open ends and (c)-(d): sealed ends damper A ( $c_A=0.254$  mm).  $P_S$  estimated based on Eq.(1). Land length  $L=25.4$  mm, ISO VG 2 oil at room temperature  $T_S=23^\circ\text{C}$ .

(a) Three feed holes open to ambient ( $P_S=P_a$ )

$P_{in}$ (bar(g))	0.07	0.14	0.21	0.28
$Q_{in}$ (LPM)	3.67	5.02	6.15	7.48
Flow conductance	$3C_o$	<b>30.20</b>	<b>LPM/bar</b>	

(b) Open ends SFD ( $c_A=0.254$  mm)

$P_{in}$ (barg)	$P_S$ (barg)	$Q_{in}$ (LPM)	$Q_B$ (LPM)	Ratio $Q_B/Q_{in}$
0.28	0.12	4.59	2.30	0.50
0.41	0.22	5.84	2.92	0.50
0.69	0.44	7.54	3.95	0.52
0.83	0.55	8.45	4.77	0.56
0.97	0.65	9.40	5.12	0.54
<b>0.63</b>	<b>0.40</b>	<b>7.16</b>	<b>3.81</b>	<b>0.53</b>
Flow Conductance	Total $C_{total-open}$	Top Land $C_{TL-open}$	Bottom Land $C_{BL-open}$	
<b>LPM/bar</b>	<b>18.02</b>	<b>8.43</b>	<b>9.59</b>	

(c) Sealed ends SFD ( $c_A=0.254$  mm):  $C_{ave-s1}=0.56$  (LPM/bar)

$P_{in}$ (barg)	$P_S$ (barg)	$Q_{in}$ (LPM)	$Q_B$ (LPM)	Ratio $Q_B/Q_{in}$
0.59	0.57	0.64	0.29	0.46
1.10	1.06	1.25	0.55	0.44
1.38	1.33	1.48	0.64	0.43
1.65	1.60	1.71	0.73	0.43
2.07	2.01	1.78	0.86	0.48
<b>1.36</b>	<b>1.31</b>	<b>1.37</b>	<b>0.62</b>	<b>0.45</b>
Flow Conductance	Total $C_{total-seal}$	Top Land $C_{T-seal-1}$	Bottom Land $C_{B-seal-1}$	
<b>LPM/bar</b>	<b>1.045</b>	<b>0.576</b>	<b>0.469</b>	

(d) Sealed ends SFD ( $c_A=0.254$  mm):  $C_{ave-s2}=0.89$  (LPM/bar)

$P_{in}$ (barg)	$P_S$ (barg)	$Q_{in}$ (LPM)	$Q_B$ (LPM)	Ratio $Q_B/Q_{in}$
0.57	0.54	0.99	0.45	0.45
0.80	0.76	1.25	0.55	0.44
0.92	0.88	1.36	0.61	0.44
<b>0.77</b>	<b>0.73</b>	<b>1.20</b>	<b>0.54</b>	<b>0.45</b>
Flow Conductance	Total $C_{total-seal}$	Top Land $C_{T-seal-2}$	Bottom Land $C_{B-seal-2}$	
<b>LPM/bar</b>	<b>1.654</b>	<b>0.916</b>	<b>0.738</b>	

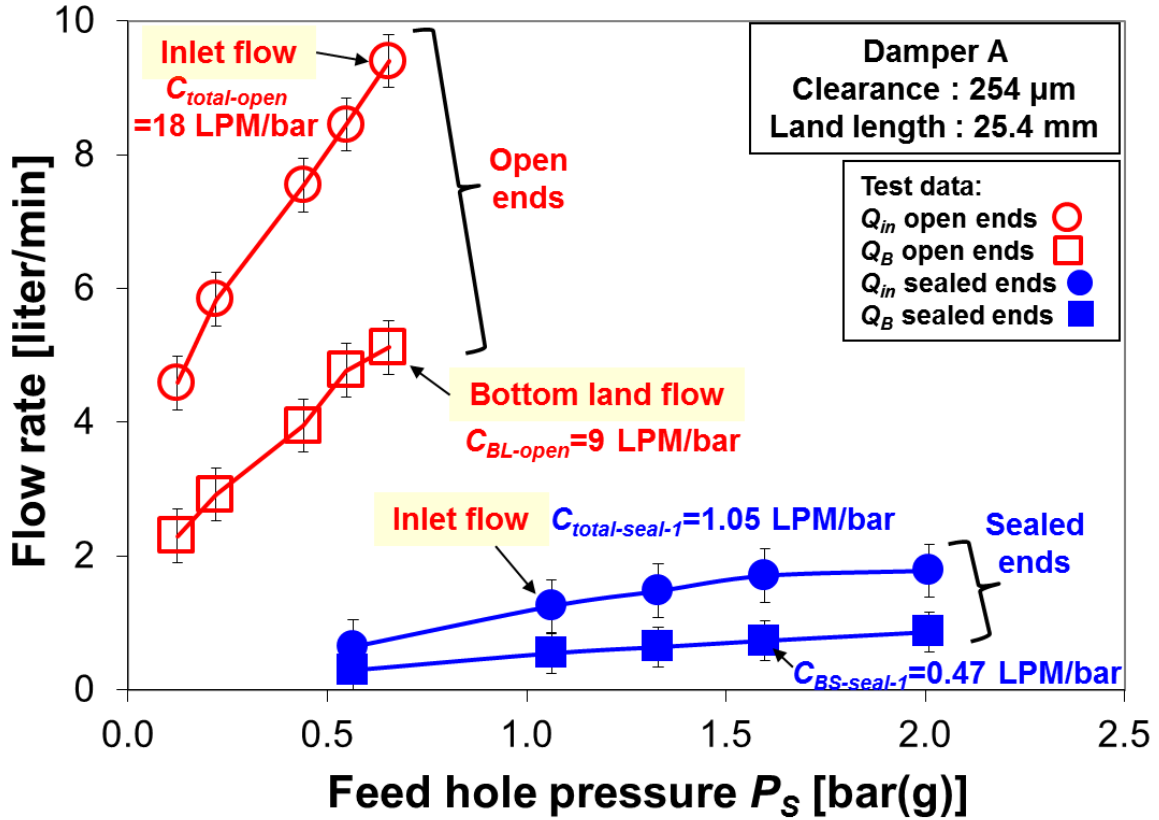


Figure 9. Oil flow rate at inlet ( $Q_{in}$ ) and through bottom section ( $Q_B$ ), versus feed hole pressure ( $P_s$ ) for open and sealed ends SFD ( $c_A=0.254$  mm).  $P_s$  estimated based on Eq.(1). Flow conductance labeled.

## Description of Single Frequency Dynamic Load<sup>1</sup>

Figure 10 provides (a) a description of the BC kinematics for a whirl orbit motion, (b) the coordinate systems of the BC and a static loader (c) a depiction of various whirl orbits at centered and off-centered conditions. Figure 10(a) depicts the whirl motion of the BC with amplitude components ( $r_x, r_y$ ) at a frequency  $\omega_{(t)}$ .  $\vec{e}_s$  and  $\vec{e}_{(t)}$  denote the eccentricity vectors from the origin to the BC static position and origin to the orbital path, respectively. As shown in Figure 10(b), the static loader pulls the BC to a static off-centered condition along  $\bar{x}$  axis,  $45^\circ$  away from  $(X, Y)$ .

<sup>1</sup> Portions of this section reproduce ad-verbatim information presented in Ref. [23]



For single-frequency dynamic loads, the ramp rate  $\alpha=0$  and the excitation frequency  $\omega$  is constant, with magnitude set at steps of 10 Hz over the frequency range 10-100 Hz.

The test rig is modeled as a two degree of freedom mechanical system and governed by the following equation of motion in the frequency domain

$$[\mathbf{K}_L - \omega^2 \mathbf{M}_L + i\omega \mathbf{C}_L] \mathbf{Z}_{(\omega)} = \mathbf{F}_{(\omega)} - M_{BC} \mathbf{a}_{(\omega)} \quad (7)$$

where  $\mathbf{F}_{(\omega)}$ ,  $\mathbf{Z}_{(\omega)}$ ,  $\mathbf{a}_{(\omega)}$  are vectors of the discrete Fourier transforms of the recorded dynamic load, bearing cartridge (BC) displacement relative to the journal, and BC acceleration, respectively. Above,  $M_{BC}=15.15$  kg is the mass of the BC.

Discrete Fourier transforms of the data obtained from two linearly independent excitation force vectors  $\mathbf{F}_{CW}$  and  $\mathbf{F}_{CCW}$  produce:

$$\mathbf{F}_{CW} \Rightarrow \begin{Bmatrix} \mathbf{Z}_{CW} \\ \mathbf{a}_{CW} \end{Bmatrix}, \mathbf{F}_{CCW} \Rightarrow \begin{Bmatrix} \mathbf{Z}_{CCW} \\ \mathbf{a}_{CCW} \end{Bmatrix} \quad (8)$$

Then Eqn. (7) can be solved for using the recorded data.

$$\mathbf{H}_L = [\mathbf{F}_{CW} - M_{BC} \mathbf{a}_{CW} \quad \mathbf{F}_{CCW} - M_{BC} \mathbf{a}_{CCW}] [\mathbf{Z}_{CW} \quad \mathbf{Z}_{CCW}]^{-1} \quad (9)$$

To identify the lubricated system force coefficients  $(\mathbf{K}, \mathbf{C}, \mathbf{M})_L$ , a complex stiffness matrix is defined as

$$\mathbf{H}_L = [\mathbf{K} - \omega^2 \mathbf{M} + i\omega \mathbf{C}]_L \quad (10)$$

Where the real part  $\text{Re}(\mathbf{H}_L) \rightarrow (\mathbf{K}_L - \omega^2 \mathbf{M}_L)$  yields the lubricated system stiffness  $(\mathbf{K}_L)$  and added mass  $(\mathbf{M}_L)$  coefficients, and the imaginary part  $\text{Im}(\mathbf{H}_L) \rightarrow (\omega \mathbf{C}_L)$  yields the lubricated system damping coefficients  $(\mathbf{C}_L)$ .

The SFD complex stiffnesses  $(\mathbf{H}_{\text{SFD}})$  follow by subtracting the dry system complex stiffnesses  $(\mathbf{H}_s)$ , calculated in the same manner, from the lubricated system complex stiffnesses. That is

$$\mathbf{H}_{\text{SFD}} = \mathbf{H}_L - \mathbf{H}_s \quad (11)$$

Appendix C details the identification of mechanical parameters  $(K, C, M)_s$  for the test dry system. In brief, the estimated structural force coefficients for the dry system (without lubricant in the film land) are  $K_s=12.0$  MN/m,  $M_s=3.5$  kg, and  $C_s=0.6$  kN.s/m. Note that the BC mass  $M_{BC}=15.15$  kg. The estimated damping ratio ( $\zeta$ ) for the dry (no oil) test system is ~2% or less, typical of a steel structure. The dry system natural frequency is

$$f_n = \sqrt{\frac{K_s}{M_{BC}}} = 127 \text{ Hz.}$$

Table 3 outlines the operating conditions for whirl orbit motions resulting from a single frequency dynamic load. For single-frequency dynamic loads ( $\alpha=0$ ), the excitation frequency  $\omega$  is fixed, at intervals of 10 Hz, over the frequency range 10-100 Hz. Note that a sealed ends damper produces much larger reaction forces which reach the load capacity of the shakers; thus the tests are limited to an excitation frequency ( $\omega$ ) less than 100 Hz.

The static loader, positioned  $45^\circ$  away from the  $X$  and  $Y$  directions, pulls the bearing cartridge to a desired static eccentricity  $e_s$  ( $\bar{X}$  -direction). The shakers exert single frequency forces to produce circular whirl motions of the BC with amplitude  $r$ . For sealed ends SFD, Dynamic load tests are conducted at three static eccentricities ( $e_s=0.0c_A$ ,  $0.25c_A$  and  $0.50c_A$ ) and with orbit radius  $r/c_A = 0.15, 0.30, 0.45, \text{ and } 0.60$ . Note that larger orbit radii could not be produced at a high static eccentricity ( $e_s/c_A > 0.5$ ) for the open ends SFD. Ref.[5] details experimental results with single frequency dynamic loads for open ends damper A ( $c_A=254 \mu\text{m}$ ).

During the tests for sealed damper (with flow conductance  $C_{ave-S1}$ ) the lubricant supply pressure upstream of the feedholes is maintained at  $P_{in-1} \sim 0.69 \text{ bar(g)}$  and the lubricant flow rate is  $Q_{in-1} = 0.68 \text{ LPM}$ . Afterwards, an identical tests is conducted but with  $\sim 4$  times higher oil supply pressure,  $P_{in-2} \sim 2.76 \text{ bar(g)}$ , and the corresponding lubricant flow rate  $Q_{in-2} = 2.71 \text{ LPM}$ .

After all the tests are completed for their first sealed ends damper. A second pair of piston rings replaces the first ones. Here  $C_{ave-S2} = 0.89 \text{ LPM/bar}$  that allows more leakage. Note again that second pair of piston rings has larger clearance of ring slit than the first pair (dimension proprietary). Then, circular whirl orbit tests are performed. Note that the lubricant supply pressure is set to  $P_{in-1} = 0.69 \text{ barg}$ .

**Table 3. Test conditions for open ends and sealed ends dampers for whirl circular orbit motions with a single frequency dynamic load ( $\alpha=0$ ).**

Single frequency dynamic load					
End condition	Whirl amplitude, $r/c_A$	Static eccentricity, $e_s/c_A$	Inlet flow rate, $Q_{in}$ (LPM)	Static inlet Pressure, $P_{in}$ (bar(g))	Seal conductance, $C_{ave-S}$ (LPM/bar)
Open [5]	$r/c_A = 0.15, 0.3, 0.45, 0.6, 0.75$	$e_s/c_A = 0.0$	5.03	$P_{in-3}=0.35$	-
Sealed	$r/c_A = 0.15, 0.3, 0.45, 0.6$	$e_s/c_A = 0.0$	2.71	$P_{in-1}=2.76$	0.56
	$r/c_A = 0.15, 0.3, 0.45$	$e_s/c_A = 0.25$			
	$r/c_A = 0.15, 0.3$	$e_s/c_A = 0.5$			
	$r/c_A = 0.15, 0.3, 0.45, 0.6$	$e_s/c_A = 0.0$	0.68	$P_{in-2}=0.69$	
	$r/c_A = 0.15, 0.3, 0.45$	$e_s/c_A = 0.25$			
	$r/c_A = 0.15, 0.3$	$e_s/c_A = 0.5$			
	$r/c_A = 0.15, 0.3, 0.45, 0.6, 0.75$	$e_s/c_A = 0.0$	1.07		0.89

\*Frequency range: 10 - 100 Hz. Damper clearance  $c_A=0.254$  mm.

## Single Frequency Dynamic Load Experimental Results

This section presents experimental results obtained from circular whirl motion of the sealed ends SFD induced by single frequency dynamic loads. Ref.[5] reports in full the operation condition and the experimental results for open ends damper. In summary, for open ends SFD [5], the SFD direct damping coefficients increase both with increasing orbit amplitude ( $r$ ) and static eccentricity ( $e_s$ ) while the direct added mass increase dramatically with static eccentricity ( $e_s$ ) while being less sensitive to the orbit radius  $r$  (see later in Figs. 17 and 18).

For sealed ends damper A, Figure 11 depicts the real and imaginary parts of the lubricated system direct impedances,  $H_{XX}$  and  $H_{YY}$ , as well as the corresponding physical model for circular orbit tests with orbit radius  $r/c_A=0.3$  and  $0.6$  at the centered condition  $e_s=0$ , and with radius  $r/c_A=0.3$  at the off-centered condition  $e_s/c_A=0.5$ .

Note that the test data spans frequency range 10-100 Hz. It is important to state that the identification of parameters considers only the data obtained within the frequency range  $f_{start}=10$  Hz to  $f_{end}=100$  Hz. For the most part, the physical model curve fits show satisfactory correlation factor ( $R^2 > 0.95$ ) indicating the physical model is adequate for the selected frequency range ( $f_{start}, f_{end}$ ).

The imaginary part of the system direct impedances shows a constant slope indicating the damping is viscous in character. In addition, the slope increase with an increase in orbit size ( $r$ ) and in journal static eccentricity ( $e_s$ ), thus evidencing that  $C_{XX}$  and  $C_{YY}$  are a function of both  $r$  and  $e_s$ .

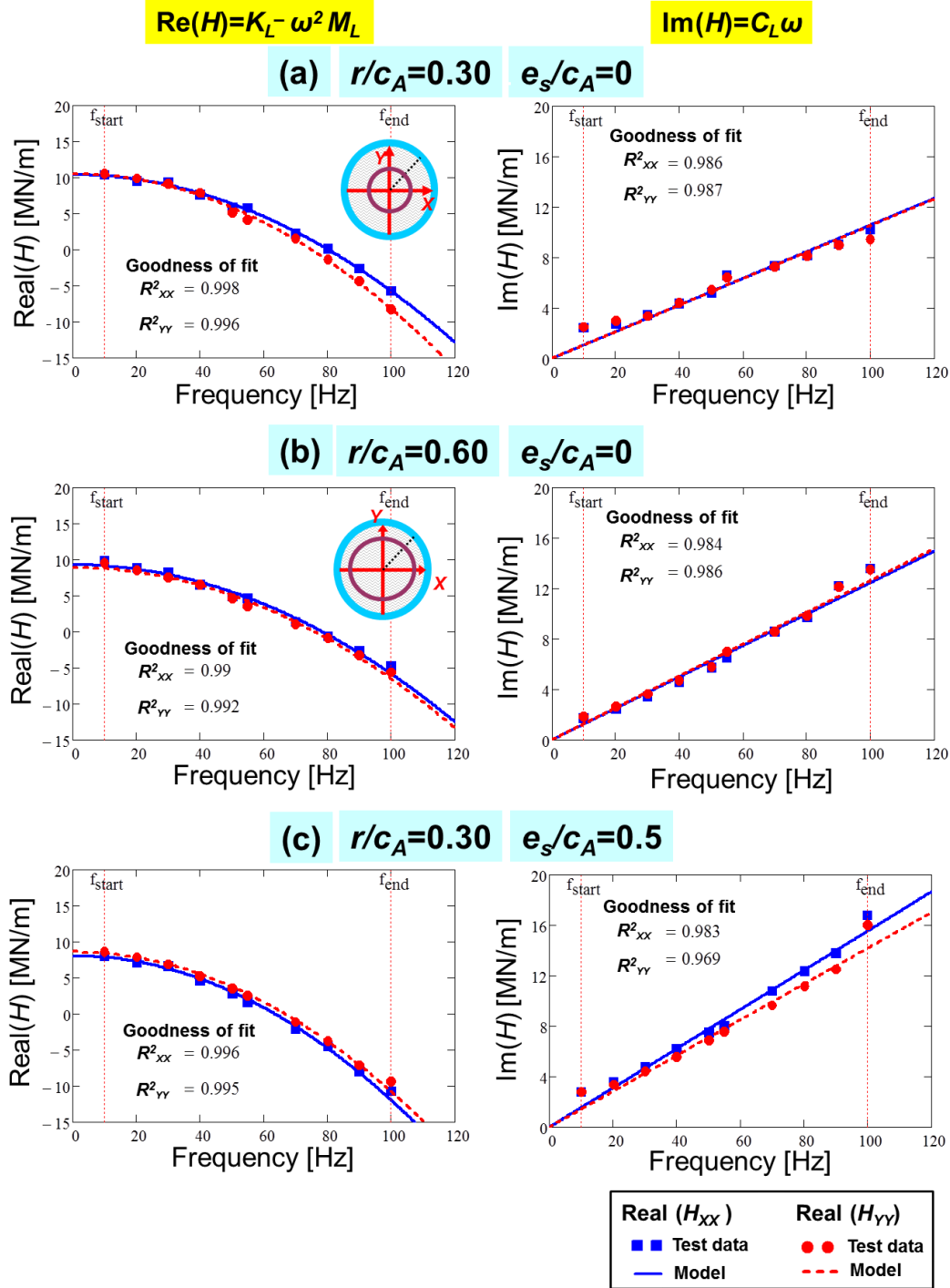


Figure 11. Real and imaginary parts of direct complex stiffness ( $H_{xx}$ ,  $H_{yy}$ ) versus excitation frequency. Test data and corresponding physical model. Sealed ends SFD ( $c_A=0.254$  mm) with circular orbits of amplitude (a)  $r/c_A=0.3$  and  $e_s/c_A=0$ , (b)  $r/c_A=0.6$  and  $e_s/c_A=0$ , (c)  $r/c_A=0.3$  and  $e_s/c_A=0.5$ . Lubricant supply pressure  $P_{in-2}=2.76$  bar with seal conductance  $C_{ave-S1}=0.56$  LPM/bar.

Figures 12 and 13 show surface plots of SFD direct and cross-coupled damping ( $C$ ), inertia ( $M$ ) and stiffness ( $-K$ ) coefficients for operating conditions with two lubricant supply pressures  $P_{in-1}=0.69$  bar and  $P_{in-2}=2.76$  bar, respectively. The test data correspond to centered circular orbit tests of increasing orbit amplitude ( $r/c_A$ ) and at three static eccentricities ( $e_s = 0.0c_A, 0.25c_A$  and  $0.50c_A$ ).

For a sealed ends SFD with oil supply pressure  $P_{in-1}=0.69$  bar in Figure 12, the SFD direct damping coefficients ( $C_{A-XX}, C_{A-YY}$ ) increase both with increasing orbit radius ( $r/c_A$ ) and static eccentricity ( $e_s$ ). In general, the direct and cross-coupled SFD damping coefficients for the  $X$  and  $Y$  axes are virtually identical ( $C_{A-XX} \sim C_{A-YY}, C_{A-XY} \sim C_{A-YX}$ ) evidencing a high degree of isotropy; hence only the  $X$ -axis coefficients are shown for brevity. Cross-coupled damping  $C_{A-XY}$  increases with static eccentricity and reaches  $\sim 23\%$  of the direct coefficient one ( $C_{A-XX}$ ) at  $e_s/c_A=0.5$ ; however,  $C_{A-XY}$  is insensitive to the orbit amplitude ( $r$ ).

The SFD direct inertia coefficients ( $M_{A-XX} \sim M_{A-YY}$ ) increase with static eccentricity ( $e_s$ ) while decreasing quickly with orbit amplitude ( $r/c_A$ ). The cross-coupled coefficient  $M_{A-XY}$  does not show a distinguishable trend with the orbit amplitude ( $r/c_A$ ), but increases with static eccentricity. For whirl motions departing from  $e_s/c_A=0.5$  with amplitude  $r/c_A=0.15$ , the direct inertia  $M_{A-XX}$  is  $\sim 22\%$  larger than the  $M_{A-XX}$  for whirl motions departing from  $e_s/c_A=0$  with the same orbit amplitude.

The SFD stiffness coefficients are all negative (softening) and are a fractional amount of the support stiffness ( $K_{A-XX} \sim 0.21 K_s$ ) at  $e_s/c=0.5$ . Note that  $|K_{A-XX}|$  grows linearly with both the static eccentricity ( $e_s$ ) and orbit amplitude ( $r$ ) while the cross-coupled stiffness coefficients are infinitesimal at all conditions.

For a higher lubricant supply pressure  $P_{in-2}=2.76$  bar in Figure 13, the SFD direct damping ( $C_{A-XX}$ ) is more or less constant with increasing orbit radius ( $r$ ) yet increases with static eccentricity ( $e_s$ ). Cross-coupled terms ( $C_{A-XY}$ ) are small compared to the direct ones, albeit increases with  $e_s$  and reaches  $\sim 20\%$  of  $C_{A-XX}$  at  $e_s/c=0.5$ .

The SFD direct and cross-coupled inertia coefficients ( $M_{A-XX}, M_{A-XY}$ ) show a similar trend. That is, the direct added mass increases with  $e_s$ , but shows a constant magnitude with across all  $r$ . Cross-coupled inertia increases with static eccentricity and  $M_{A-XY}$  is

$\sim 0.11 M_{A-XX}$  at  $e_s/c=0.5$ . The SFD stiffness coefficient ( $K_{A-XX}$ ) increases both with  $e_s$  and  $r$  while  $K_{A-XY}$  is minute over the test range.

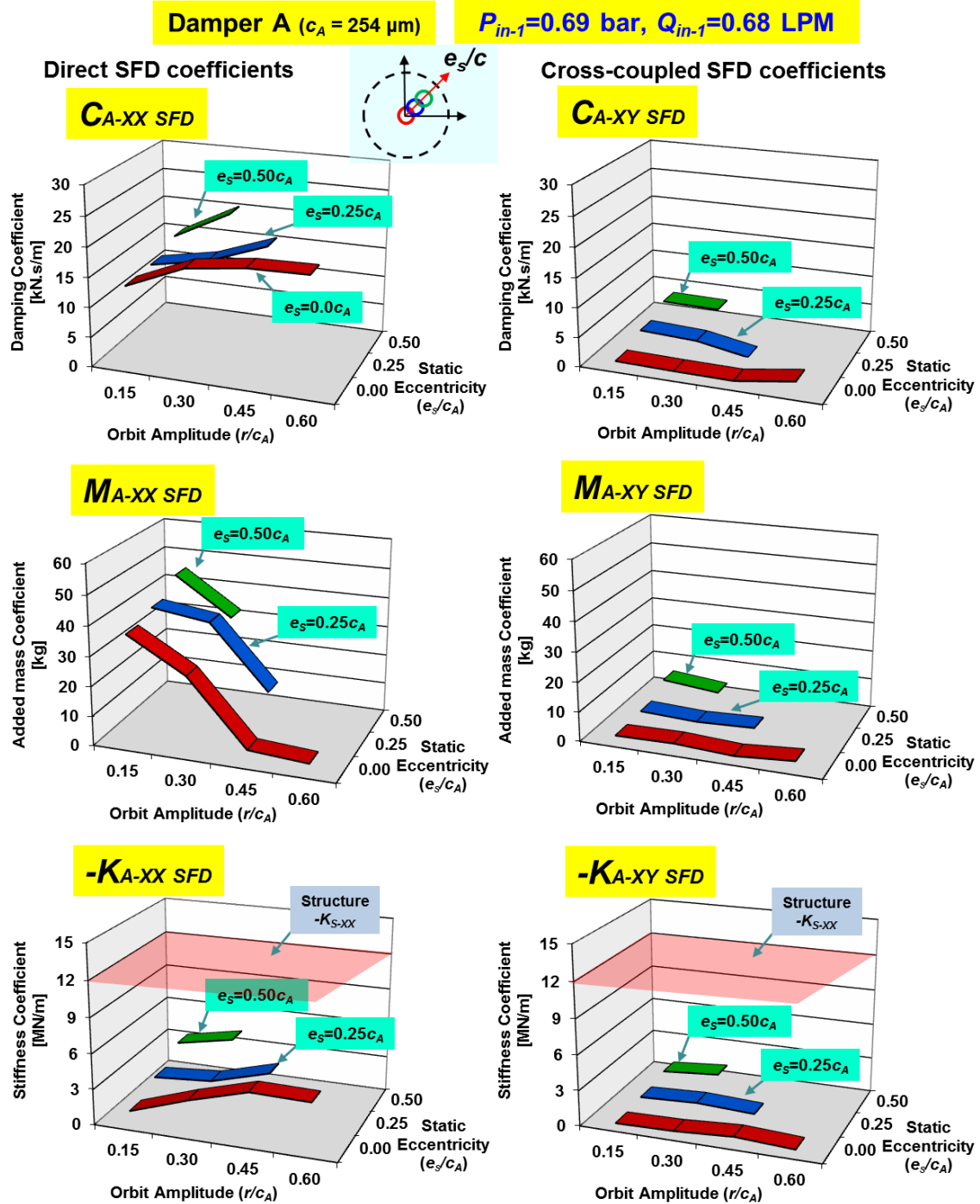


Figure 12. **Sealed ends damper A ( $c_A=254\mu\text{m}$ )** with lubricant supply pressure  $P_{in-1}=0.69 \text{ bar}$  ( $1/4 \cdot P_{in-2}$ ). SFD direct and cross-coupled dynamic force coefficients versus orbit amplitude ( $r/c_A$ ) at three static eccentricities ( $e_s/c_A=0.0, 0.25, 0.50$ ). Seal conductance  $C_{ave-S1} = 0.56 \text{ LPM/bar}$ . Identification frequency range 10–100 Hz.

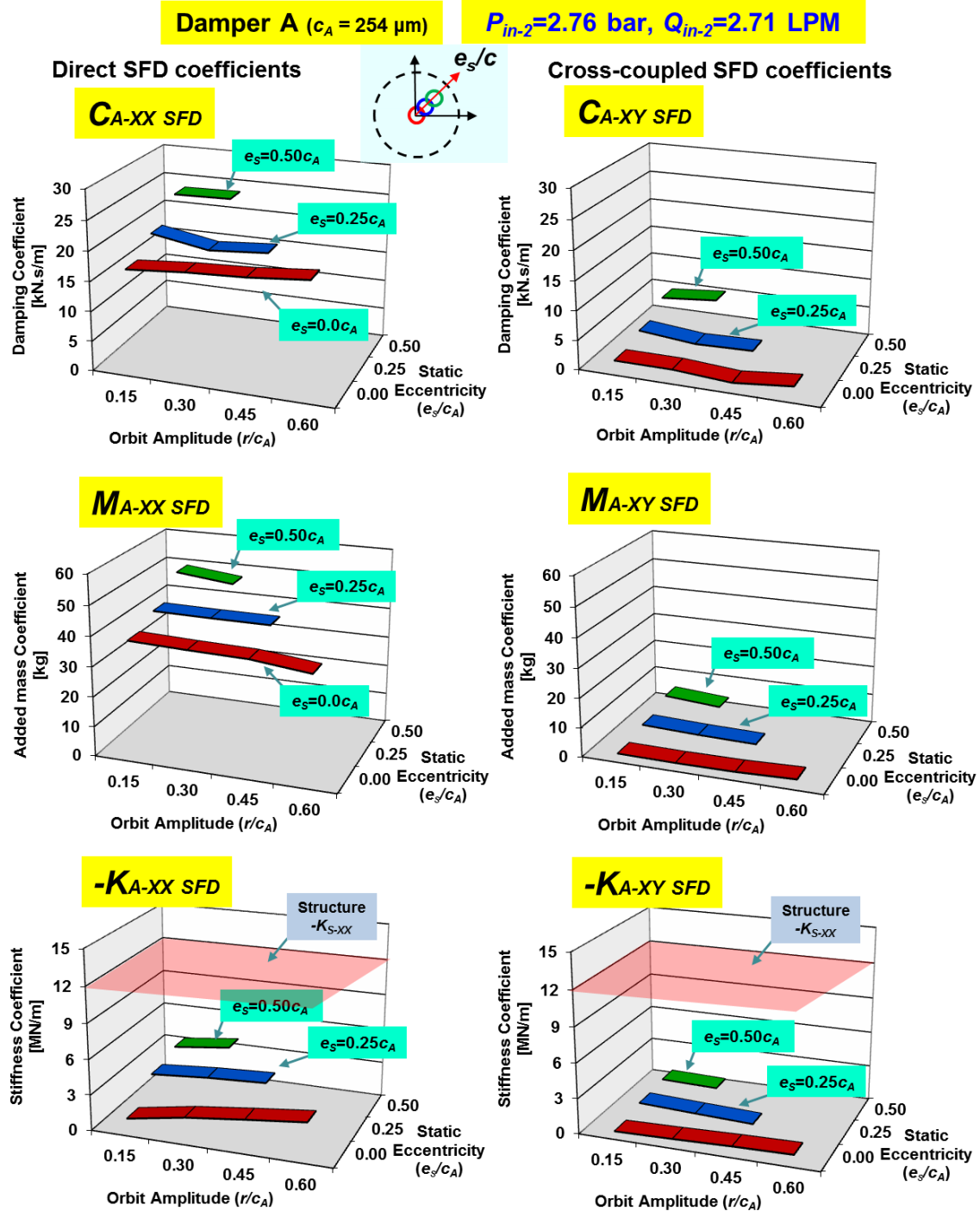


Figure 13. **Sealed ends damper A ( $c_A = 254 \mu\text{m}$ )** with lubricant supply pressure  $P_{in-2} = 2.76 \text{ bar}$  ( $4 \cdot P_{in-1}$ ). SFD direct and cross-coupled dynamic force coefficients versus orbit amplitude ( $r/c_A$ ) at three static eccentricities ( $e_s/c_A = 0.0, 0.25, 0.50$ ). Seal conductance  $C_{ave-S1} = 0.56 \text{ LPM/bar}$ . Identification frequency range 10–100 Hz.

## Effect of Lubricant Supply Pressure on Sealed Ends SFD Force Coefficients

Figure 14 depicts the experimental SFD direct damping  $(C_{XX}, C_{YY})_{\text{SFD}}$  and added mass  $(M_{XX}, M_{YY})_{\text{SFD}}$  coefficients for the sealed ends SFD supplied with lubricant at  $P_{in-1} \sim 0.69$  barg ( $Q_{in-1} = 0.68$  LPM) and  $P_{in-2} \sim 2.76$  barg ( $Q_{in-2} = 2.68$  LPM). The test data correspond to centered circular orbit tests ( $e_s/c_A = 0.0$ ) with orbit radii  $r = 0.15c_A - 0.60c_A$ . Note that the end seals flow conductance is  $C_{ave-S1} = 0.56$  LPM/bar.

At small whirl amplitude motion  $r = 0.15c_A$ , the experimental direct damping  $(C_{XX}, C_{YY})_{\text{SFD}}$  with large oil supply pressure  $P_{in-2} \sim 2.76$  barg provide  $\sim 26\%$  larger magnitude than the those with smaller  $P_{in-1} \sim 0.69$  barg. With increasing amplitude motion ( $r$ ),  $C_{XX(P_{in-1})}$  and  $C_{XX(P_{in-2})}$  show an opposite trend where  $C_{XX(P_{in-1})}$  increases rapidly and then tend to plateau while  $C_{XX(P_{in-2})}$  shows a constant value. For a reduced oil supply pressure  $P_{in-1} \sim 0.69$  barg, the inertia coefficients  $(M_{XX}, M_{YY})$  decrease quickly with orbit amplitude whereas the damper with a higher  $P_{in-2}$  has more uniform coefficients.

Figure 15 shows the identified direct damping  $(C)_{\text{SFD}}$  and inertia  $(M)_{\text{SFD}}$  coefficients for the SFD supplied with lubricant at varying pressures. The coefficients are identified from whirl orbits with amplitude  $r/c_A = 0.15$  and for increasing static eccentricity  $e_s/c_A = 0.0 - 0.5$ . The damping coefficients increase both with increasing oil supply pressure and static eccentricity ( $e_s$ ). The sealed ends damper operating with higher supply pressure ( $P_{in-2}$ ) provides  $\sim 26\% - 50\%$  larger damping than those with lower supply pressure ( $P_{in-1}$ ), the difference in magnitude becoming larger with an increasing static eccentricity ( $e_s$ ). The inertia force coefficients for both conditions  $P_{in-1}$  and  $P_{in-2}$ , overlap onto each other; albeit  $M_{YY(P_{in-2})}$  is  $\sim 10\%$  larger than  $M_{YY(P_{in-1})}$  at  $e_s/c_A = 0.5$ .

Appendix D presents the detailed procedure for the calculation of uncertainty in the SFD force coefficients. In general, the direct damping, added mass, and stiffness coefficients have a total uncertainty of  $U_C < 9.2\%$ ,  $U_M < 17.4\%$  and  $U_K < 2.3\%$ , respectively. The uncertainties are valid for the identification frequency range 10-100 Hz only.

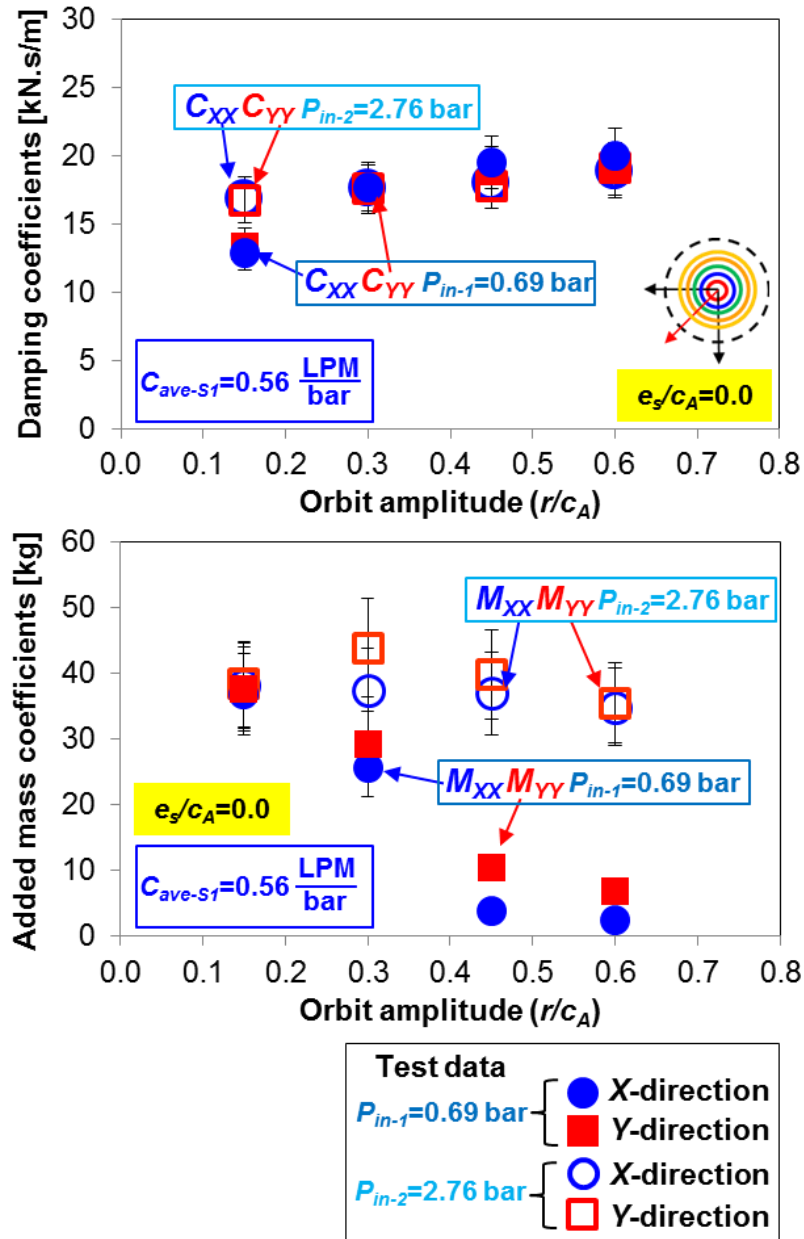


Figure 14. **Effect of lubricant supply pressure:** sealed ends SFD direct damping ( $C_{SFD}$ ) and added mass ( $M_{SFD}$ ) force coefficients versus whirl orbit amplitude ( $r/c_A$ ) at journal centered condition ( $e_g/c_A=0.0$ ). Lubricant supply pressure  $P_{in-1}=0.69$  bar and  $P_{in-2}=2.76$  bar. Seal conductance  $C_{ave-S1}=0.56$  LPM/bar. Identification frequency range 10–100 Hz.

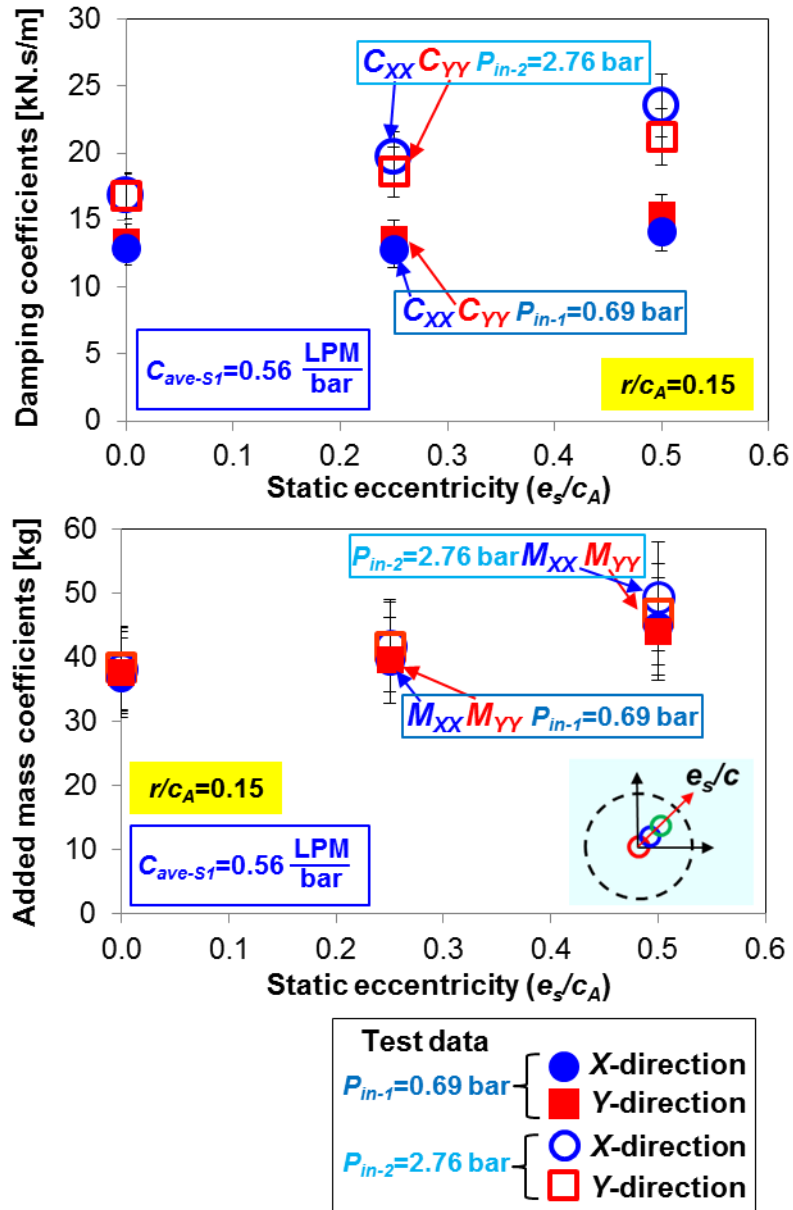


Figure 15. **Effect of lubricant supply pressure:** sealed ends SFD direct damping ( $C$ )<sub>SFD</sub> and added mass ( $M$ )<sub>SFD</sub> force coefficients versus static eccentricity ( $e_s/c_A$ ) at whirl orbit amplitude ( $r/c_A=0.15$ ). Lubricant supply pressure  $P_{in-1}=0.69 \text{ bar}$  and  $P_{in-2}=2.76 \text{ bar}$ . Seal conductance  $C_{ave-S1} = 0.56 \text{ LPM/bar}$ . Identification frequency range 10–100 Hz.

## Effect of Flow Conductance on Sealed Ends SFD Force Coefficients

Figure 16 depicts the experimental direct damping  $(C_{XX}, C_{YY})_{\text{SFD}}$  and inertia  $(M_{XX}, M_{YY})_{\text{SFD}}$  operating with both the lubricant inlet pressure  $P_{in-1} \sim 0.69$  barg. There are two ends seals configuration, one with seal conductance  $C_{ave-S1} = 0.56$  LPM/bar and  $C_{ave-S2} = 0.89$  LPM/bar, respectively. Recall that the two separate pairs of seal provide two distinct seal conductances  $C_{ave-S1}$  and  $C_{ave-S2}$  (Table 2). The second damper leaks 60% more than the damper with  $C_{ave-S1}$ , i.e.,  $\frac{C_{ave-S2}}{C_{ave-S1}} = 1.6$ . The test data correspond to motion with whirl orbit amplitude  $r = 0.15c_A$  to  $0.60c_A$  and at a journal centered condition ( $e_S/c_A = 0.0$ ).

The direct damping coefficients  $(C)_{\text{SFD}}$  for both flow conductances ( $C_{ave-S1}$  and  $C_{ave-S2}$ ) increase mildly with orbit amplitude motion ( $r$ ). However, in general, the damping coefficients with the lower flow conductance  $C_{ave-S1}$  increase more with increasing whirl amplitude ( $r/c_A$ ) and eventually show  $\sim 20\%$  larger damping for motion with orbit amplitude  $r/c_A = 0.6$ . Note that for small whirl amplitude motions  $r/c_A = 0.15$ , both damping coefficients ( $C_{XX-C_{ave-S1}}$  and  $C_{XX-C_{ave-S2}}$ ) are within the uncertainty range. For the damper with  $C_{ave-S}$  less than 1 LPM/bar ( $\bar{C}_{seal} = 4.0 \cdot 10^{-4} \frac{\text{mm}^2}{\text{s} \cdot \text{Pa}}$ ), both damping and inertia coefficients do not increase significantly (later see predictions in Figure 29).

For a damper with either flow conductance, the SFD inertia coefficients decrease with increasing whirl amplitude motion ( $r$ ). For small amplitude of motion ( $r/c_A \leq 0.3$ ), added mass  $(M)_{\text{SFD}}$  for the damper with higher flow resistance  $C_{ave-S1}$  shows  $\sim 12\% - 30\%$  larger magnitude than that of the damper with smaller flow resistance  $C_{ave-S2}$ . Interestingly, as the orbit amplitude increases to  $r/c_A > 0.3$ , the difference in magnitude of added mass (obtained from either flow conductance) becomes smaller.

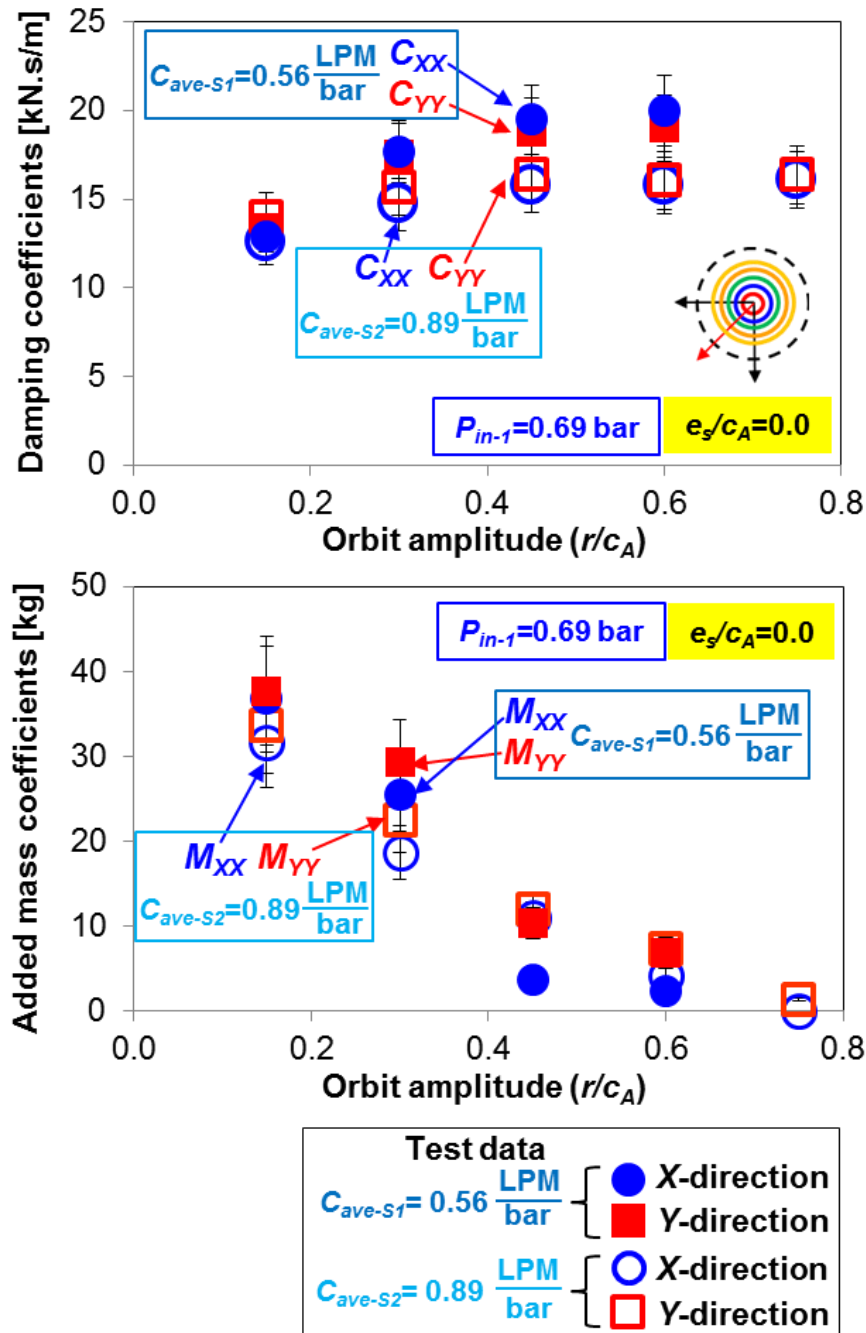


Figure 16. **Effect of flow conductance**: sealed ends SFD direct damping ( $C_{SFD}$ ) and added mass ( $M_{SFD}$ ) force coefficients versus whirl orbit amplitude ( $r/c_A$ ) at journal centered condition ( $e_s/c_A=0.0$ ). Lubricant supply pressure  $P_{in-1}=0.69$  bar. Seal conductances  $C_{ave-S1}=0.56$  LPM/bar and  $C_{ave-S2}=0.89$  LPM/bar. Identification frequency range 10–100 Hz.

## Comparison of Experimental Force Coefficients from Both Open Ends and Sealed Ends Dampers

Table 4 (reproduced from Table 3 for convenience) lists the geometry and the operating conditions for both open ends and sealed ends SFDs. The damper configurations have an identical radial clearance  $c_A=0.254$  mm and axial film length  $L=25.4$  mm. Without the piston seals in place, the open ends damper has total wetted length  $L_{tot}=36.83$ mm and an effective film length  $L_{eff}=2.97$ mm [5]. The oil feed pressure is set at  $P_{in-3}\sim 0.35$  barg (5 psig) and  $P_{in-1}\sim 0.69$  barg (10 psig) for operation with open ends and sealed ends, respectively. The corresponding flow rates ( $Q_{in}$ ) are 5.03 LPM and 0.68 LPM. Note the significant drop in flow rate ( $Q_{in}$ ) when the film land ends are sealed with the piston rings. The lubricant inlet flow rate ( $Q_{in}$ ) and pressure ( $P_{in}$ ) are chosen to be comparable with those used to obtain prior test results in Refs.[3,5,15,29,30].

**Table 4. Open ends and sealed ends SFD configurations and operating conditions**

Parameter	Open ends [5]	Sealed ends
Radial clearance	254 $\mu$ m	
Land length	$L_{eff}=2.97^*$	$L=2.54$
Static inlet pressure, $P_{in}$	$P_{in-3}=0.35$ bar(g)	$P_{in-1}=0.69$ bar(g)
Inlet flow rate, $Q_{in}$	5.03 LPM	0.68 LPM

\*Denotes the effective film land length ( $L_{eff}$ )

Figures 17 and 18 show the SFD force coefficients ( $C_{SFD}$ ,  $M_{SFD}$ ) obtained for both the sealed ends and the open ends condition versus orbit amplitude ( $r/c_A$ ) and static eccentricity ( $e_s$ ). Note the data for open ends is taken from Ref. [5]. Refer to authors' work in [5] for more detailed experimental results with open ends damper A. The inset in Figures 17 and 18 depicts the cross-section views of the two dampers.

Both the sealed ends and open ends damper show an increase of damping with increasing amplitude  $r$  and as well as increasing eccentricity  $e_s$ . The sealed ends SFD shows, not surprisingly, eleven to thirteen times more damping than the open ends configuration. This is because the end seals amplify the available damping while reducing the flowrate. Detailed comparison of recorded dynamic film pressure for the sealed ends and the open ends dampers follows.

The sealed ends damper also provides nearly eleven times more mass (inertia) coefficients. The significant increase in the mass coefficient is an important consideration as it will affect the placement of rotor-bearing system critical speeds. Nonetheless, for motions around a journal centered conditions ( $e_s=0$ ), the sealed ends SFD added mass coefficients decrease with increased orbit amplitude ( $r$ ) and eventually reach those magnitude of open ends damper  $M_{SFD} \sim 3\text{kg}$ . Note all force coefficients shown in the figure are identified with a frequency range  $\omega=10\text{-}100$  Hz.

The results, as expected, show that both damping coefficients and fluid inertia are larger for sealed ends dampers than those for open ends dampers due to the large generation of hydrodynamic pressure in the film land by restricting the squeezed lubricant flow using piston ring seals.

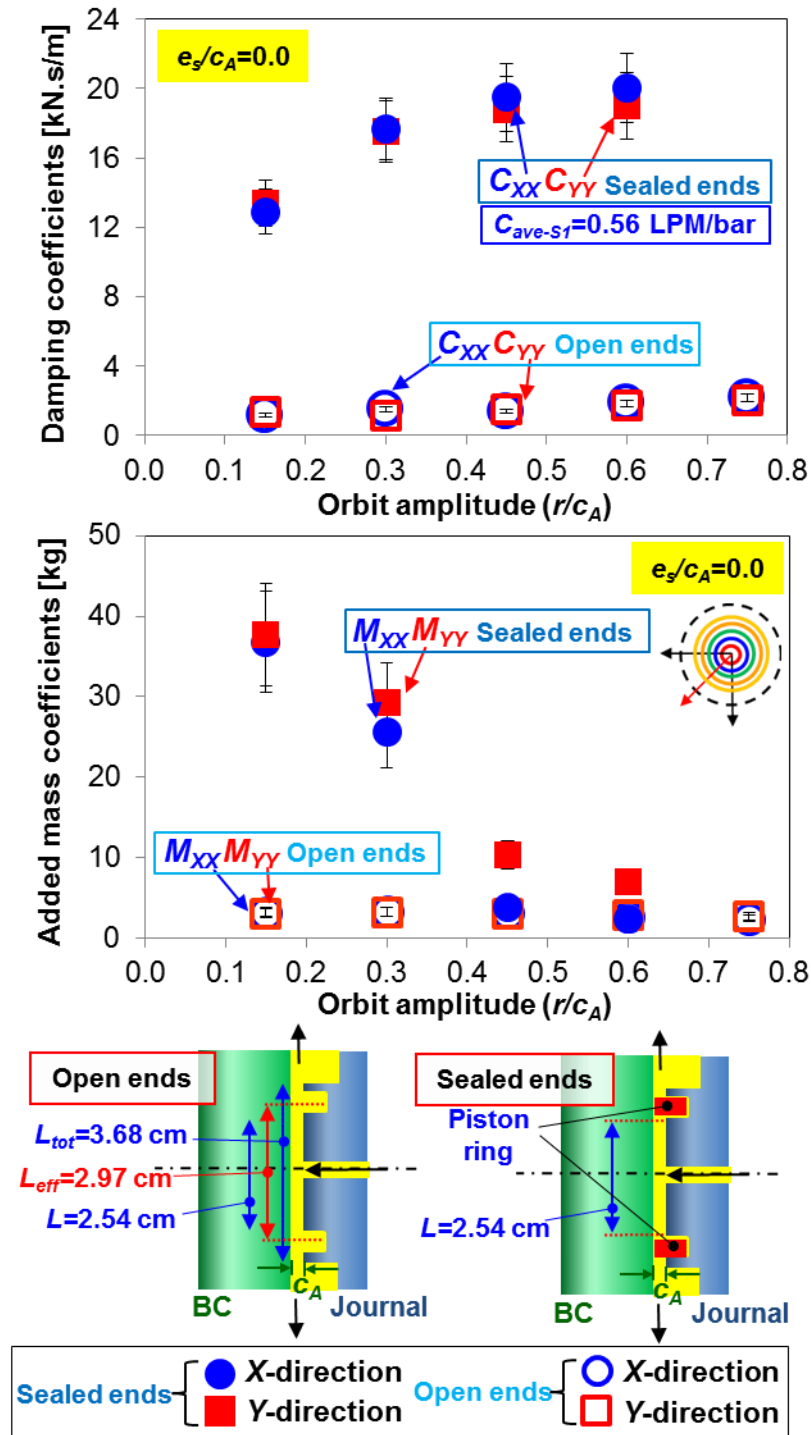


Figure 17. **Sealed ends SFD vs Open ends SFD** [5]: direct damping ( $C_{SFD}$ ) and added mass ( $M_{SFD}$ ) force coefficients versus whirl orbit amplitude ( $r/c_A$ ) at journal centered condition ( $e_s/c_A = 0.0$ ). Seal conductance  $C_{ave-S1} = 0.56$  LPM/bar. Identification frequency range 10–100 Hz.

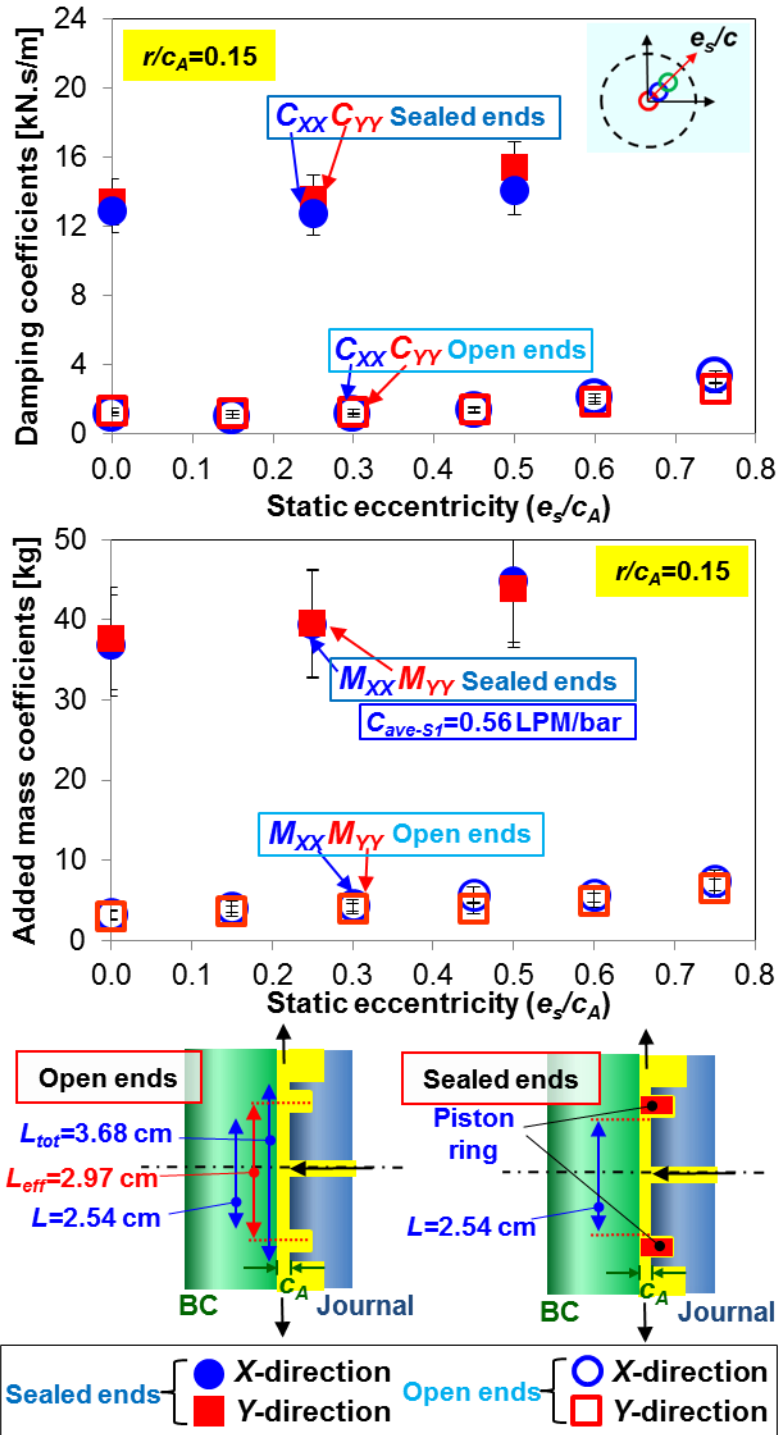


Figure 18. **Sealed ends SFD vs Open ends SFD** [5]: direct damping ( $C$ )<sub>SFD</sub> and added mass ( $M$ )<sub>SFD</sub> force coefficients versus static eccentricity ( $e_s/c_A$ ) at whirl orbit amplitude ( $r/c_A=0.15$ ). Seal conductance  $C_{ave-S1} = 0.56$  LPM/bar. Identification frequency range 10–100 Hz.

## Comparison of Recorded Film Pressures for Sealed Ends and Open Ends SFDs<sup>2</sup>

Figure 19 shows the position of pressure sensors in the bearing cartridge (BC). Eight PCB® piezoelectric dynamic pressure sensors ( $P_1 - P_8$ ) and two strain gauge EPX® absolute pressure sensors ( $E_1$  and  $E_2$ ) are installed in the BC around its circumference. Two sets of three PCB pressure sensors ( $P_{1-3} - P_{4-6}$ ), spaced apart by  $90^\circ$ , record the dynamic pressure at the top, bottom and mid sections of the damper land as shown in the figure. Note that  $P_{1-2-3}$  and  $P_{4-5-6}$  are spaced  $15^\circ$  apart. Two other piezoelectric pressure sensors ( $P_7$  and  $P_8$ ) measure the film dynamic pressures in the end grooves at the exit of the squeeze film land.

This section presents an analysis of the film dynamic pressures as a function of the amplitude ( $r$ ) and whirl frequency ( $\omega$ ) of the test damper. Ref. [5] give further details on the film dynamic pressure measurement as a function of amplitude ( $r$ ) and whirl frequency ( $\omega$ ). The following figures depict the *peak-to-peak* ( $p-p$ ) dynamic film pressures for the sealed ends damper and the open ends damper configurations.

Figure 20 shows the  $p-p$  pressures recorded at the top ( $z=1/2 L$ ), bottom ( $z=-1/2 L$ ), and mid plane ( $z=0$ ) versus whirl frequency ( $\omega$ ). The data corresponds to circular centered orbits with an amplitude of  $r/c_A=0.15$  ( $e_s=0$ ). For the ends sealed damper, the dynamic pressures are recorded to a maximum excitation frequency ( $\omega$ )=100 Hz. This frequency is lower than the maximum frequency of 250 Hz for the open ends dampers. Since the sealed ends SFD produces much larger reaction forces which reach the load capacity of the excitation shakers, tests could only be conducted for  $\omega < 100$  Hz. Figure 20(c) shows the ratio of peak-peak dynamic pressures ( $\frac{P_{sealed\ ends}}{P_{open\ ends}}$ ). Note the difference in

horizontal axis scales in Fig. 20 (a,b) and (c).

Recall that, for the open and sealed ends damper A, the lubricant supply pressure upstream of the feed holes was maintained at  $P_{in-3} \sim 0.35$  barg and  $P_{in-1} \sim 0.69$  barg, respectively. The supplied oil flow rate, measured by a turbine flow meter, ( $Q_{in}$ ) equals 5.03 LPM for the open ends damper and 0.68 LPM for the sealed ends damper.

---

<sup>2</sup> Portions of this section reproduce ad-verbatim information presented in Ref. [5].

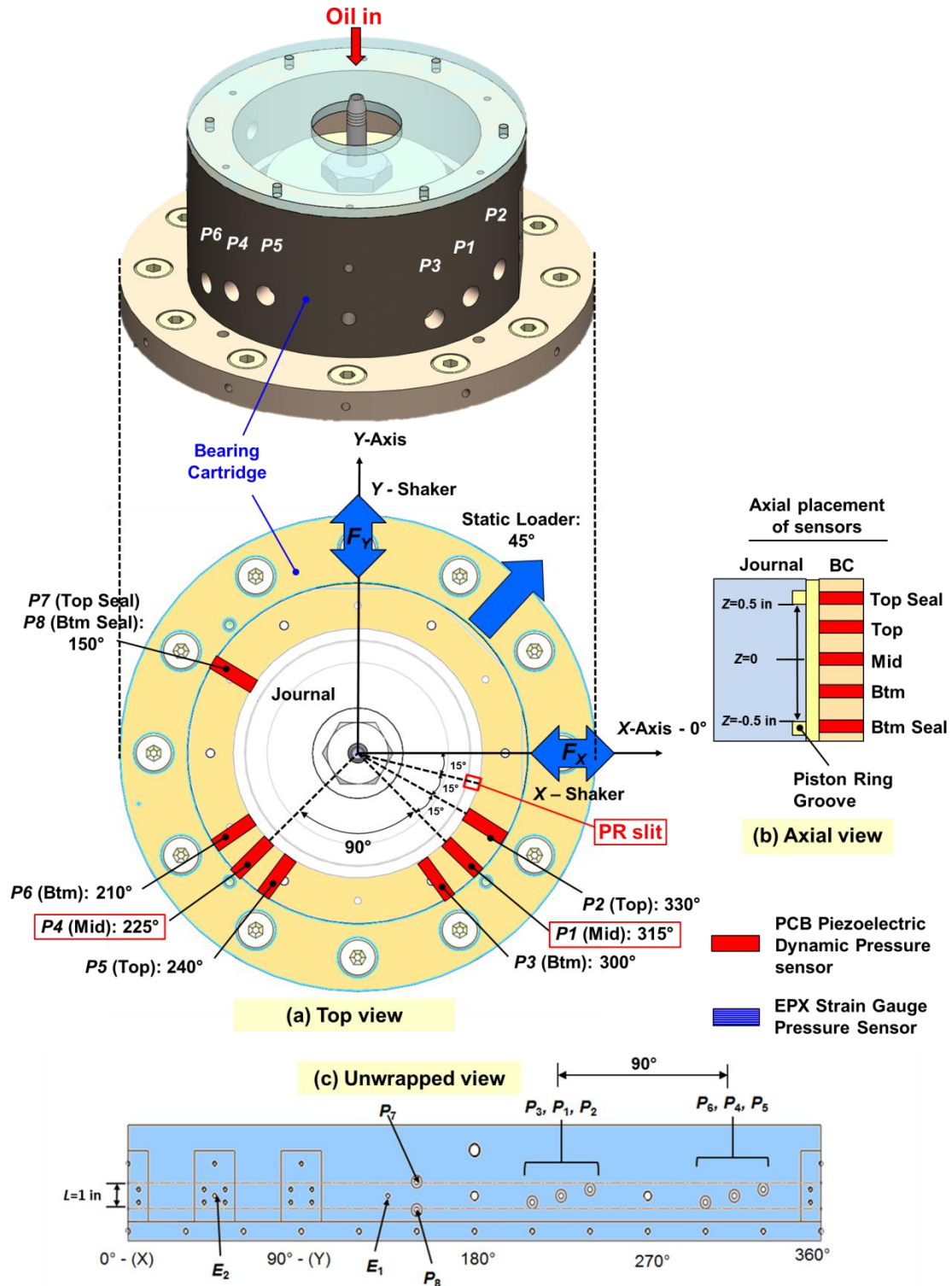


Figure 19. Schematic views of the disposition of pressure sensors in the BC: (a) top view, (b) axial view and (c) unwrapped view [5].

For both configurations, an increase in whirl frequency produces an increase in  $p$ - $p$  dynamic film pressures. Dynamic  $p$ - $p$  pressures for the sealed ends damper A are roughly ten to fifteen times higher than the  $p$ - $p$  pressures for the open ends damper A, in particular at  $\omega > 50$  Hz (see Fig.20(c)). Moreover, the disparity in the  $p$ - $p$  dynamic pressure between the sealed and open ends damper increases with whirl frequency. The comparison demonstrates that the piston ring seals, by restricting the axial flow, effectively increase the generation of dynamic pressures in the film land. Notice that for an open ends condition, the film pressures at the end grooves ( $z = \pm \frac{1}{2}L$ ) are not nil, they are ~20% of the  $p$ - $p$  pressures at the mid-plane. Ref. [5] details the analysis for dynamic pressure generation at the end grooves of an open ends SFD.

Expectedly, the top and bottom film pressures ( $z = \pm 0.25$  in.) are similar in magnitude; and at the mid-plane ( $z = 0$  in.) the pressures  $P_1$  and  $P_4$  are also similar in magnitude. The comparisons between top and bottom  $p$ - $p$  pressures demonstrate that the top and bottom film lands are similar in operating film clearances and thus the bearing cartridge (BC) is properly aligned.

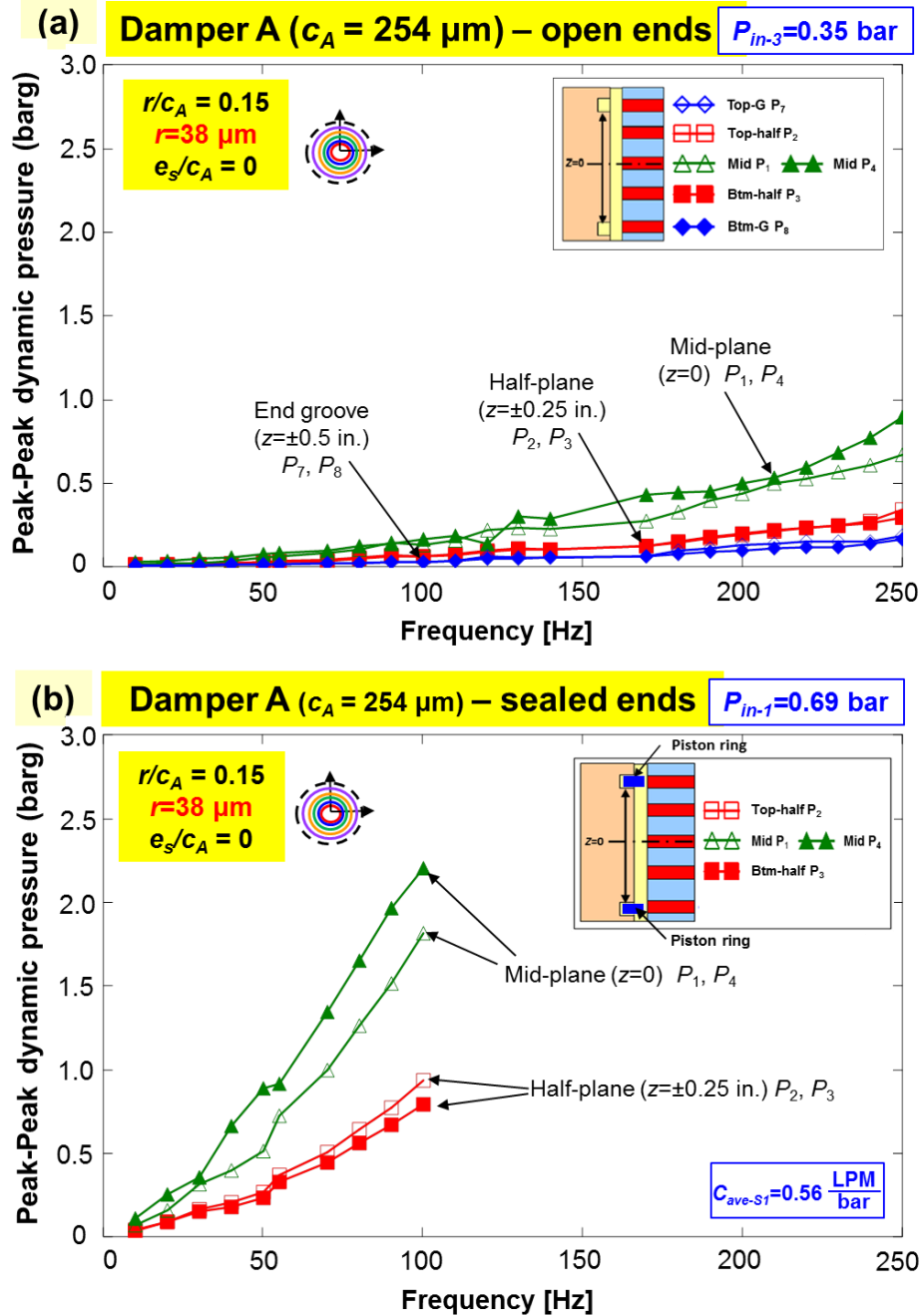


Figure 20. Recorded *peak-to-peak* film dynamic pressures versus excitation frequency ( $\omega$ ) for (a) open ends damper A, (b) sealed ends damper A, and (c) ratio of *p-p* dynamic pressure,  $P_{sealed}/P_{open}$ . Circled pressures indicate high whirl frequency  $\omega > 60 \text{ Hz}$ . Centered ( $e_s = 0$ ) circular orbit tests with radius  $r/c_A = 0.15$ . Measurements at damper mid-plane, top and bottom (half-planes) and end grooves. (Inset shows location of pressure sensors).

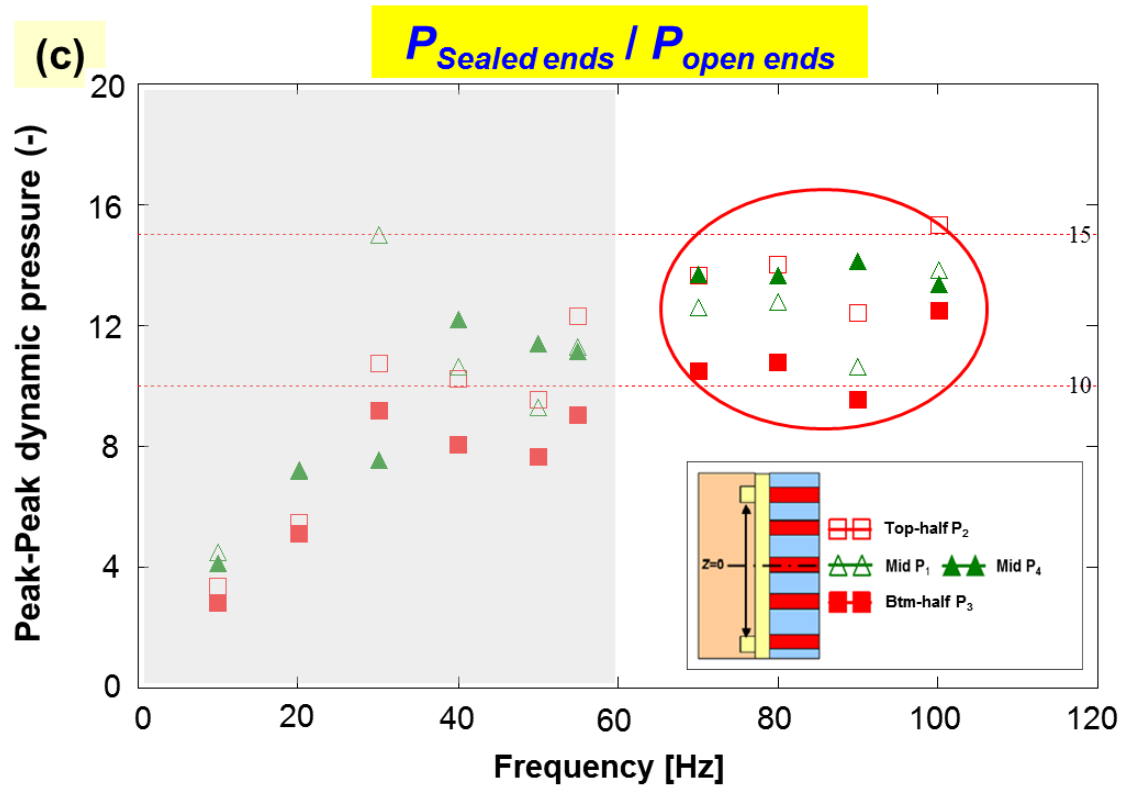


Figure 20. Continued.

Figure 21 shows the peak-to-peak dynamic film pressure at the top ( $z=1/2 L$ ), bottom ( $z=-1/2 L$ ), and mid plane ( $z=0$ ) versus whirl frequency ( $\omega$ ) for the sealed ends damper supplied with a higher lubricant pressure  $P_{in-2}=2.76$  bar. The data corresponds to circular centered orbits with an amplitude of  $r/c_A=0.15$  ( $e_s=0$ ). An increase in frequency ( $\omega$ ) results in an increase in  $p$ - $p$  pressure. The  $p$ - $p$  pressures from operation with the two oil supply pressures  $P_{in-1}=0.69$  bar (Fig.20 (b)) and 2.76 bar (Fig.21) are similar in magnitude.

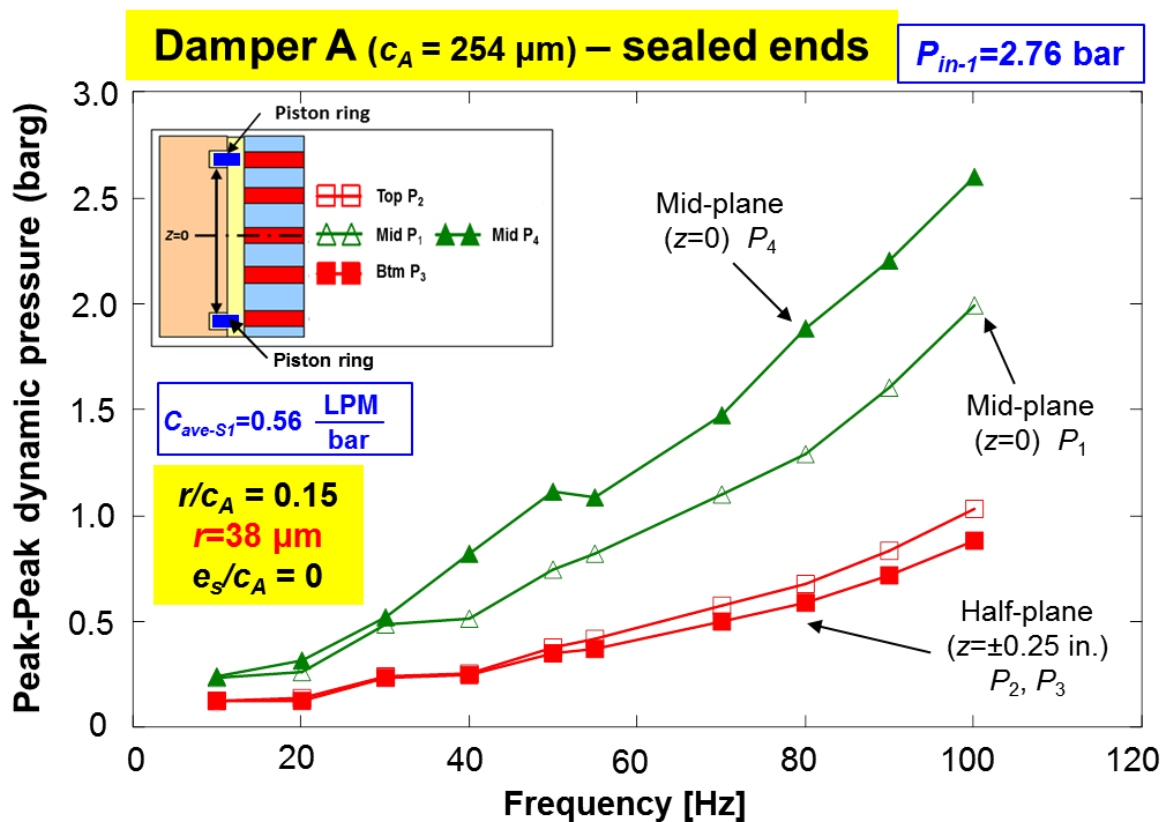


Figure 21. Recorded *peak-to-peak* film dynamic pressures versus excitation frequency ( $\omega$ ) for sealed ends damper A. Centered ( $e_s=0$ ) circular orbit tests with radius  $r/c_A=0.15$ . Measurements at damper mid-plane, top and bottom (half-planes) and end grooves. (Inset shows location of pressure sensors).

For the damper operating with either supply pressure ( $P_{in-1}$  and  $P_{in-2}$ ) undergoing circular centered orbits ( $e_s=0$ ), Figure 22 shows the  $p-p$  dynamic pressures recorded at the mid-plane ( $z=0$ ) versus whirl frequency ( $\omega$ ) as well as increasing orbit radius ( $r$ ). Expectedly, increasing the orbit radius produces an increase in *peak-peak* fluid film pressure. For small to moderate orbit radii  $r/c_A \leq 0.30$ , the  $p-p$  pressures for the sealed ends SFD with both  $P_{in-1}$  and  $P_{in-2}$  are similar in magnitude. However, for moderate to large amplitude motion  $r/c_A \geq 0.45$  and at high whirl frequency  $\omega > 60$  Hz, the sealed ends damper supplied with large pressure  $P_{in-2}$  provides  $\sim 25\%$  higher  $p-p$  pressures than those for the damper operating with  $P_{in-1}$ .

Figure 23 reveals the ratio of the peak-peak dynamic pressures for the two lubricant supply pressures ( $\frac{P_{sealed} : P_{in-2} = 2.76 \text{ bar}}{P_{sealed} : P_{in-1} = 0.69 \text{ bar}}$ ). The data corresponds to circular centered orbits ( $e_s=0$ ) with an amplitude of  $r/c_A=0.60$ . In general, the sealed ends damper with large oil supply pressure  $P_{in}=2.76$  bar generates  $\sim 20\%$  larger  $p-p$  dynamic film pressure. The ratio of  $p-p$  pressures tends to increase with whirl frequency, in particular at high whirl frequency<sup>3</sup>  $\omega > 60$  Hz. This is attributed to the prevention of oil cavitation in the film land due to a large supply pressure.

---

<sup>3</sup> Note that for low whirl frequency  $\omega < 50$  Hz, the  $p-p$  dynamic pressure is small which has less physical meaning compared to those of high whirl frequency  $\omega > 60$  Hz, but still shows  $p-p$  ratio ( $P_{in-2}/P_{in-1}$ ) $\sim 1$ .

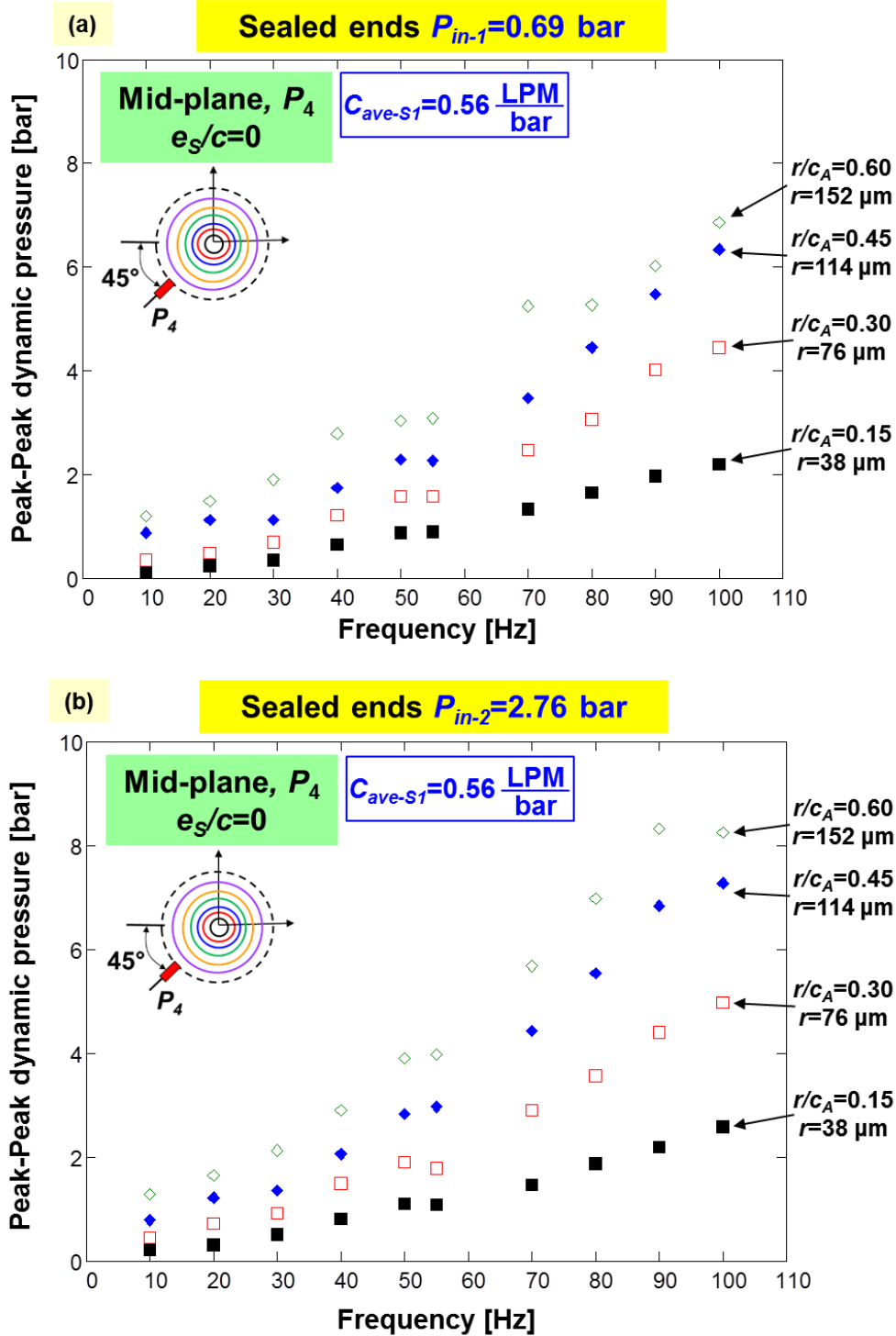


Figure 22. Measured film *peak-peak* pressures ( $P_4$ ) at mid-plane ( $z=0$ ) versus whirl frequency ( $\omega$ ) for increasing orbit radii ( $r$ ): Sealed ends damper with lubricant supply pressure (a)  $P_{in-1}=0.69$  bar and (b)  $P_{in-2}=2.76$  bar. Centered condition ( $e_s=0$ ).

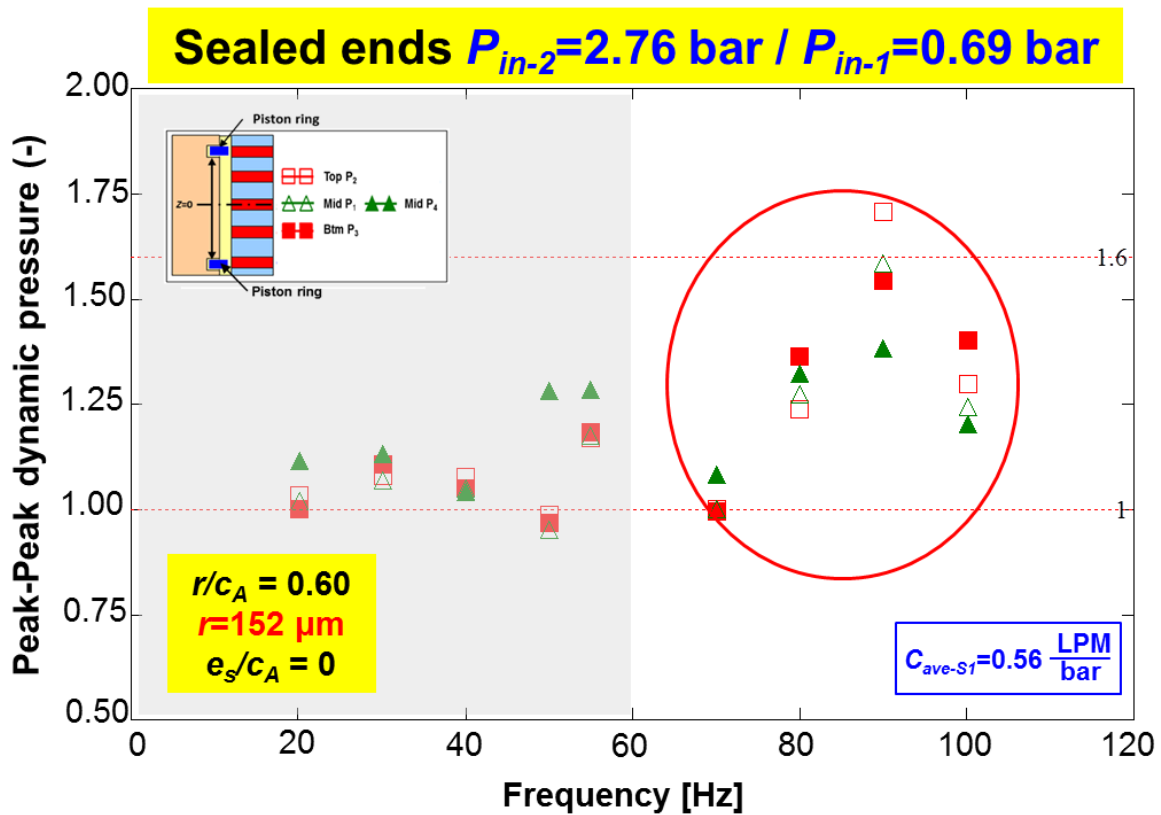


Figure 23. Ratio of recorded *peak-to-peak* film dynamic pressures,  $P_{sealed}$ :  $P_{in-2}=2.76$  bar/ $P_{in-1}=0.69$ bar, versus excitation frequency ( $\omega$ ) for sealed ends damper A. Centered ( $e_s=0$ ) circular orbit tests with radius  $r/c_A=0.60$ . Circled pressures indicate high whirl frequency  $\omega>60$ Hz. Measurements at damper mid-plane, top and bottom (half-planes) and end grooves. (Inset shows location of pressure sensors).

Note that during the tests with the sealed ends SFD ( $C_{ave-S1}=0.56$  LPM/bar) supplied with a low pressure ( $P_{in-1}=0.69$  bar) operating at a large amplitude motion  $r/c_A>0.45$  and at high whirl frequency  $\omega>60$  Hz, visual inspection of the oil collectors at the damper top and bottom discharge sections reveals a foamy-bubbly air-in-oil mixture that can be described as a murky oil.

Figure 24(a) displays the phenomenon for a test with sealed ends damper operating  $P_{in-1}=0.69$ ,  $r/c_A>0.45$  and  $\omega=80$  Hz. Note that the foamy-mixture leaks first at the piston ring slit ( $\Theta=345$  deg) and extends towards the oil outlet ( $\Theta=150$  deg). Hence, oil cavitation persists on the sealed ends SFD configuration operating with a low lubricant supply pressure  $P_{in-1}=0.69$  psig. The red dashed line indicates the location of piston ring slit.

On the other hand, the same damper with ~4 times higher lubricant supply pressure  $P_{in-2}=2.76$  bar did not show signs of bubbly air-oil mixture (murky oil) in lubricant as seen in Fig 24(a). Note that the oil leakage through the ring slit generates air bubbles at the surface of the top oil collector, but these bubbles are not an air-oil mixture.

For further illustration, please watch the video (<https://www.youtube.com/watch?v=PulQisPDRtY>) showing how the bubbly mixture extends with time for operation with two lubricant supply conditions.

Top oil collector  
 $r/c_A=0.45$ ,  $\omega=80\text{Hz}$

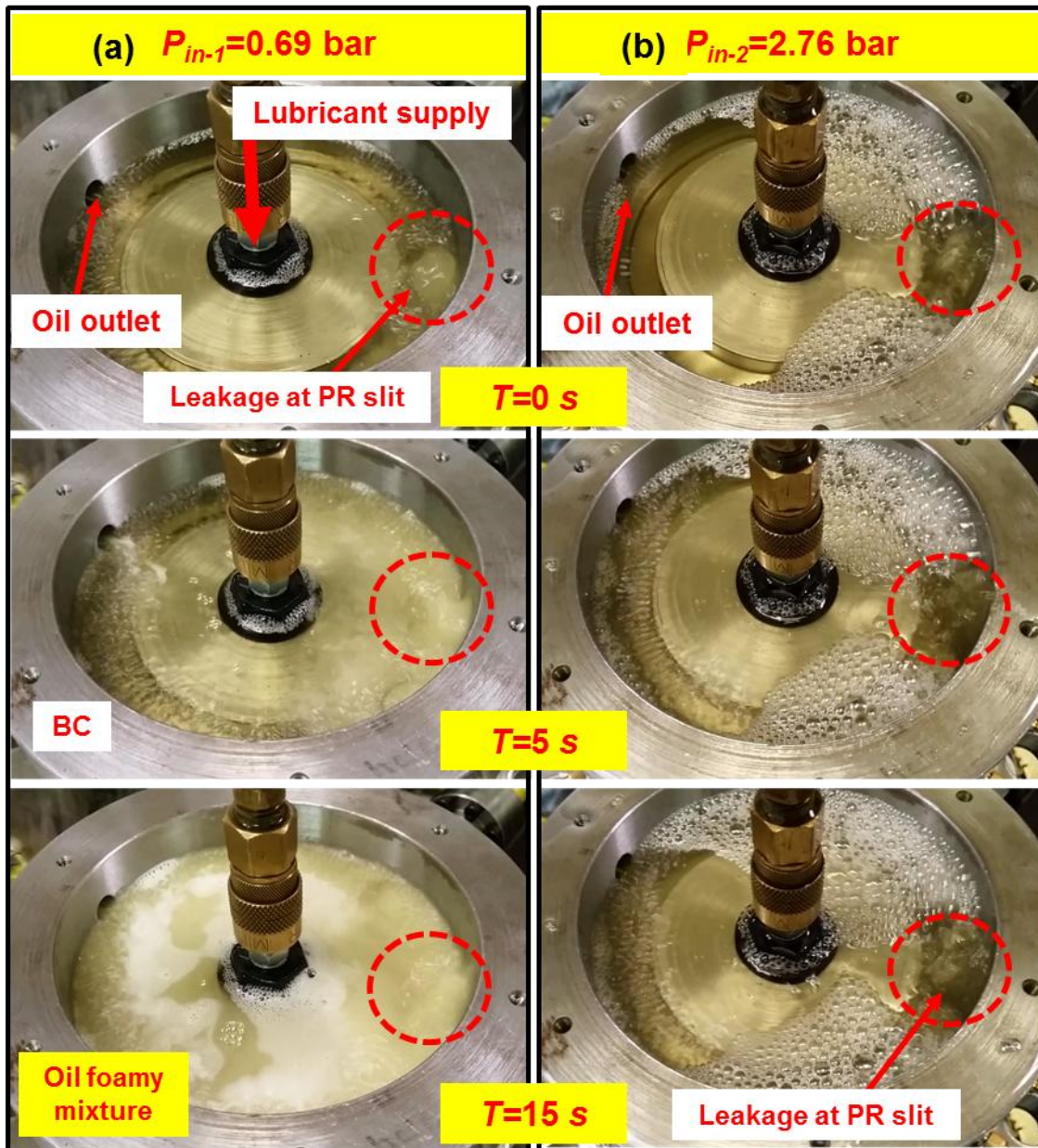


Figure 24. Photographs of the top oil collector showing the lubricant exit condition. Sealed ends damper sections for whirl motions with  $r/c_A=0.45$  and  $\omega=80$  Hz with lubricant supply pressure (a)  $P_{in-1}=0.69$  bar and (b)  $P_{in-2}=2.76$  bar. Top figures: elapse time  $T=0$  s. Middle figures: elapse time  $T=5$  s. Bottom figures: elapse time  $T=15$  s. (Pictures taken on October 9, 2015). <https://www.youtube.com/watch?v=PulQisPDRtY>

## Examples of Recorded Squeeze Film Dynamic Pressures Profiles<sup>4</sup>

Figure 25 depicts the recorded squeeze film dynamic pressures (at  $z=0$ ) and the film thickness for the sealed ends damper with two distinct lubricant supply pressure  $P_{in-1} \sim 0.69$  barg ( $Q_{in-1}=0.68$  LPM) and  $P_{in-2} \sim 2.76$  barg ( $Q_{in-2}=2.68$  LPM) operating with circular centered orbits with amplitudes  $r/c_A=0.30, 0.45$  and  $0.60$  and whirl frequency  $\omega=90$  Hz. Note that the end seal flow conductance is  $C_{ave-S1}=0.56$  LPM/bar.

The figure shows the recorded pressure data for three periods of whirl motion ( $T_P=2\pi/\omega=0.011$  s) as recorded by sensor  $P_4$  ( $\Theta=225^\circ$ , see Fig. 22). The film thickness is calculated as

$$h_{(\Theta,t)} = c + X_{(t)} \cos \Theta + Y_{(t)} \sin \Theta \quad (12)$$

$$\begin{aligned} X_{(t)} &= r_x \cos(\phi_x + \omega t) + e_s \cos\left(\frac{\pi}{4}\right) \\ Y_{(t)} &= r_y \cos(\phi_y + \omega t) + e_s \sin\left(\frac{\pi}{4}\right) \end{aligned} \quad (13)$$

where  $e_s$  is the static eccentricity along ( $\Theta=45^\circ$ );  $r_x, r_y$  are the magnitude along the  $X, Y$  directions, and  $\phi_x, \phi_y = \phi_x + \frac{1}{2} \pi$ , are the arguments of the fundamental components of the Fourier series built functions from the measured displacements along the  $X, Y$  axes.

In Figure 25, the dynamic pressures increase with an increase in orbit amplitude ( $r$ ) and are periodic in nature. Importantly enough, with increasing orbit amplitude ( $r$ ), the sealed ends damper with higher oil supply pressure  $P_{in-2}=2.76$  bar provides larger dynamic pressures than that of  $P_{in-1}=0.69$  bar. At moderate to large orbit amplitude motions of  $r/c_A \geq 0.3$ , this difference is due to the presence of air in the lubricant film land for the sealed ends damper with lower  $P_{in-1}$ . Interestingly enough, for sealed ends damper with smaller oil leakage  $C_{ave-S1}=0.56$  LPM/bar and with motion amplitudes  $r/c_A=0.6$ , the *peak-peak* dynamic film land pressure reaches  $\sim 8.5$  barg that is,  $\sim 8.5$  times the ambient pressure (1 bar).

The pressure shows high frequency spikes indicating the presence of air while the fluctuations persist into the positive pressure zone and evidencing the collapse of air/gas bubbles. Note the negative pressure zone ends with a shape typical of oil vapor cavitation [8,31,32]. Eventually, a foamy-bubbly air-oil mixture exits through the piston rings slit

<sup>4</sup> Portions of this section reproduce ad-verbatim information presented in Ref. [5].

resulting to that shown in the visual inspection in Fig. 24. It is important to note, however, that the oil in the test rig has an unknown amount of dissolved air.

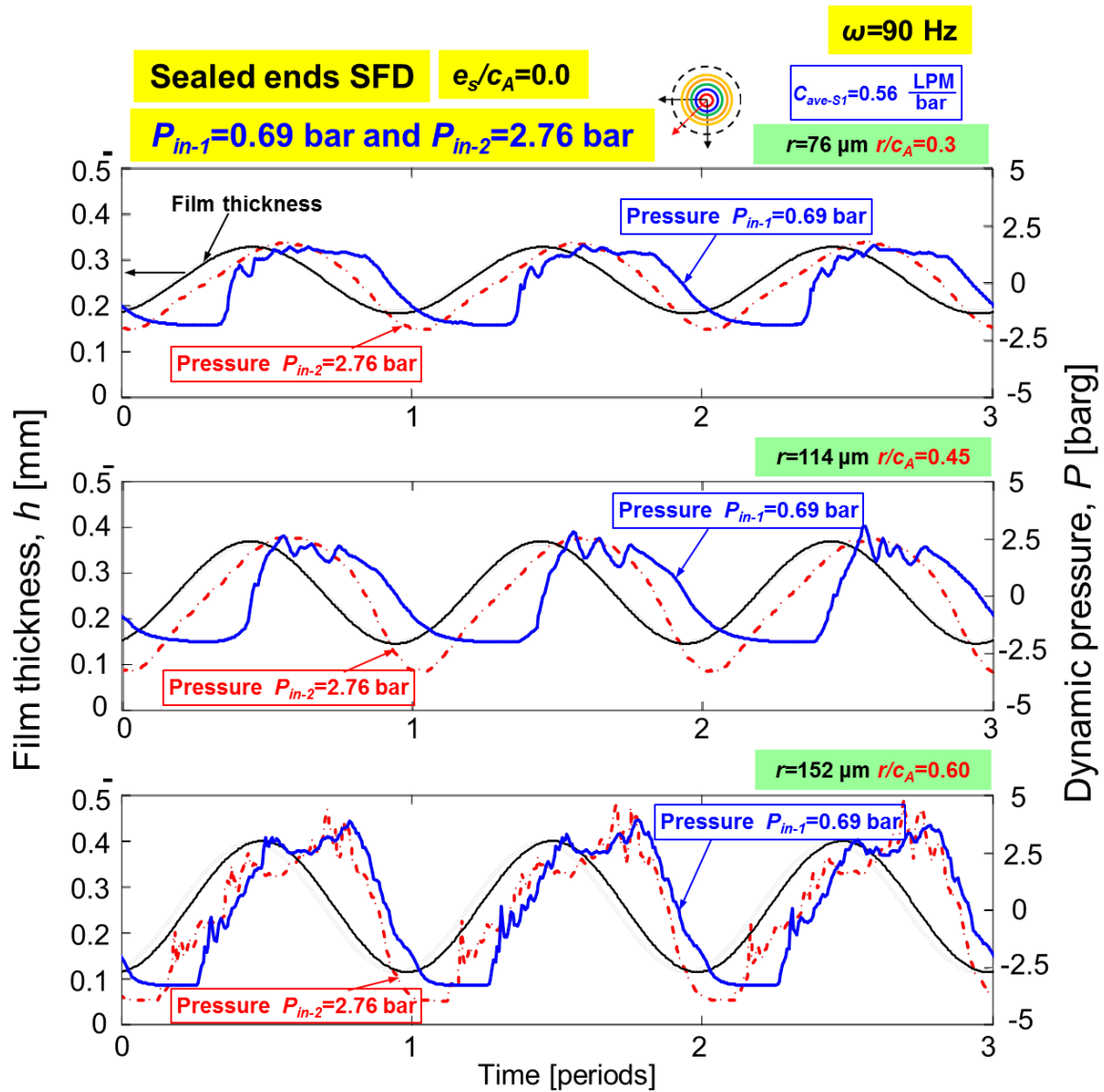


Figure 25. Sealed ends damper with lubricant supply pressure  $P_{in-1} = 0.69$  bar and  $P_{in-2} = 2.76$  bar: Dynamic film pressures ( $P$ ) and film thickness ( $h$ ) recorded at  $\Theta = 225^\circ$  versus time ( $t/T$ ) for measurements at mid-plane ( $z = 0$ ). Circular centered orbit with frequency  $\omega = 90$  Hz. Graphs show data for orbits with magnitude  $r/c_A = 0.30$ ,  $0.45$  and  $0.60$ . (nominal clearance  $c_A = 254$   $\mu\text{m}$ ).

Figure 26 shows the measured dynamic pressure and the film thickness for both the open and sealed ends dampers, respectively. Note the pressure for the open ends SFD is multiplied by 10 for better visualization. For damper A ( $c_A=254 \mu\text{m}$ ), the sealed ends configuration generates ~12-15 times larger peak-peak dynamic pressures than those in the open ends configuration. Recall the sealed ends damper ( $C_{ave-S1}=0.56 \text{ LPM/bar}$ ) generates ~13 times larger damping and ~11 times more inertia coefficients than those of open ends.

The graphs in Fig. 26 illustrate the change in phase angle between the peak (+) pressure relative to the location of maximum film thickness. In general, the open ends SFD shows a peak pressure after the location of maximum squeeze velocity,  $|dh/dt|$ , while the sealed ends SFD shows a much broader pressure profile that does not resemble the classical lubrication shape.

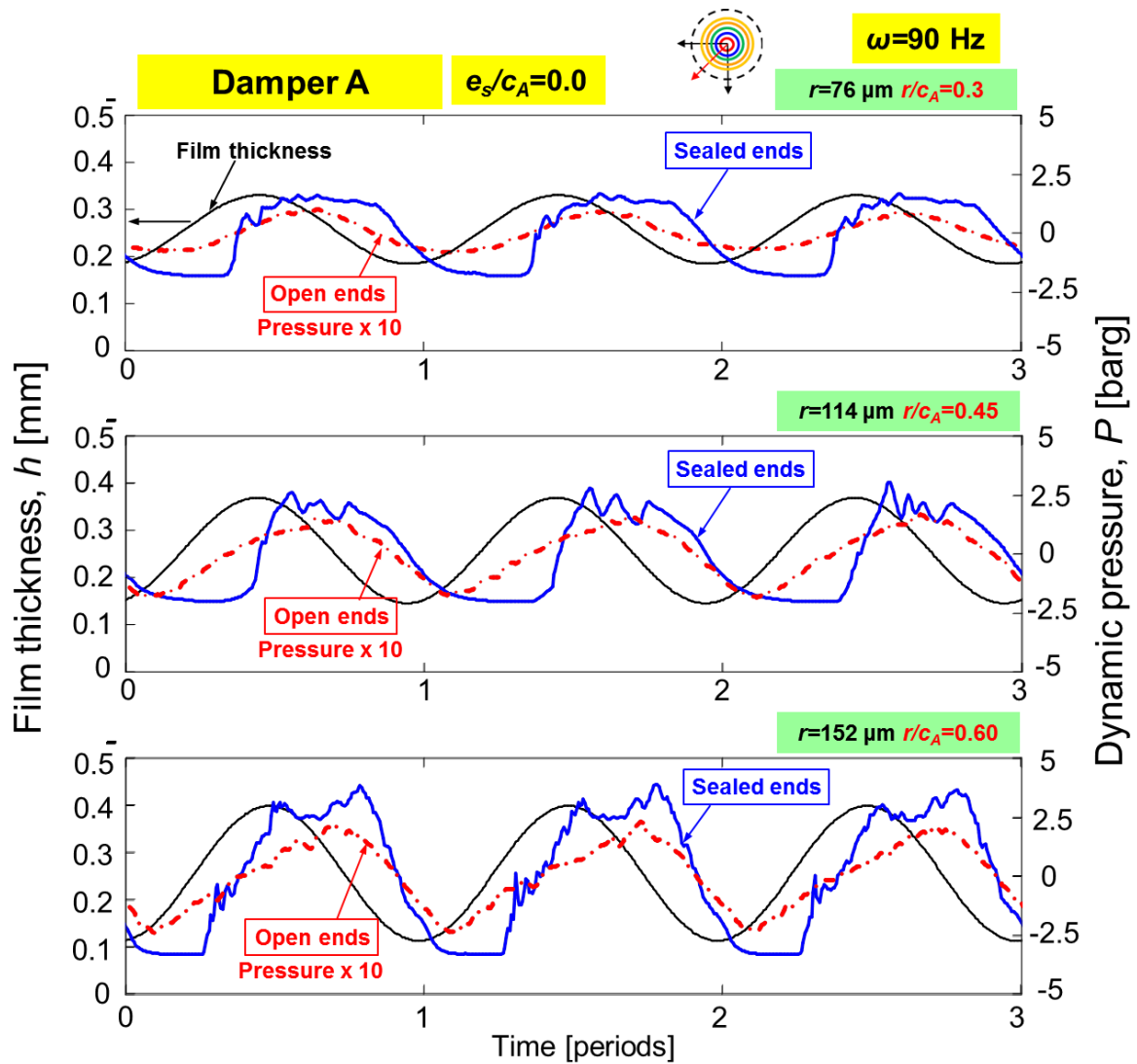


Figure 26. **Damper A with sealed ends and open ends:** Dynamic film pressures ( $P$ ) and film thickness ( $h$ ) recorded at  $\Theta=225^\circ$  versus time ( $t/T$ ) for measurements at mid-plane ( $z=0$ ). Circular centered orbit with frequency  $\omega=90$  Hz. Graphs show data for orbits with magnitude  $r/c_A=0.30, 0.45$  and  $0.60$ . Pressure for the open ends SFD is multiplied by 10 for better visualization. (nominal clearance  $c_A=254$   $\mu\text{m}$ , pressure supply at  $P_{in-1}\sim 0.69$  barg for sealed ends damper and at  $P_{in-3}\sim 0.35$  barg for open ends damper).

## Predicted Versus Experimental SFD Force Coefficients

This section presents predictions from *orbit analysis* [7] and comparisons results against the experimentally identified SFD force coefficients. Recall that the computational physics model implements a Finite Element Method (FEM) to solve an modified Reynolds equation that includes temporal fluid inertia effects [17,18], i.e.,

$$\frac{\partial}{\partial x} \left( h^3 \frac{\partial P}{\partial x} \right) + \frac{\partial}{\partial z} \left( h^3 \frac{\partial P}{\partial z} \right) = 12\mu \frac{\partial h}{\partial t} + \rho h^2 \frac{\partial^2 h}{\partial t^2} \quad (14)$$

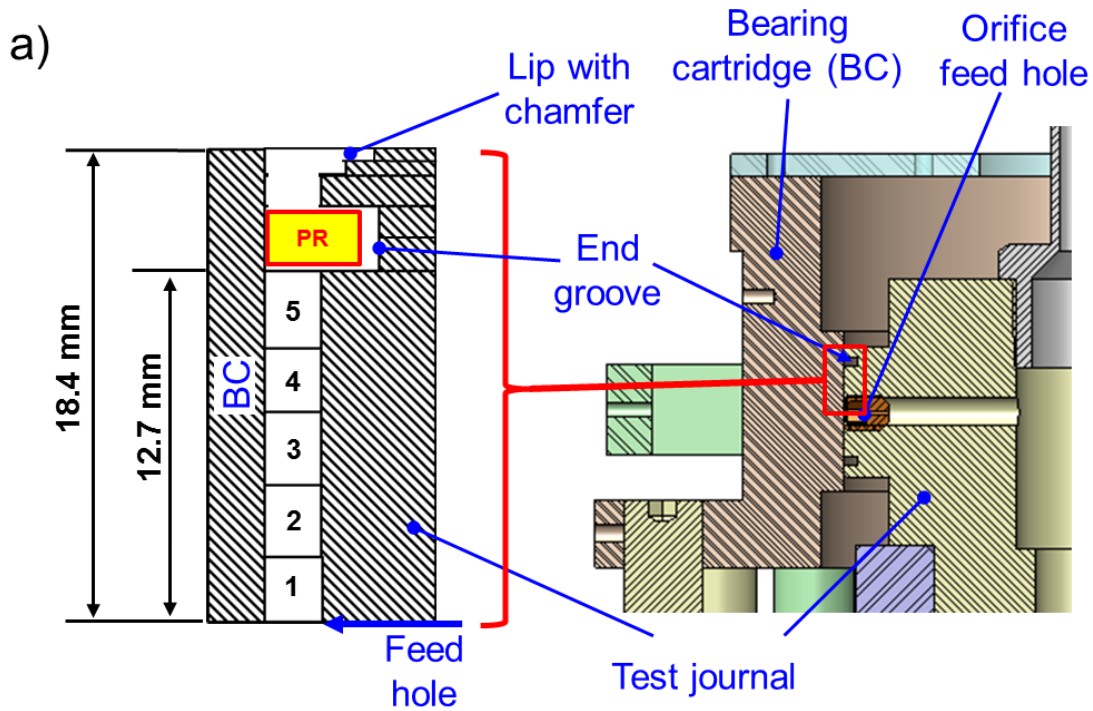
where  $P$ ,  $\mu$ , and  $\rho$  are film pressure, lubricant viscosity and density, respectively. Note the model satisfies flow continuity at the intersection between a groove and a film land.

Table 5 lists the physical parameters to obtain predictions of the SFD dynamic force coefficients for the sealed ends configuration. Figure 27 depicts schematic views of the SFD test rig and the damper axial film length and radial clearance as modeled in computational program. The piston ring seals are installed at the top and bottom ends grooves of the journal. Due to symmetry, only half of the damper axial length needs to be modeled. Five elements model half of the axial film land length and 121 elements model the circumference of the damper. The computational model best reproduces the experimental dynamic pressure when the lubricant gaseous cavitation pressure is set to  $P_{cav}=-1$  barg, i.e.,  $P_{cav}=0$  bar (absolute).

**Table 5. Dimensions of open ends SFD with large clearance ( $c_A=254 \mu\text{m}$ ). Three feed holes ( $\phi=2.5 \text{ mm}$ ) at damper mid-plane ( $120^\circ$  apart)**

Parameter	Value	Units
Journal Diameter, $D$	127 (5)	mm (inch)
Nominal Axial Film Land Length, $L$	25.4 (1.00)	mm (inch)
Nominal Radial Clearance, $c$	0.254 (10)	mm (mil)
Ambient pressure at ends	0.0	barg (psig)
Supply pressure, $P_{in}$	0.69 (10) or 2.76 (40)	barg (psig)
Flow conductance, $\bar{C}_{seal-1} = \frac{C_{ave-S1}}{\pi D}$	$2.34 \times 10^{-4}$ ( $2.49 \times 10^{-3}$ )	( $\text{mm}^2/(\text{s} \cdot \text{Pa})$ ) ( $\text{in}^2/(\text{s} \cdot \text{psig})$ )
Seal conductance, $C_{ave-S1}$	0.56	LPM/bar
Cavitation pressure, $P_{cav}$	-1.0 (-14.5)	barg (psig)
Supply Temperature, $T_S$	23 (73)	$^\circ\text{C}$ ( $^\circ\text{F}$ )
Viscosity <sup>5</sup>	2.60 (0.377)	cP (micro-Reyns)
Density	799 (49.9)	$\text{kg/m}^3$ ( $\text{lb/ft}^3$ )

<sup>5</sup> Please see Appendix B for further details.



**b) Damper A ( $c_A = 254 \mu\text{m}$ ) – sealed ends**

Element #	1	2	3	4	5	End groove
Axial length [mm]	2.54	2.54	2.54	2.54	2.54	Piston Ring
Clearance [mm]	0.254	0.254	0.254	0.254	0.254	

\*Circumferential direction: 121 elements

**Figure 27. (a) Depiction of SFD test rig section and elements to model half the damper axial length. Elements 1-5: film land (axial).**

The computational program performs an *orbit analysis* [7] process to estimate the SFD force coefficients. This feature numerically reproduces the actual test conditions; that is, the program computes the instantaneous damper reaction forces to specific journal amplitude motion ( $r_x, r_y$ ), static eccentricity ( $e_x, e_y$ ) and whirl frequency ( $\omega$ ) in one cycle of whirl motion for a selected range of frequencies as shown in Figure 28. Then, calculated SFD forces (time domain) are transformed into the frequency domain using a Fourier analysis to construct impedance functions ( $\mathbf{H}$ ). SFD force coefficients ( $K, C, M$ ) are identified by curve fitting the real and imaginary parts of the impedance over a designated frequency range; that is,  $\text{Re}(\mathbf{H}) \rightarrow \mathbf{K} - \omega^2 \mathbf{M}$ ,  $\text{Im}(\mathbf{H}) \rightarrow C\omega$ .

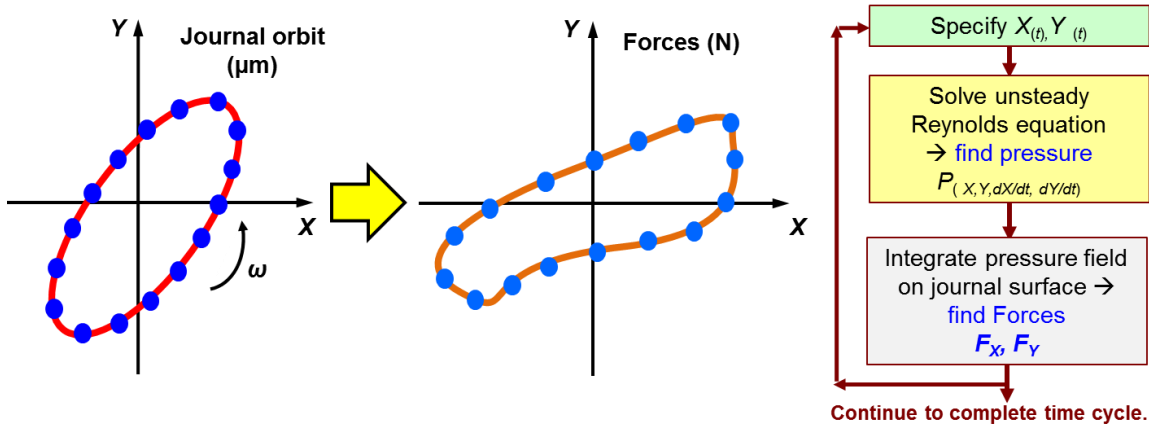


Figure 28. (a) Example of analysis for an elliptical off-centered orbit: journal motion  $X$  versus  $Y$  and fluid film bearing reaction forces ( $F_X$  versus  $F_Y$ ). Dots indicate discrete points at which the numerical program predicts forces and (b) illustration of algorithm flow chart [7].

### Predictions based on Classical Lubricant Theory

Classical Lubrication Theory for an open ends, full film SFD (i.e., without oil cavitation), predicts damping and inertia force coefficients [1] as

$$C_{XX-Open\ ends} = C_{YY-Open\ ends} = \pi \frac{\mu R L_{eff}^3}{c^3} = 0.9 \frac{\text{kN}\cdot\text{s}}{\text{m}}, \quad (15)$$

$$M_{XX-Open\ ends} = M_{YY-Open\ ends} = \pi \frac{\rho R L_{eff}^3}{12c^3} = 1.4 \text{kg}$$

The simple model does not account for any feeding hole(s). It is noteworthy to realize that the simple equation use an effective film length  $L_{eff}$ . As detailed in Ref.[5],  $L_{eff}$  accounts the pressure generation at the end grooves  $L_{eff} >$  than the design film land length  $L=25.4$  mm and shorter than the actual wetted length  $L_{tot}=36.8$  mm.

Figure 29 depicts the predicted SFD direct damping and added mass force coefficients versus end seal flow conductance ( $\bar{C}_{seal}$ ) and flow rate ( $Q_{in}$ ). The predictions correspond to a circular orbit amplitude of  $r/c_A=0.15$  about a centered condition ( $e/c_H=0$ ), where cross-coupled force coefficients are negligible as shown in the experimental results. Both the damping and inertia force coefficient increase with a decreasing flow conductance, i.e., decreasing flow rate through the piston ring seal.

The end seals flow conductances ( $\bar{C}_{seal-1}$  and  $\bar{C}_{seal-2}$ ) are overlaid with the predictions. As the seal flow conductance increases both the damping and added mass force coefficients decrease until they reach the open ends SFD condition. Note that for  $\bar{C}_{seal}$  values  $< 4.0 \cdot 10^{-4} \frac{\text{mm}^2}{\text{s} \cdot \text{Pa}}$ , both damping and inertia coefficients do not increase significantly. Additionally, notice that the predicted added mass coefficients for  $C_{ave-S1}$  and  $C_{ave-S2}$  fell short by ~30% of the experimental added mass coefficients,  $M_{SFD} \approx 37$  kg. Further discussion follows when presenting Figure 30.

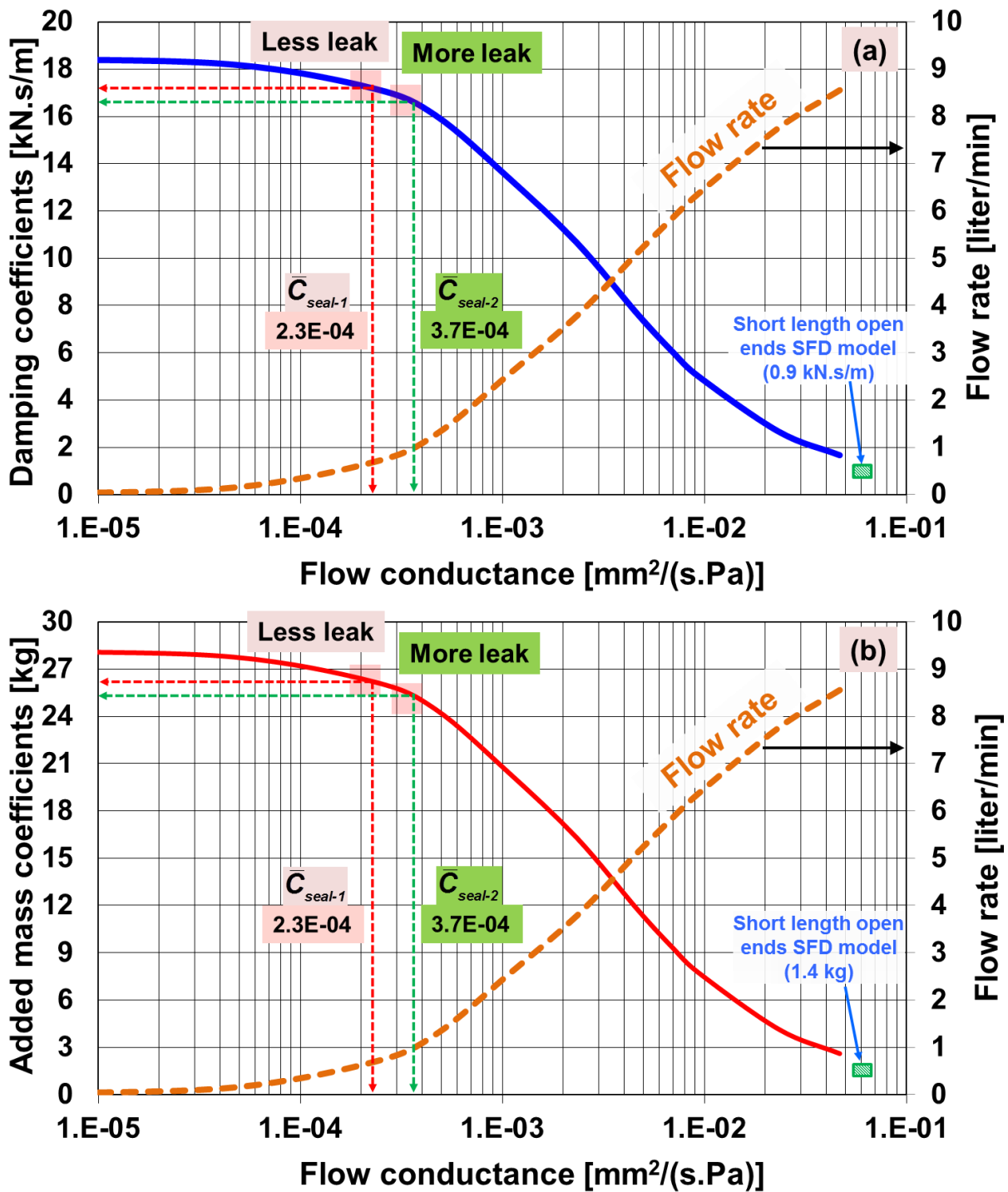


Figure 29. Predicted SFD dynamic force coefficients versus end seal flow conductance and flow rate: (a) damping ( $C_{XX}=C_{YY}$ )<sub>SFD</sub> and (b) mass ( $M_{XX}=M_{YY}$ )<sub>SFD</sub> coefficients. Lubricant supply pressure  $P_{in-1}=0.69$  bar. End seal flow conductance labeled  $\bar{C}_{seal-1}=2.34 \cdot 10^{-4} \text{ mm}^2/(\text{sPa})$  and  $\bar{C}_{seal-2}=3.70 \cdot 10^{-4} \text{ mm}^2/(\text{sPa})$ . Test data shown in symbols.

Figures 30 and 31 show comparisons of the experimental and predicted damping ( $C$ ) and added mass ( $M$ ) coefficients identified over the frequency range 10 – 100 Hz from small to large amplitude whirl motions ( $r/c_A=0.15 - 0.60$ ) at the centered position ( $e_s/c_A=0$ ). In Figures 30 and 31, notice the difference in oil feed pressures set at  $P_{in-1}\sim 0.69$  barg and  $P_{in-2}\sim 2.76$  barg for operation. The figures also includes predictions from Eq.(15) for an open ends SFD ( $e_s=0$ ).

With a low lubricant supply pressure  $P_{in-1}\sim 0.69$  barg, (as shown in Figure 30) the predicted damping force coefficients show an opposite trend of the test coefficients with increasing whirl motion amplitude ( $r$ ). That is, predicted  $C_{XX}$  and  $C_{YY}$  first decrease as the whirl amplitude grows to  $r/c_A<0.3$ , then remain constant above  $r/c_A>0.3$ . On the other hand, the experimental damping coefficients show an increase with orbit amplitude  $r$ .

Both predicted and experimental added mass coefficients ( $M_{XX}$ ,  $M_{YY}$ ) decrease with the whirl motion ( $r$ ). The predictions agree well with the test  $M_{XX}$  and  $M_{YY}$  for  $r/c_A>0.15$ ; however, the mass coefficients are under predicted by  $\sim 30\%$  at the small amplitude motion for  $r/c_A=0.15$ .

In Figure 31, for operation with a larger  $P_{in-2}$ , the predicted damping coefficients remain constant with increasing orbit amplitude motions. These trends closely resemble the test results.

The predicted and experimental SFD added mass coefficients ( $M_{XX}$ ,  $M_{YY}$ ) show a large discrepancy from small to large amplitude whirl motions ( $r/c_A=0.15 - 0.60$ ). This difference increases from 30% to 65% with increasing orbit motions. The difference is perhaps due to the physical model neglecting the volume in the three feed holes. These holes amount to  $\sim 15\%$  of the lubricant volume in the film land (see Appendix A) [5].

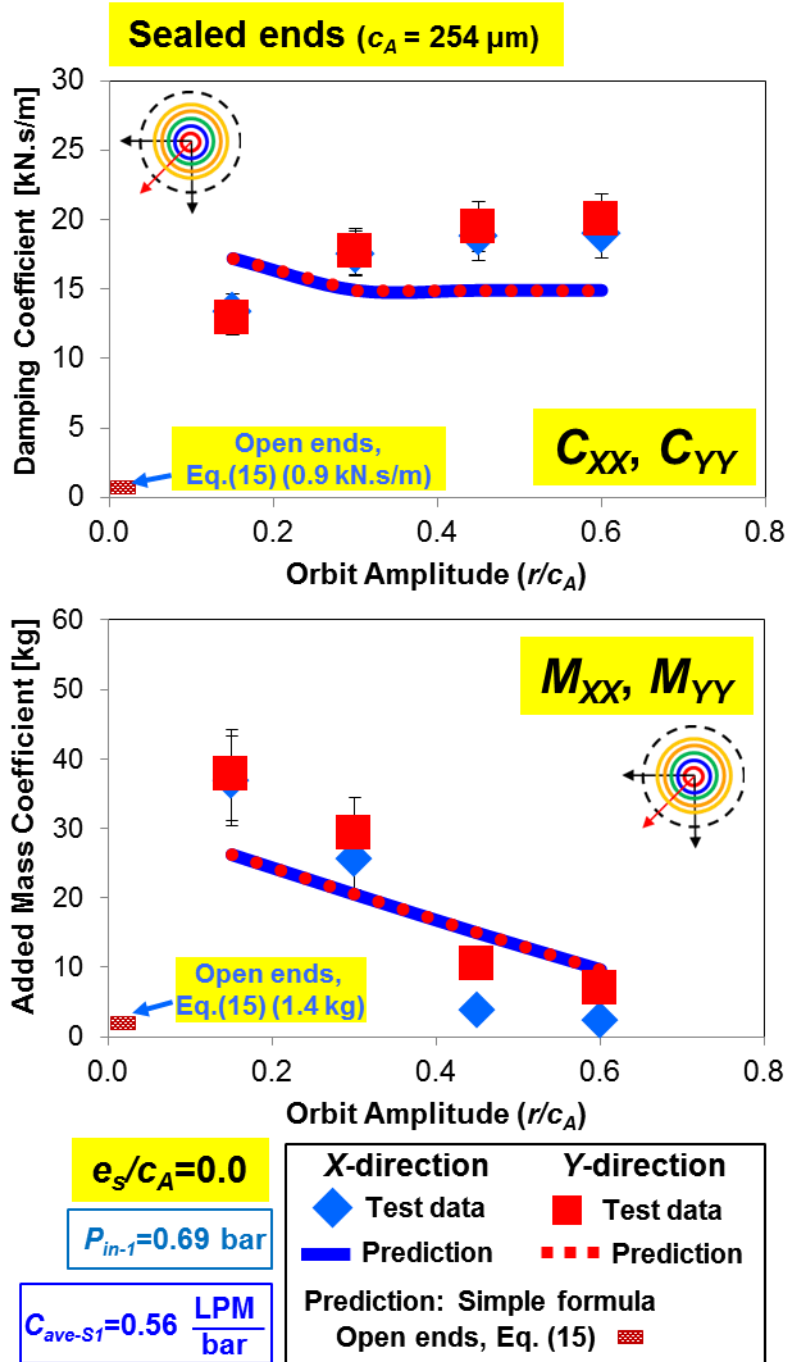


Figure 30. **Sealed ends:** Experimental and predicted SFD direct damping ( $C$ ) and added mass ( $M$ ) coefficients versus amplitude ( $r/c_A$ ) for circular orbits, centered ( $e_s=0$ ) with lubricant supply pressure  $P_{in-1}=0.69 \text{ bar}$ . End seal flow conductance  $C_{ave-S1}=0.56 \text{ LPM/bar}$ .

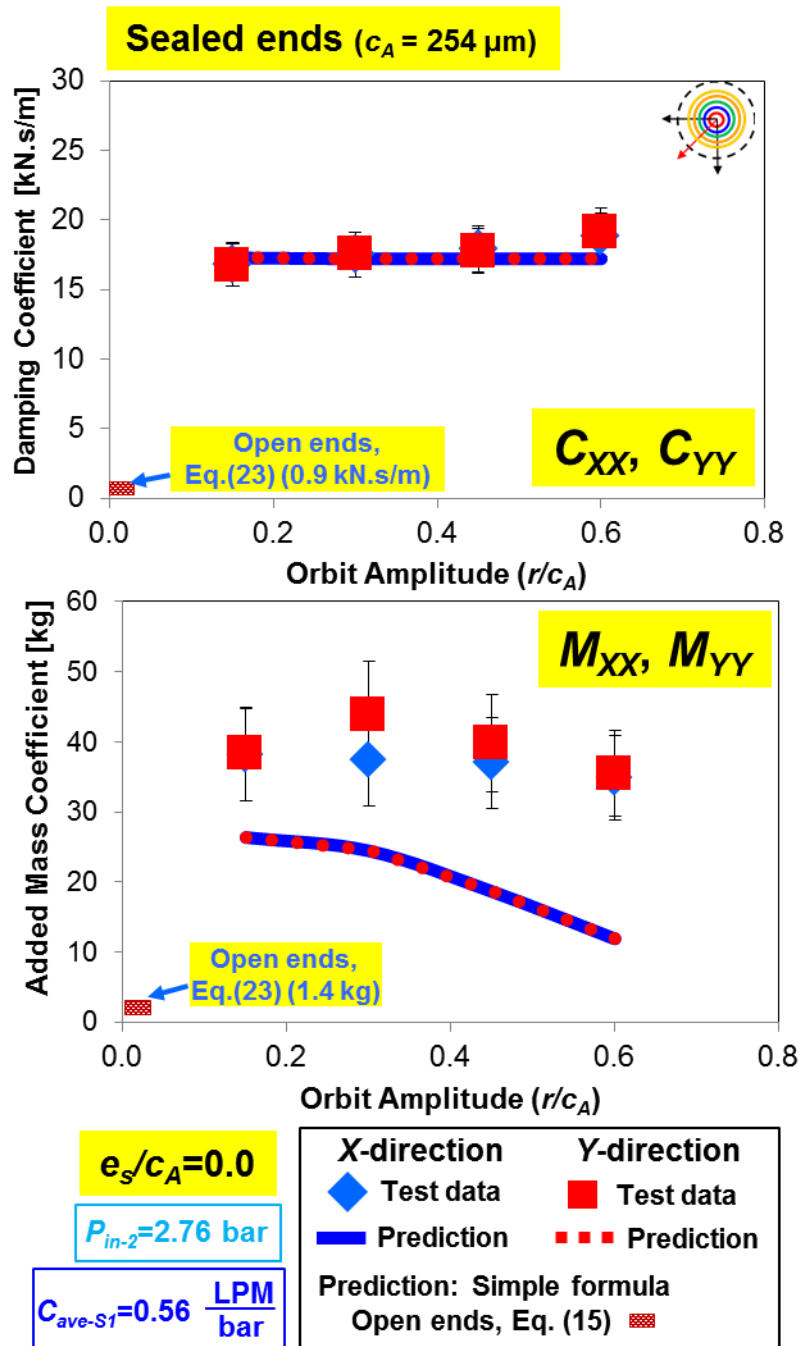


Figure 31. **Sealed ends:** Experimental and predicted SFD direct damping ( $C$ ) and added mass ( $M$ ) coefficients versus amplitude ( $r/c_A$ ) for circular orbits, centered ( $e_s=0$ ) with lubricant supply pressure  $P_{in-2}=2.76 \text{ bar}$ . End seal flow conductance  $C_{ave-S1}=0.56 \text{ LPM/bar}$ .

## Conclusions: Single Frequency Dynamic Loads

The section presented comparison of single frequency dynamic loads tests conducted with both an open ends and a sealed ends SFD. The operating conditions differ in particular for lubricant supply pressure and end seal flow conductance. For the sealed ends SFD, by increasing four times the lubricant supply pressure from  $P_{in-1} \sim 0.69$  barg to  $P_{in-2} \sim 2.76$  barg, the SFD direct damping coefficients do not significantly increase with increasing amplitude of motion ( $r/c_A$ ) while the SFD added mass coefficients show a large increase (see Fig. 15).

For small orbit amplitude  $r/c_A = 0.15$  and for increasing static eccentricity  $e/c_A = 0.0-0.5$ , the sealed ends damper operating with large  $P_{in-2}$  provides  $\sim 26\% - 50\%$  larger direct damping while the inertia coefficients show similar magnitude for both dampers for  $P_{in-1}$  and  $P_{in-2}$  (see Fig. 16).

The piston ring end seals are effective in reducing the side leakage and thus the sealed SFD with  $C_{ave-S1}$  provides 11-13 times more damping and eleven times larger added mass coefficients than the open ends configuration.

The peak-peak dynamic pressures measurements for two lubricant supply pressures show that the tests with large oil supply pressure ( $P_{in-2} = 2.76$  bar) generate  $\sim 20\%$  larger  $p-p$  dynamic film pressure. For increasing orbit amplitude  $r/c_A = 0.15 - 0.60$ , the dynamic pressure measurements and a visual inspection show that the vapor cavitation persists for the sealed ends SFD with a low lubricant supply pressure  $P_{in-1} = 0.69$  psig which most likely leads to a large decrease in direct added mass coefficients.

Numerical predictions agree very well with the experimental damping coefficients while under predicting the added mass coefficients at  $r/c_A = 0.15$ .

## Description of Sine-Sweep Frequency Dynamic Load Tests

Sine-sweep frequency dynamic load tests aim to characterize the forced response of a sealed ends SFD during transient motion events such as with a maneuver load, shocks during a hard landing, and a sudden loss of lift due to air turbulence. Furthermore, the sine-sweep frequency dynamic load tests save time to identify force coefficients compared to single frequency dynamic load tests ( $\alpha=0$ )<sup>6</sup>.

Sine-sweep frequency dynamic load test utilizes a similar procedure to the one described in section ‘Description of Single Frequency Dynamic Load’. That is, the dynamic loads are exerted by the shakers in the  $X$  and  $Y$  directions as

$$\mathbf{F}_{CW} = F \begin{bmatrix} \cos(\phi_{(t)}) \\ \sin(\phi_{(t)}) \end{bmatrix}; \mathbf{F}_{CCW} = F \begin{bmatrix} \cos(\phi_{(t)}) \\ -\sin(\phi_{(t)}) \end{bmatrix} \quad (16)$$

where the angle is  $\phi_{(t)} = \omega_{(t)}t$  with  $\omega_{(t)} = \alpha t + \omega_{start}$ .  $\alpha$  denotes a constant angular acceleration (frequency ramp rate) defined as

$$\alpha = \left( \frac{\omega_{end} - \omega_{start}}{T^*} \right) \quad (17)$$

The variables  $\omega_{start}$  and  $\omega_{end}$  above denote the start and end excitation frequencies and  $T^*$  is the elapsed time of the dynamic load excitation. The sine-sweep dynamic load tests cover the frequency range 5-105 Hz with  $\alpha=6.5$  Hz/s while for single-frequency dynamic loads, the constant angular acceleration is zero ( $\alpha=0$ ).

Table 6 lists the sine-sweep dynamic load tests performed for sealed ends damper A. The sine-sweep frequency dynamic load test that took place produces whirl motions with various sets of static eccentricity ( $e_s/c_A=0.0, 0.25, 0.5$ ) and various shaker force amplitude ( $F_{avg}=120\text{N}, 260\text{N}, 400\text{N}$ ), and at lubricant supply conditions  $P_{in-1}=0.69$  barg and  $P_{in-2}=2.76$  barg.

---

<sup>6</sup> The single-frequency dynamic load tests requires ~10 s to save test data at each frequency, that is, total ~100 s (10 s  $\times$  10) for tests from 10 Hz to 100 Hz. While sine-sweep frequency dynamic load tests with  $\alpha=6.5$  Hz/s requires less than ~20 s to collect test for identical frequency range (10 - 100 Hz).

**Table 6. Sine-sweep frequency dynamic load tests for sealed ends damper A. End seal flow conductance  $\bar{C}_{seal-1}=2.34 \cdot 10^{-4} \text{ mm}^2/(\text{s} \cdot \text{Pa})$ . Excitation frequency range 10 – 100 Hz.**

Sine-sweep frequency dynamic load ( $\alpha=6.5 \text{ Hz}$ )				
Dynamic load amplitude (N)	Static eccentricity, $e_s/c$	Inlet flow rate, $Q_{in}$ (LPM)	Static inlet Pressure, $P_{in}$ (bar(g))	Seal conductance, $C_{ave-s}$ (LPM/bar)
120, 260, 400	$e_s/c_A = 0.0$	0.68	0.69	0.56
120, 260, 400	$e_s/c_A = 0.25$			
120, 260, 400	$e_s/c_A = 0.5$			
260	$e_s/c_A = 0.0$	2.71	2.76	
260	$e_s/c_A = 0.25$			
260	$e_s/c_A = 0.5$			

Figure 32 shows the applied forces in the  $X$  direction ( $F_X$ ) and Figure 33 shows the ensuing BC displacement from two tests of frequency ranges<sup>7</sup> (i) 5 – 55 Hz and (ii) 55 – 105 Hz. Note that the sweep frequency ramp rate  $\alpha=6.5 \text{ Hz/s}$  for motions departing from  $e_s/c_A=0$ . For brevity, only the applied forces and ensuing displacement in the  $X$  direction are shown; typically  $F_X \sim F_Y$  and  $Z_X/c_A \sim Z_Y/c_A$ . The test data correspond to the average amplitude of dynamic load (a)  $F_X=F_Y=F_{avg}=120 \text{ N}$ , (b)  $F_X=F_Y=F_{avg}=260 \text{ N}$ , (c)  $F_X=F_Y=F_{avg}=400 \text{ N}$  with lubricant supply pressure  $P_{in-1}=0.69 \text{ bar}$  and (d)  $F_X=F_Y=F_{avg}=260 \text{ N}$  with  $P_{in-2}=2.76 \text{ bar}$ . Figures 32 and 33 both show the time trace of applied dynamic load and ensuing displacement and its discrete Fourier transform (DFT) amplitude of applied load and BC motion versus frequency.

Recall that the dynamic load amplitude along the  $X$  and  $Y$  direction remains fairly constant  $F_X=F_Y=F_{avg}$ . While the delivered dynamic load tends to decrease for whirl frequency  $\omega=10 \text{ Hz}$  through 30 Hz. In general, for a sine-sweep frequency dynamic load, the shakers receive a periodic voltage signal with increasing frequency and constant amplitude. However, the delivered dynamic load amplitude is not necessarily constant. This is due to a resonance ( $\sim 30\text{Hz}$ ) in the shakers' armature that leads to an inconstant in

<sup>7</sup> The DAQ's limitations prevent recording more than 11 s of data. Thus, the experiments used two frequency ranges to perform tests with the frequency ramp rate  $\alpha=6.5 \text{ Hz/s}$ .

the delivered dynamic load around  $\omega \sim 30$  Hz. Refs.[33,34] detail the explanation of the resonance of the E-shakers.

Notice that at the start and end of the excitation for both frequency ranges (i) 5 – 55 Hz and (ii) 55 – 105 Hz, the DFT amplitude of applied load rapidly changes while maintaining a magnitude that is relatively small compared to those in the 8 – 50 Hz and 60 – 95 Hz ranges. Hence, maintaining a parameter identification range of 5-105 Hz but excluding data in the ranges at the start and end of the excitation (5-7 Hz, 51-59 Hz, 96-105 Hz) give a good correlation between the assumed physical model and the experimental data (see later Figure 34). Note that the frequency range does not excite a resonance of the structure [23].

For dynamic loads from  $F_{avg}=120$  N to 260 N or 400 N, the BC whirls with average orbit amplitude from  $Z/c_A \sim 0.1$  to  $\sim 0.15$  or  $\sim 0.2$  over the identification frequency ranges. Similar to the delivered dynamic load, the BC amplitude motions first decrease with increasing whirl frequency up to  $\omega \sim 30$  Hz and then increase to  $\omega \sim 50$  Hz. As the frequency of the dynamic load increases from 50 Hz to 100 Hz, the BC amplitude motions tend to decrease with increasing whirl frequency.

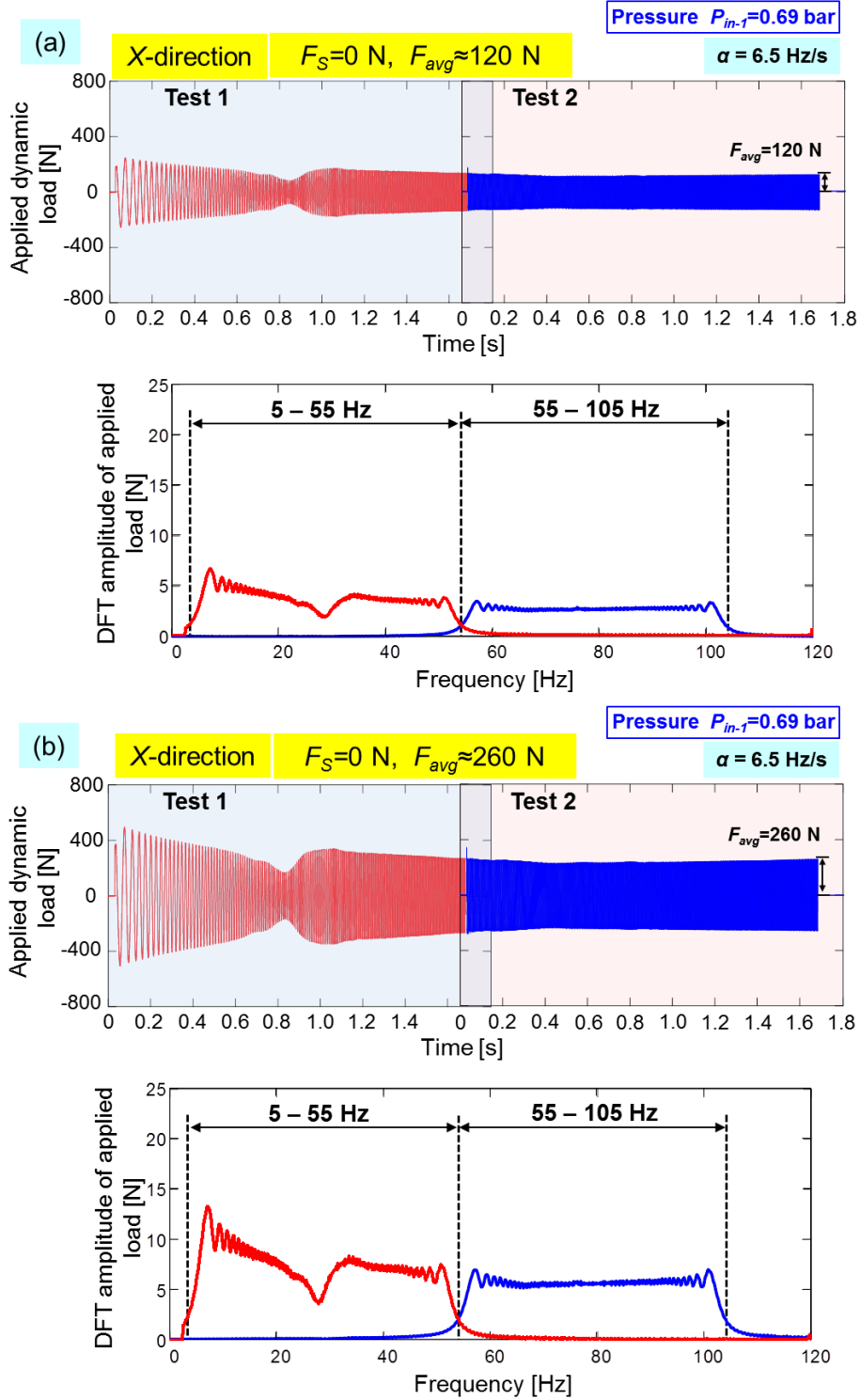


Figure 32. Time trace and DFT of applied dynamic load ( $F_X$ ) for (a)  $F_{avg}=120$  N, (b)  $F_{avg}=260$  N, (c)  $F_{avg}=400$  N with lubricant supply pressure  $P_{in-1}=0.69$  bar and (d)  $F_{avg}=260$  N with  $P_{in-2}=2.76$  bar. Frequency range from (i) 5-55 Hz and (ii) 55-105 Hz.  $\alpha = 6.5$  Hz/s and static journal eccentricity  $e_s=0$ .

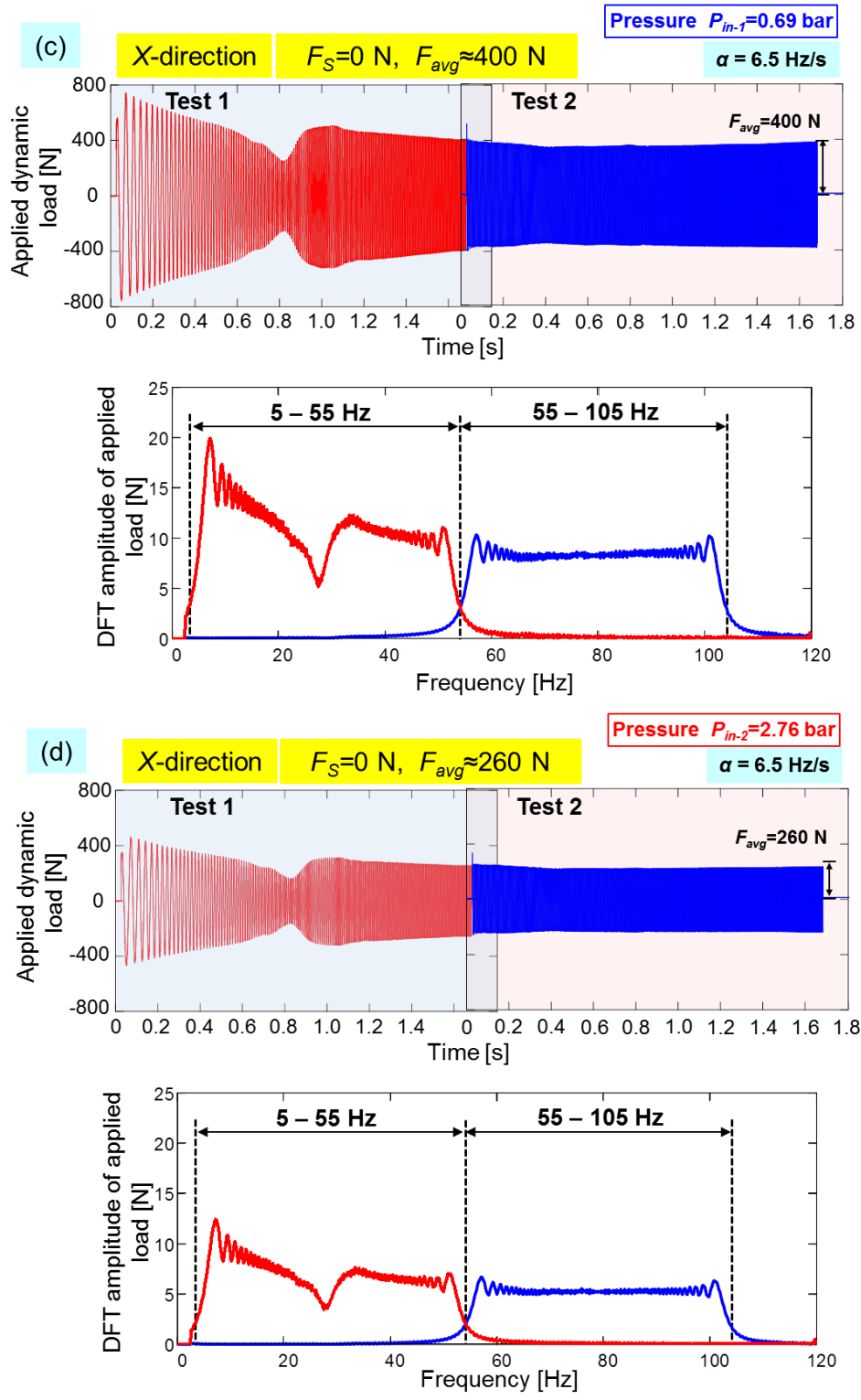


Figure 32. Continued.

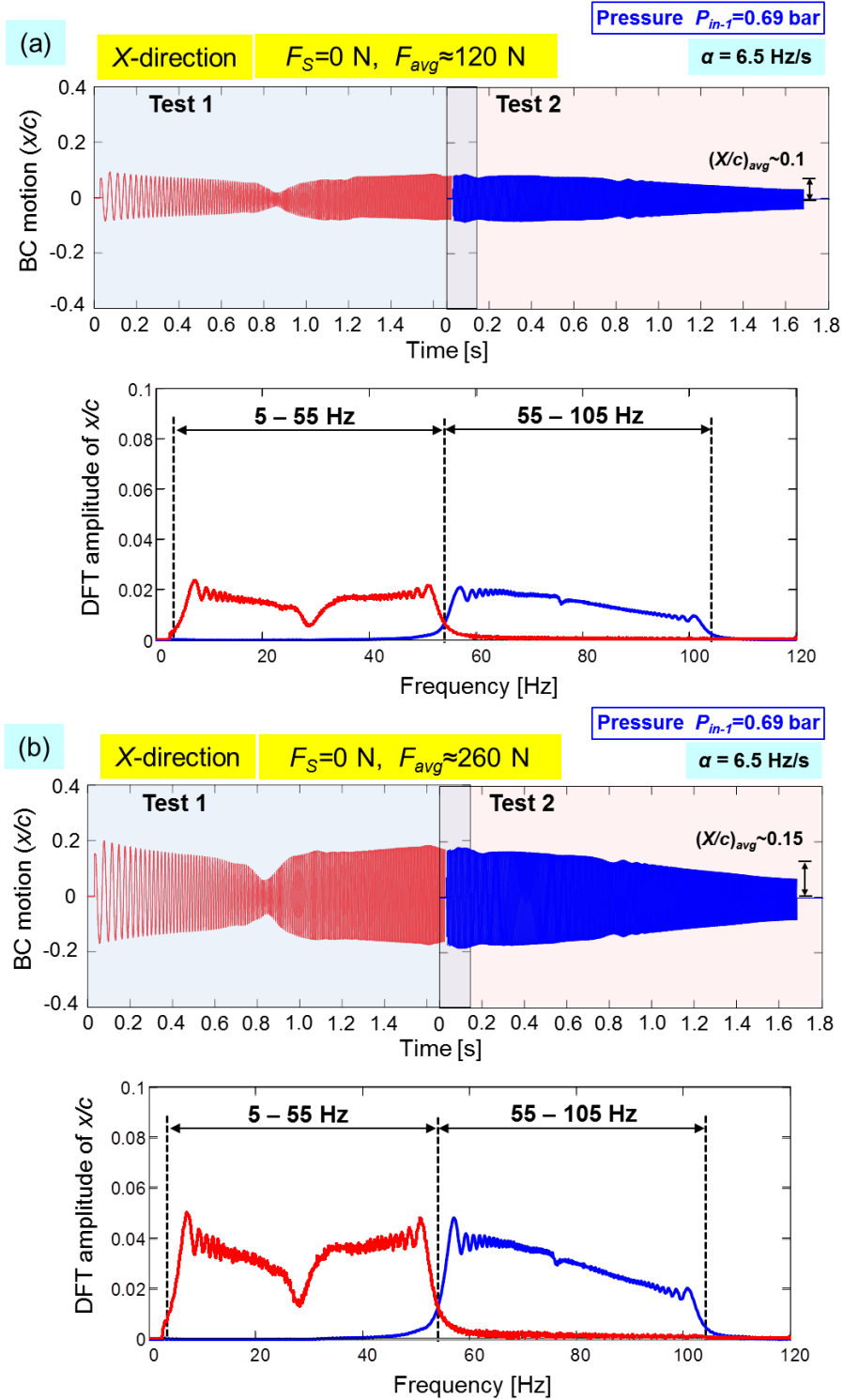


Figure 33. Time trace and DFT of ensuing BC motion ( $x/c$ ) for (a)  $F_{avg}=120$  N, (b)  $F_{avg}=260$  N, (c)  $F_{avg}=400$  N with lubricant supply pressure  $P_{in-1}=0.69$  bar and (d)  $F_{avg}=260$  N with  $P_{in-2}=2.76$  bar. Frequency range from (i) 5-55 Hz and (ii) 55-105 Hz.  $\alpha = 6.5$  Hz/s and static journal eccentricity  $e_s=0$ .

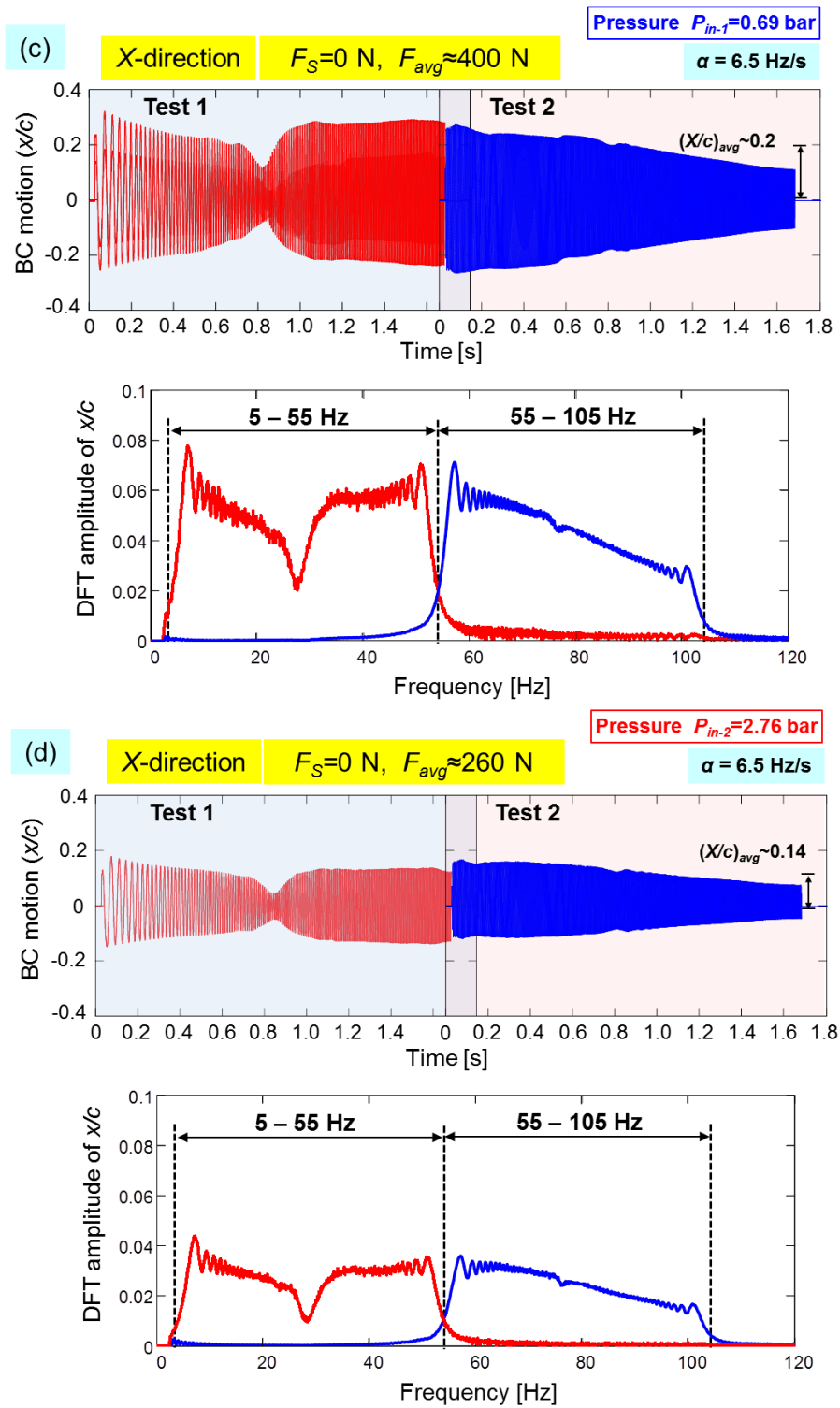


Figure 33. Continued.

## Sine-Sweep Frequency Dynamic Load Experiment Results

Figure 34 presents the real and the imaginary parts of the direct and cross-coupled dynamic impedances ( $H_{XX}$ ,  $H_{YY}$ ,  $H_{XY}$ ,  $H_{YX}$ ) obtained from sine-sweep dynamic load tests of the sealed ends SFD with an average amplitude of dynamic load  $F_{avg}=260$  N and operating with lubricant supply pressure  $P_{in-1}=0.69$  bar. Note that the frequency range for the respective physical model curve fits spans from  $f_{start}=5$  Hz to  $f_{end}=95$  Hz. The majority of the physical model fits show a high correlation factor ( $R^2 > 0.9$ ) for the selected frequency range ( $f_{start}, f_{end}$ ).

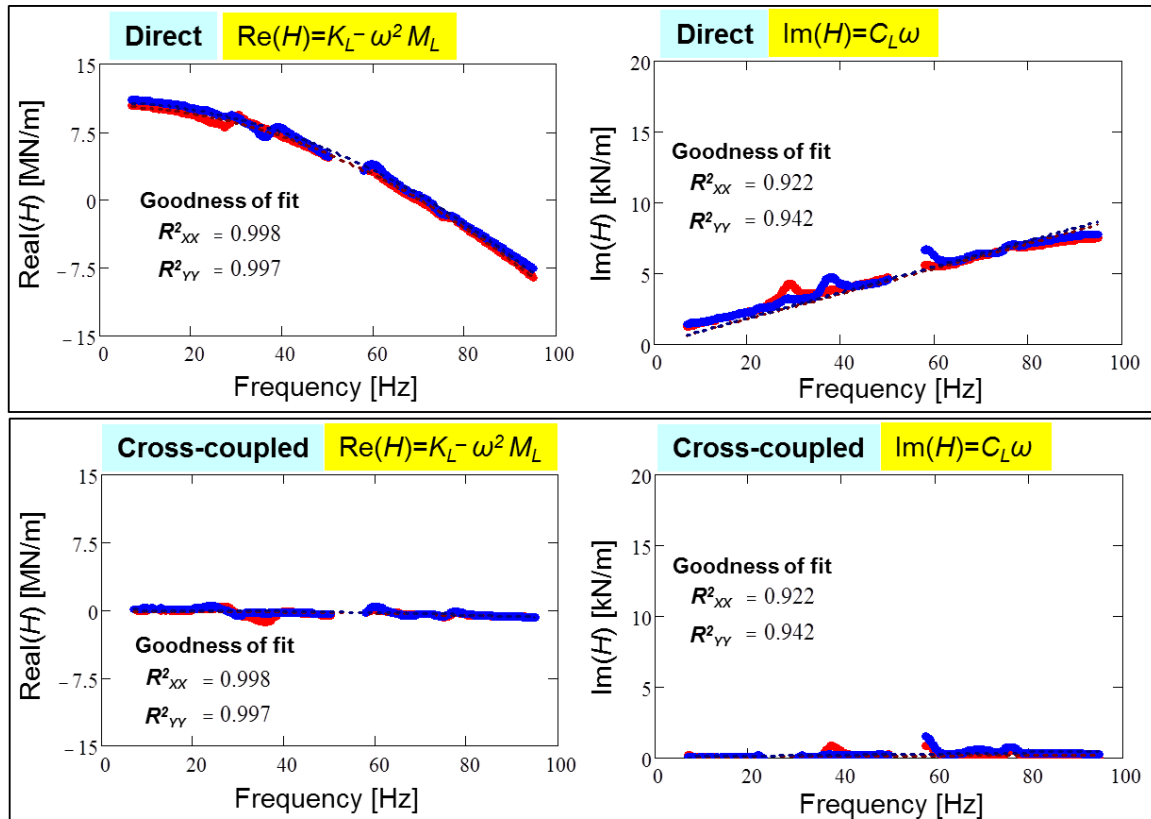


Figure 34. Real and imaginary parts of direct complex stiffness ( $H_{XX}$ ,  $H_{YY}$ ,  $H_{XY}$ ,  $H_{YX}$ ) versus excitation frequency and corresponding physical model (dash lines).  $\alpha = 6.5$  Hz/s. Sealed ends SFD with  $F_{avg}=260$  N with lubricant supply pressure  $P_{in-1}=0.69$  bar. End seal flow conductance  $C_{ave-S1} = 0.56$  LPM/bar.

Figures 35 and 36 present a comparison of the experimentally identified direct SFD damping and added mass versus static eccentricity ( $e_s/c_A$ ) identified over a frequency range  $f=10-100$  Hz from both sine-sweep frequency dynamic loads and single-frequency dynamic load excitations of the sealed ends SFD operating with oil supply pressure  $P_{in-1}=0.69$  bar. Do notice that the SFD cross-coupled coefficient magnitudes are more than one order of magnitude smaller than the direct coefficients, hence, the cross-coupled SFD force coefficients are omitted here for brevity. In general, the identified  $C_{SFD}$ ,  $M_{SFD}$  coefficients versus orbit amplitude (Figure 35) and static eccentricity (Figure 36) obtained from sine-sweep frequency dynamic load tests and single frequency tests agree with each other. The SFD direct added mass coefficients ( $M_{XX}$ ,  $M_{YY}$ ) obtained from sine-sweep frequency dynamic load tests show a  $\sim 15\%$  larger magnitude; however, the values are within the uncertainty ( $U_M \sim 17.4\%$ ) range of those from circular orbit tests.

Figure 37 presents the experimental SFD direct damping ( $C_{XX}$ ,  $C_{YY}$ )<sub>SFD</sub> and added mass ( $M_{XX}$ ,  $M_{YY}$ )<sub>SFD</sub> coefficients for the sealed ends SFD with supply pressure  $P_{in-1} \sim 0.69$  barg ( $Q_{in-1} = 0.68$  LPM) versus supply pressure  $P_{in-2} \sim 2.76$  barg ( $Q_{in-2} = 2.68$  LPM). Recall that the end seal flow conductance is  $C_{ave-S1} = 0.56$  LPM/bar. The test data correspond to circular whirl motions with orbit amplitude  $r/c_A \sim 0.15$  and departing from increasing static eccentricity  $e_s/c_A = 0.0-0.5$ . The frequency range of the sine-sweep dynamic load excitation is  $f=10-100$  Hz and the ramp rate  $\alpha=6.5$  Hz/s. In both cases, the SFD damping coefficients increase with an increase in static eccentricity ( $e_s$ ). A larger supply pressure  $P_{in-2}$ , however, provides constantly  $\sim 25\%$  larger damping coefficients than those provided by a damper with smaller supply pressure  $P_{in-1}$ . On the other hand, the inertia force coefficients for both  $P_{in-1}$  and  $P_{in-2}$  overlap onto each other. Recall that similar trends were observed for SFD force coefficients estimated from single-frequency circular orbit motions (see Figure 15).

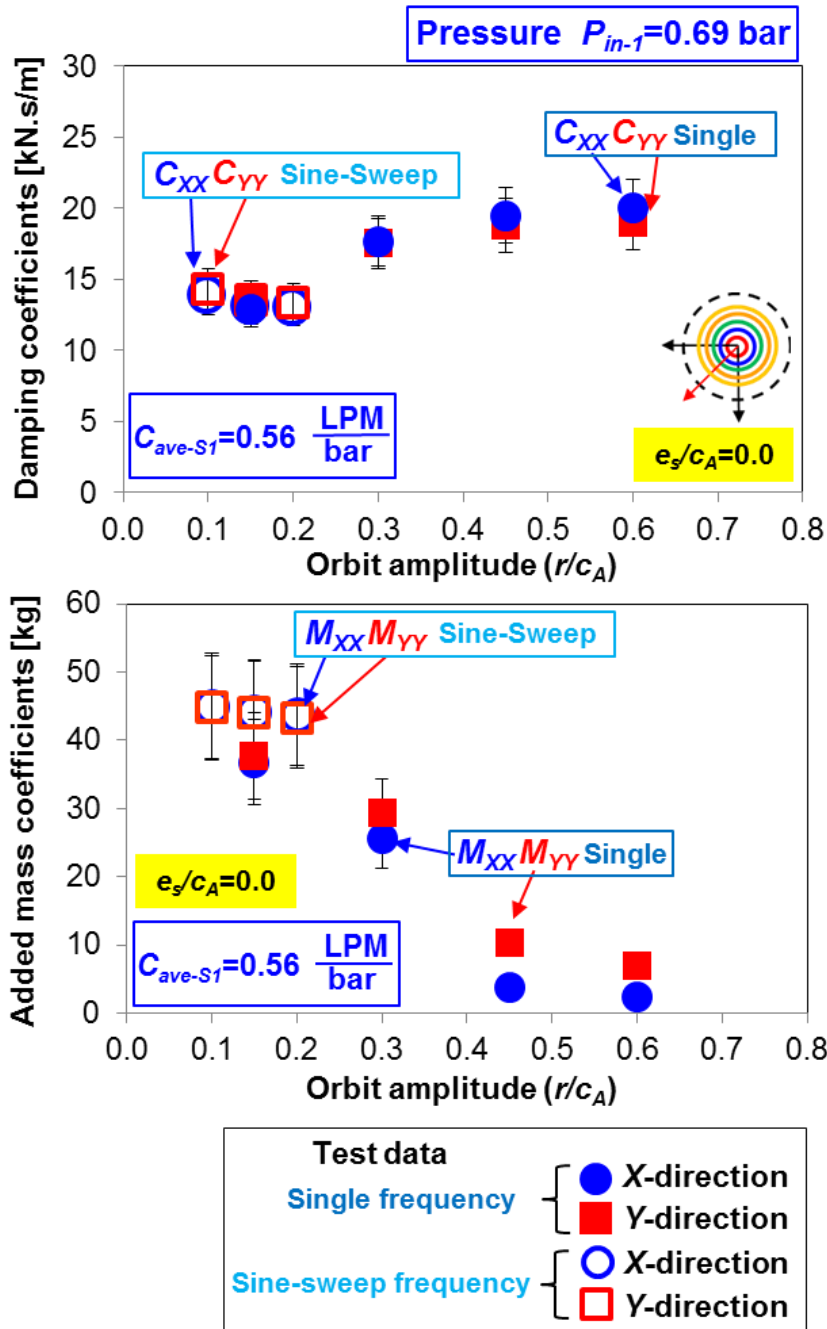


Figure 35. Sealed ends SFD direct damping ( $C$ )<sub>SFD</sub> and added mass ( $M$ )<sub>SFD</sub> force coefficients versus whirl orbit amplitude ( $r/c_A$ ) for motions at the centered condition ( $e_s/c_A=0.0$ ) and obtained from sine-sweep frequency dynamic load tests ( $\alpha = 6.5$  Hz/s) and single-frequency circular orbit tests. End seal flow conductance  $C_{ave-S1}=0.56$  LPM/bar. Identification frequency range 10–100 Hz.

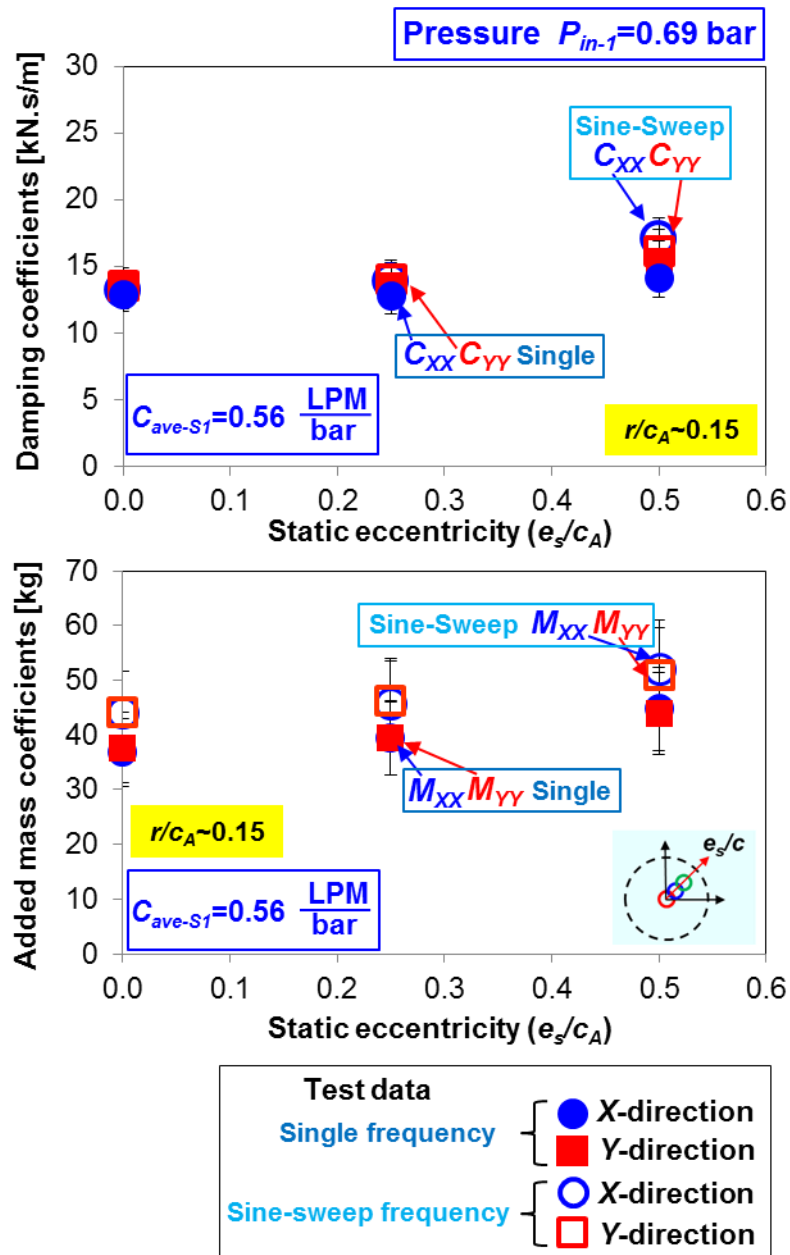


Figure 36. Sealed ends SFD direct damping ( $C_{SFD}$ ) and added mass ( $M_{SFD}$ ) force coefficients versus static eccentricity ( $e_s/c_A$ ) for motions with whirl orbit amplitude ( $r/c_A = 0.15$ ) and obtained from sine-sweep frequency dynamic load tests ( $\alpha = 6.5$  Hz/s) and single-frequency circular orbit tests. End seal flow conductance  $C_{ave-S1} = 0.56$  LPM/bar. Identification frequency range 10–100 Hz.

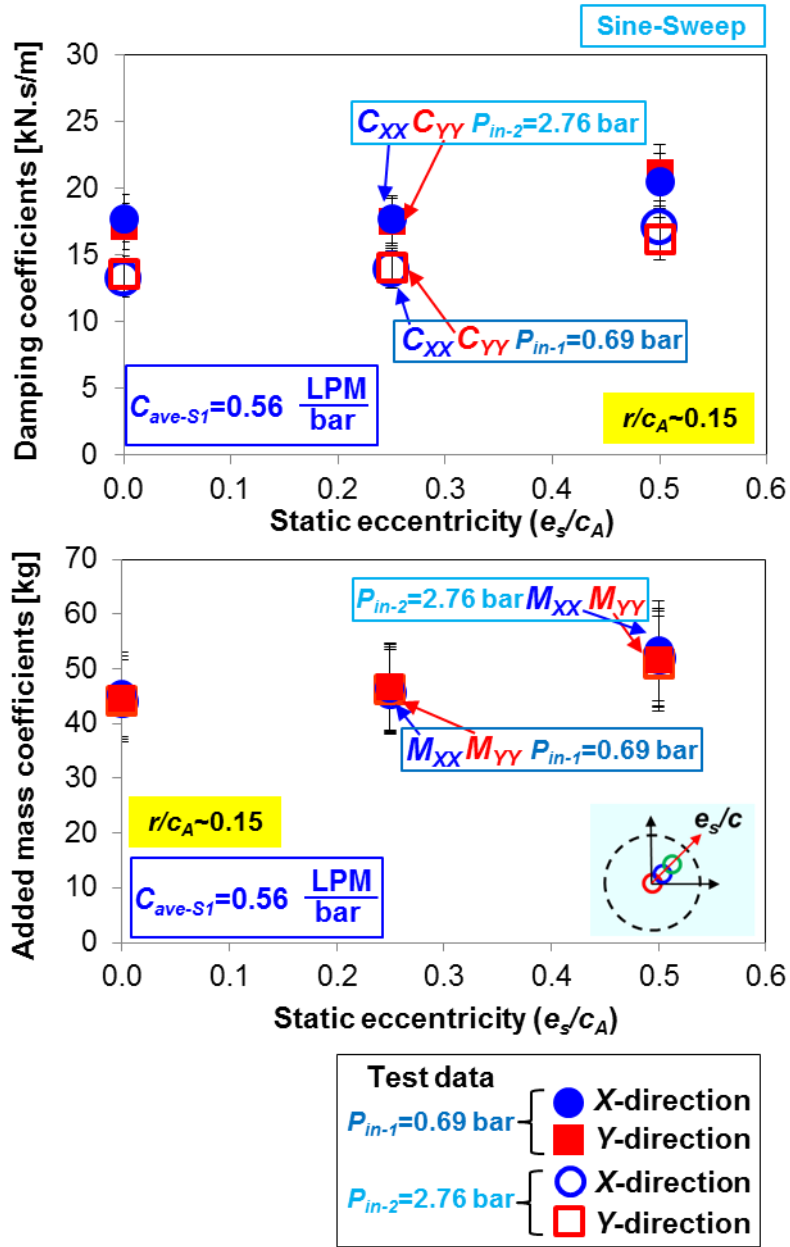


Figure 37. **Effect of lubricant supply pressure:** sealed ends SFD direct damping ( $C$ )<sub>SFD</sub> and added mass ( $M$ )<sub>SFD</sub> force coefficients versus static eccentricity ( $e_s/c_A$ ) at whirl orbit amplitude ( $r/c_A=0.15$ ). End seal flow conductance  $C_{ave-S1}=0.56$  LPM/bar. Identification frequency range 10–100 Hz.

## **Conclusions: Sine-Sweep Frequency Dynamic Loads**

This section presented SFD force coefficients of a sealed ends SFD in response to transient events by performing tests with a sine-sweep frequency dynamic load to simulate an engine startup event. Further comparisons are shown between the sine-sweep frequency dynamic load tests and single frequency dynamic loads test for sealed ends SFDs.

The estimated direct SFD damping and inertia force coefficients obtained both from sine-sweep and single frequency dynamic load tests overlap onto each other within their respective uncertainty ranges. This is because of the slow angular acceleration rate ( $\alpha=6.5$  Hz/s) which allows the mechanical system to attain a quasi-steady state response to the sine-sweep frequency dynamic load, which ultimately enables the accurately estimation of system complex stiffnesses. This finding is also described in Ref. [23], but for tests with open ends SFD. The sine-sweep frequency dynamic load tests evaluate quickly the SFD force coefficients while sweeping from a low to a high whirl frequency while the single frequency load tests require more time to excite a range of frequencies. The experimental results presented provide credence to the abilities of a SFD to control rotor-bearing system response amplitude during transient events such as engine startup sequences.

## Further measurement: Response Due to Single Impact Load<sup>8</sup>

Single impact load tests are performed to quantify the effect of a shock on the elastically supported SFD. The transient response is taken from either centered or off-centered conditions for both open and sealed ends configurations.

First, to perform an impact load test, one side of a steel rod stinger is detached from the BC thus the stingers are not affixed rigidly to the BC, but facing a pair of load cells located at the center of mass of the BC as shown in Figure 38. A load cell aligned with a stinger records the dynamic force ( $F_{X(t)}$  or  $F_{Y(t)}$ ) from the shakers.

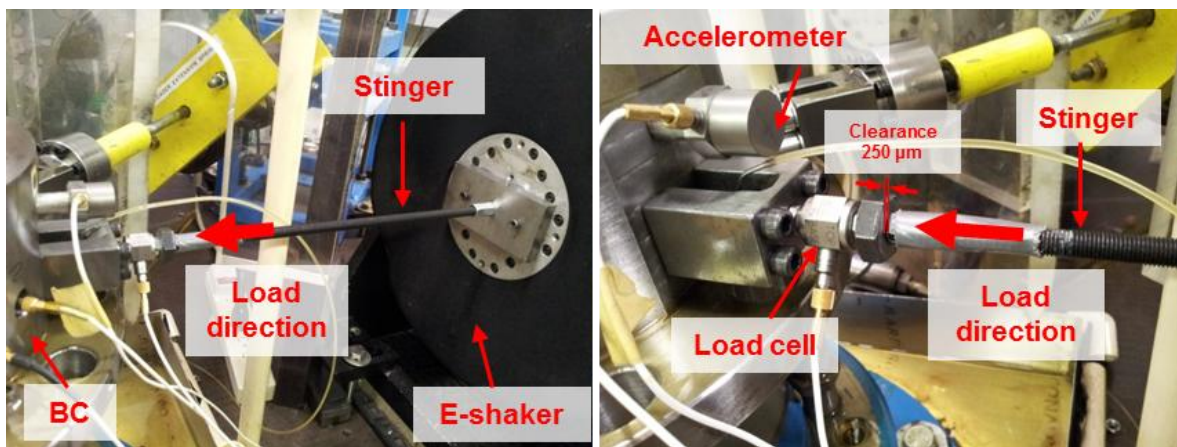


Figure 38. Photo of stinger connection to a shaker and instrumentation set up

Figure 39 displays a schematic view of the BC at a statically off-centered condition. Note that with an increasing static eccentricity  $e_s$ , the damper clearance at  $\Theta=225^\circ$  decreases; this is the location of the minimum clearance. One end of the stinger is not fastened to the load cell mounted on the BC and the free end stinger travels 0.254 mm (10 mil) before imposing dynamic load on the BC.

Table 7 summarizes the operating conditions for single impact load tests performed on the open and sealed ends SFD for motions departing from the journal center. Figure 40 depicts isometric views of the bearing cartridge (BC) and journals for the configurations detailed in Table 7. Again, note that the open and sealed ends dampers' lubricant inlet

<sup>8</sup> Portions of this section reproduce ad-verbatim information described in Ref. [28].



**Table 7. Test conditions for single impact loads.**

Impact load								
Damper Config.	Radial clearance, $c$ (mm)	End condition	Duration of impact, $t_{IMP}$ (ms)	Peak impact load, $F_{MAX}/LD$ (bar)	Static eccentricity, $e_s/c$	Inlet flow rate, $Q_{in}$ (LPM)	Static inlet Pressure, $P_{in}$ (bar(g))	Seal conductance, $C_{ave-S}$ (LPM/bar)
A	0.254	Sealed	1.3	1.6, 3.1, 4.7, 6.2	$e_s/c_A = 0.0$	0.68	0.69	0.56
				1.6, 3.1, 4.7, 6.2	$e_s/c_A = 0.25$			
				1.6, 3.1, 4.7, 6.2	$e_s/c_A = 0.5$			
		Open		1.6, 3.1, 4.7, 6.2	$e_s/c_A = 0.0$	5.03	0.35	-
				1.6, 3.1, 4.7, 6.2	$e_s/c_A = 0.25$			
				1.6, 3.1, 4.7, 6.2	$e_s/c_A = 0.5$			
B	0.267	Open [31]		1.5, 2.4, 3.1, 4.7, 6.2, 7.8	$e_s/c_C = 0.0$	5.21	0.34	-

\*Number of averaged impacts' sets: 15

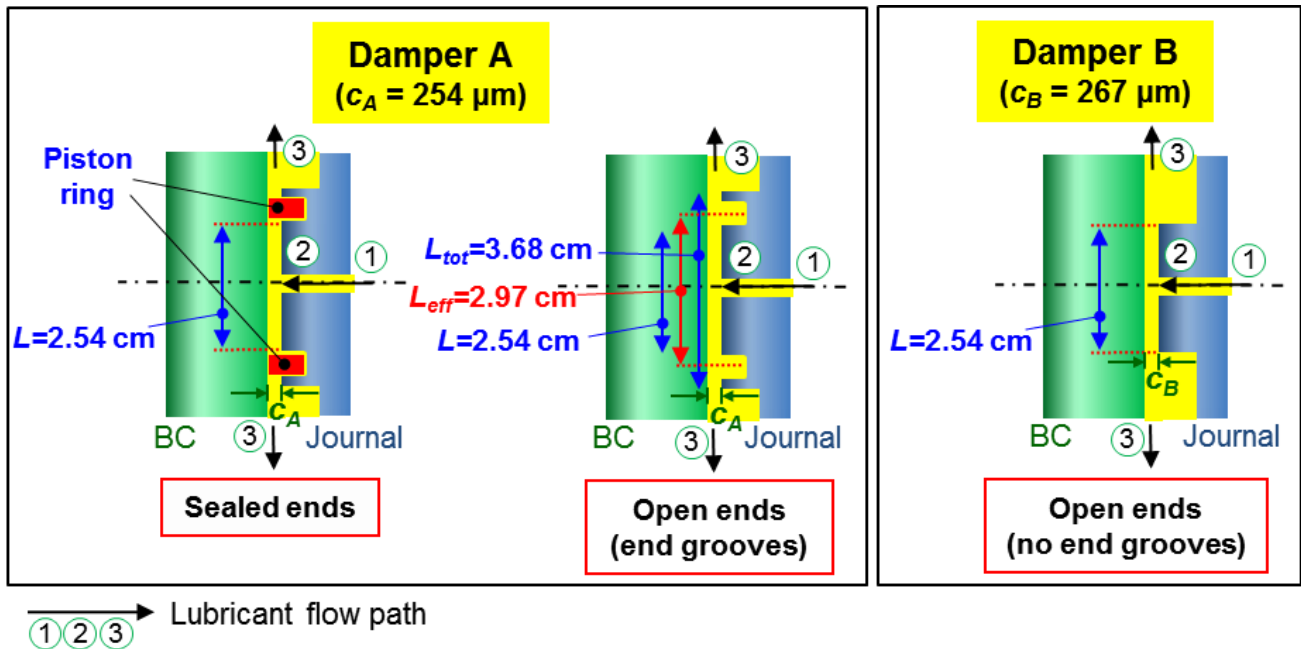


**Figure 40. Cross-section views showing two test squeeze film damper configurations. Test damper A: (a) sealed ends and (b) open ends, end grooves for piston rings. Test damper B [28]: (c) open ends, no end grooves.**

## Single Impact Load Experiment Results

Figure 41 depicts the trace of an impact load delivered to the BC along the  $X$  direction and the ensuing BC displacement ( $Z_X$ ) for tests conducted with both open and sealed ends SFDs, respectively. The test data correspond to an increasing impact peak amplitude  $F_{MAX}/(LD)=1.6 - 6.2$  bar. The impact load, resembling a half-sine wave, lasts  $\sim \Delta t_{IMP}= 1.3$  ms. The response of the BC is characterized as oscillatory, with an exponentially decaying amplitude. For brevity, only the results for  $X$  direction are shown (typically, the BC motions for both  $X$  and  $Y$  directions show the similar results). Expectedly, the transient response of the BC for the sealed ends SFD shows a smaller maximum BC amplitude and decays faster than that of an open ends SFD.

Figure 42 depicts the maximum BC displacement  $\bar{Z}_{MAX}/c = [\bar{Z}_{MAX}^{dyn} + Z_s]/c$  versus the peak amplitude of the impact load ( $\bar{F}_{MAX} / LD$ ) applied along the  $X$  or  $Y$  directions for motions initiating from static eccentricity  $e_s/c_A=0.0, 0.25,$  and  $0.5$ . Let

$$\frac{\bar{Z}_{MAX}^{dyn}}{c} = \frac{1}{c} \left\{ \frac{1}{n} \sum_{i=1}^n [Z_{MAX}^{dyn}]_i \right\}, \quad \frac{\bar{F}_{MAX}}{LD} = \frac{1}{LD} \left\{ \frac{1}{n} \sum_{i=1}^n [F_{MAX}]_i \right\} \quad (18)$$

Each symbol in the graphs represents the average of transient responses collected from  $n=15$  separate impacts.

The dashed lines show a linear regression fit, which for most conditions, evidences a proportional relationship between the maximum BC displacement ( $\bar{Z}_{MAX}^{dyn}$ ) and the peak

impact load, that is,  $\frac{\bar{Z}_{MAX}^{dyn}/c}{\bar{F}_{MAX}/(LD)} \rightarrow \beta$  is nearly constant. A large load forces the BC

towards a large (dynamic) amplitude.  $Z_{MAX}/F_{MAX}$  appears to be smaller with sealed ends damper compared to open ends. Again, this indicates that with same amount of applied unit load, the peak displacement is smaller for sealed ends damper. Most notably, for both open and sealed ends dampers, increasing the static eccentricity ( $e_s$ ) of the SFD causes no significant difference in the slope ( $\beta$ ).

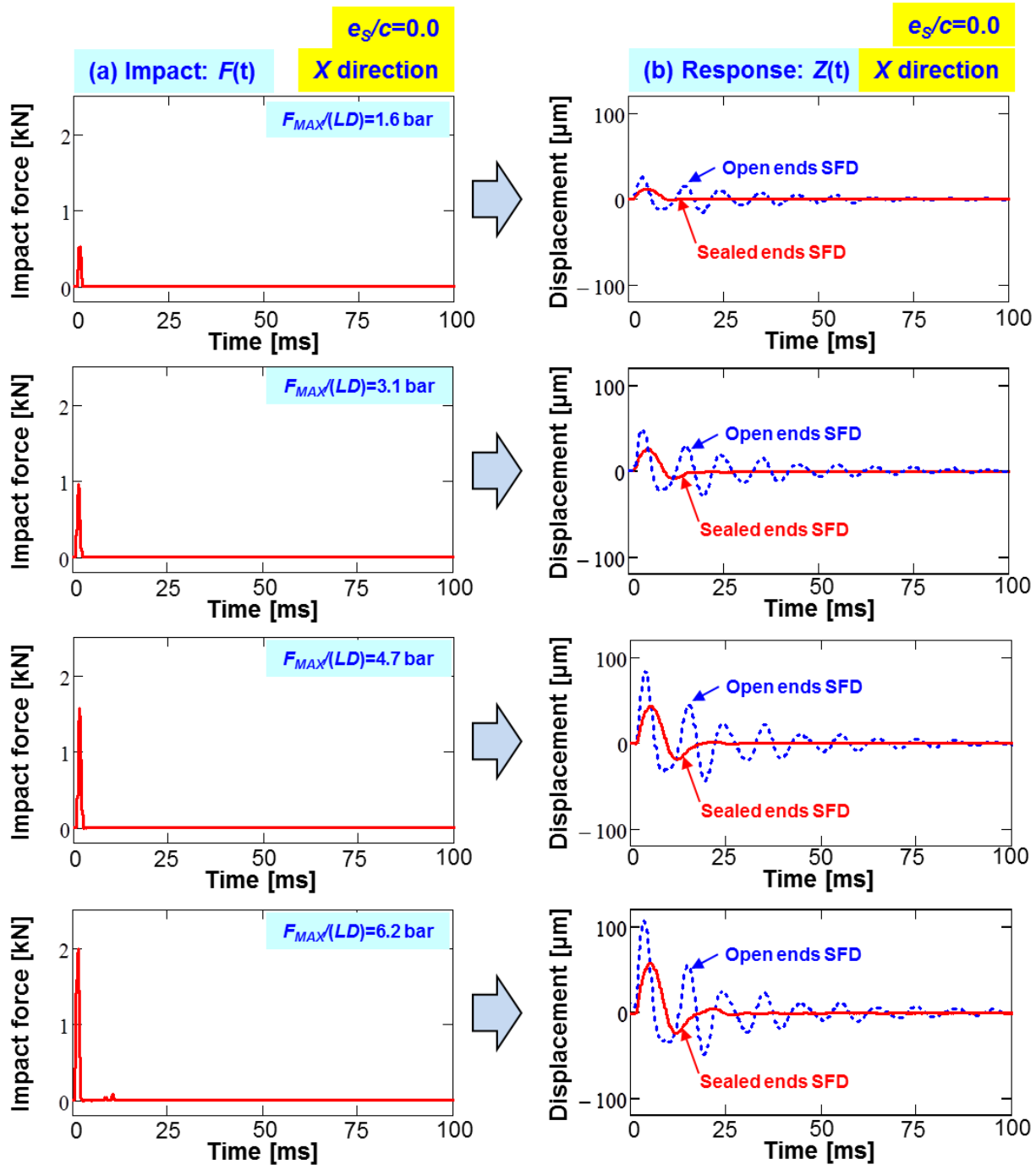


Figure 41. Impact load along X direction and BC dynamic displacement  $Z_x$  versus time. Test at centered condition ( $e_s=0.0c$ ). Single impact load  $F_{MAX-x}/(LD)=1.6 - 6.2$  bar. Open ends and sealed ends SFD with clearance  $c_A=0.254$  mm.

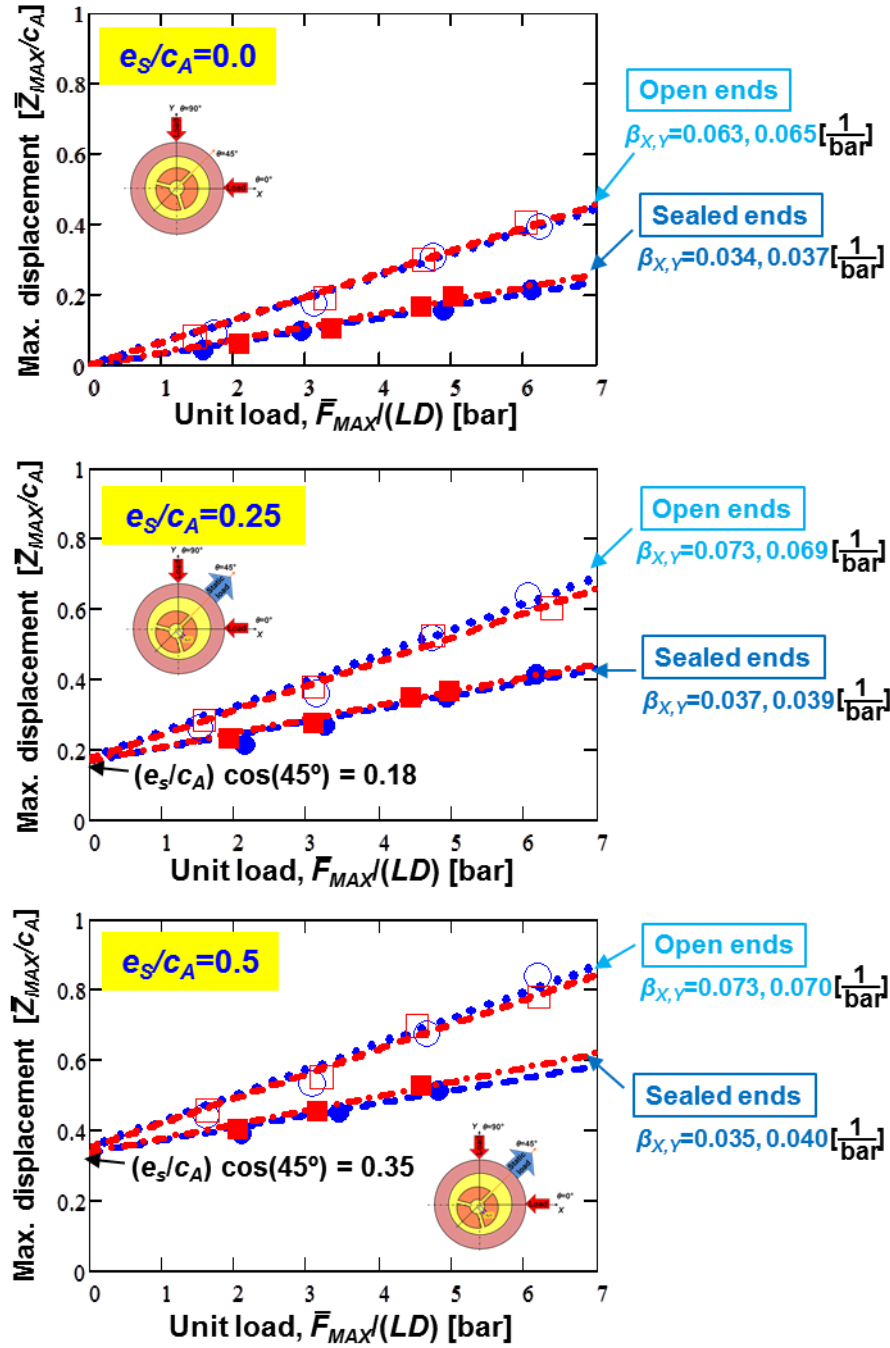


Figure 42. Maximum displacement  $\bar{Z}_{MAX}/c_A$  vs. peak amplitude of applied single impact load  $\bar{F}_{MAX}/(LD)$  for motions initiating from static eccentricity  $e_s/c=0.0, 0.25,$  and  $0.5$ . Open ends and sealed ends SFD with clearance  $c_A=0.254$  mm.  $\beta[1/\text{bar}] =$  slope of line fit to data.

Figure 43 shows  $\beta$ , the peak BC amplitude  $((\bar{Z}_{MAX}^{dyn})/c)_{X,Y}$  over unit load  $(\bar{F}_{MAX} / LD)$  versus static eccentricity  $(e_s/c_A)$ . The data correspond to results from a single impact load for both open and sealed ends SFDs for motions initiating from static eccentricity  $e_s/c_A=0.0, 0.25,$  and  $0.5$ .  $\beta$  appears to be constant with increasing static eccentricity albeit the open ends damper shows  $\sim$ two times larger  $\beta$  than those of sealed ends. Ref.[28] details the estimation of variability  $V\sim\pm 14\%$ .

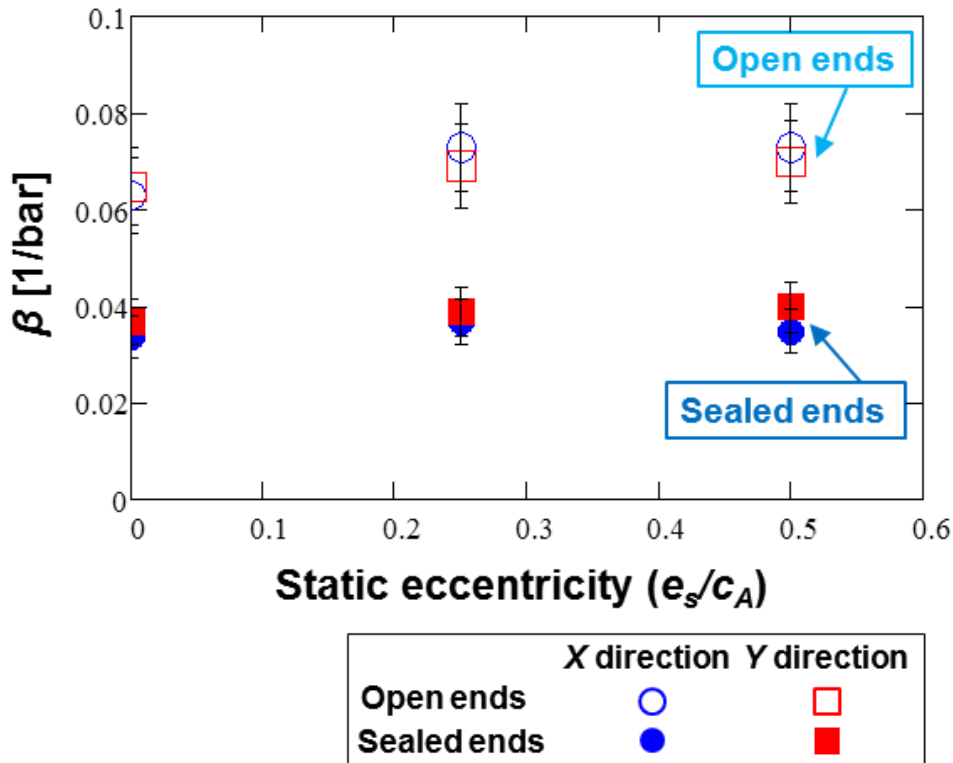


Figure 43. Peak displacement  $\bar{Z}_{MAX}/c_A$  over peak amplitude of unit load  $\bar{F}_{MAX}/(LD)$  vs. static eccentricity  $e_s/c_A=0.0, 0.25,$  and  $0.5$ . Open ends and sealed ends SFD with clearance  $c_A=0.254$  mm.

As shown in Figure 41, the BC response to a delivered impact load decays exponentially, which is typical of a viscous under-damped system. From this BC response, a well-known equation for the logarithmic decrement ( $\delta$ ) identifies the system log dec ( $\delta$ ) or subsequently the system damping ratio  $\xi$ . Deriving log dec  $\delta$  from the ratio of two peak displacement amplitudes separated by  $N$  periods of motion [35] follows

$$\delta = \frac{1}{N} \ln \left( \frac{Z_k}{Z_{k+N}} \right) = \frac{2\pi\xi}{\sqrt{1-\xi^2}} = \xi\omega_n\tau_d \quad (19)$$

Eq. (19) is based on the transient free-response of an underdamped ( $\xi < 1$ ) one degree of freedom mechanical system, where  $\xi = \frac{C}{2\sqrt{K_S M}}$  is the damping ratio and  $\omega_n = \sqrt{\frac{K_S}{M}}$  is the system natural frequency. Above,  $M = M_{BC} + M_{SFD}$ , where  $M_{BC} = 15.15$  kg and  $M_{SFD}$  is the SFD added mass, and  $K_S = 12.0$  MN/m is the support structural stiffness.

Figure 44 shows the displacement transient response overlaid with the damping envelope curve ( $e^{-\xi\omega_n t}$ ). The data corresponds to unidirectional impact loads with  $F_{MAX}/(LD) = 1.6$  bar on open ends and sealed ends SFD for motions initiating from the centered condition ( $e_s = 0$ ). For a better comparison of all the presented test conditions, the BC displacements are normalized with respect to the BC maximum peak amplitude such that,  $Z/Z_{MAX}$ . Hence, the maximum dimensionless displacement is equal to one. The BC transient response decays faster for the larger amplitude applied impact load and motions starting from a higher static eccentricity. A curve fit on the six peaks for open ends and three peaks for sealed ends in the recorded transient response estimates the logarithmic decrement ( $\delta$ ). The majority of the line fits ( $e^{-\xi\omega_n t}$ ) show a high correlation factor ( $R^2 > 0.9$ ) indicating the physical model is adequate to represent the transient response of the test SFD subject to a single impact load.

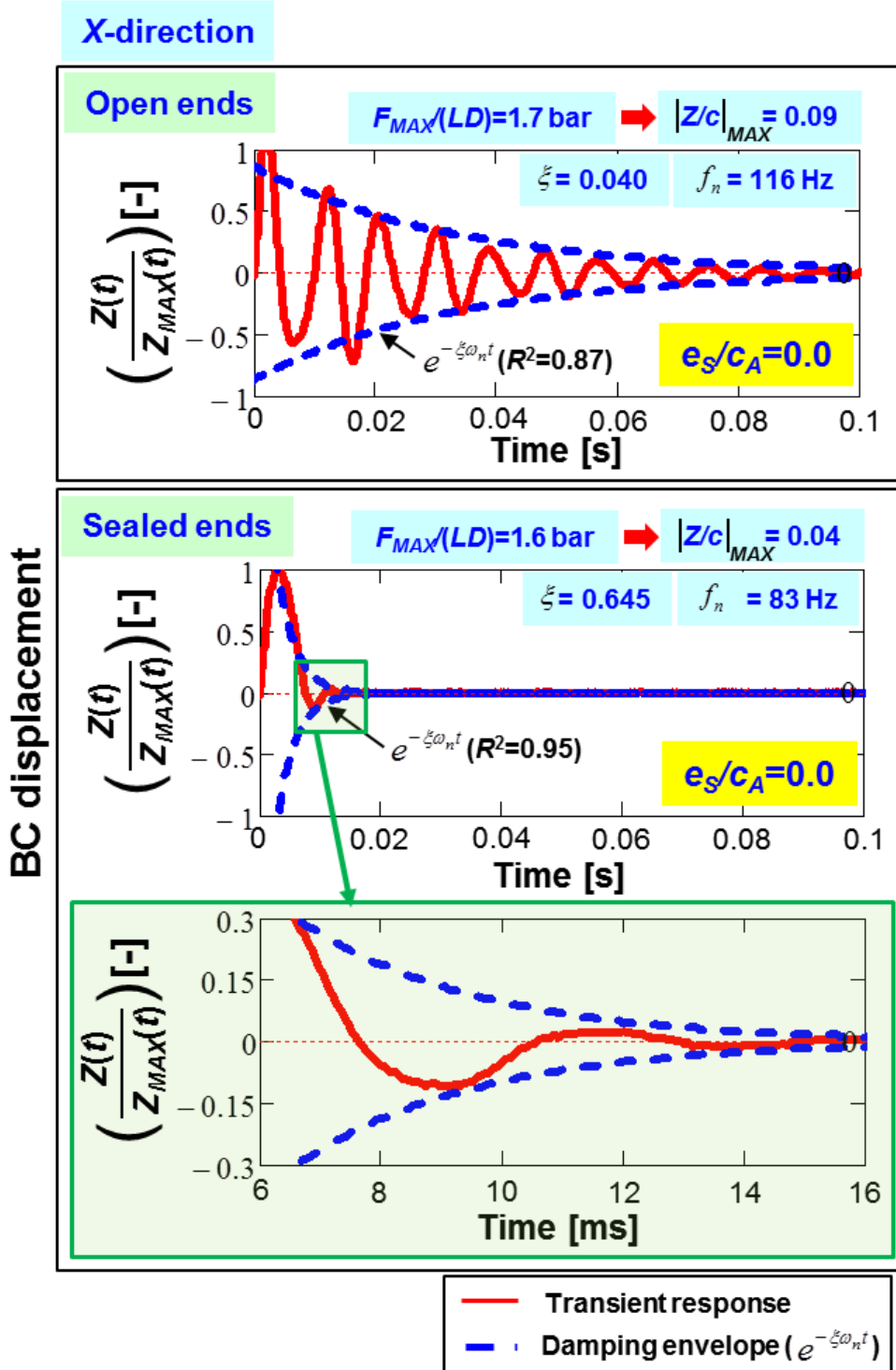


Figure 44. Dimensionless BC displacement  $Z/Z_{MAX-X}$  and damping envelope ( $e^{-\xi\omega_n t}$ ) versus time ( $t$ ). Measurements for  $F_{MAX-X}(LD)=1.6 \text{ bar}$  for motions from  $e_S/c_A=0$ . Open ends and sealed ends SFD with clearance  $c_A=0.254 \text{ mm}$ .

Figure 45 shows the estimated system damping ratio ( $\zeta$ ) obtained for the sealed ends and the open ends SFDs versus maximum displacement ( $Z_{MAX}/c_A$ ). The test data correspond to a single impact on the SFD and motion departing from static eccentricity  $e_s=0.0c_A$ ,  $0.25c_A$ , and  $0.5c_A$ . Recall that  $Z_{MAX}$  includes the static displacement  $Z_S$ , see Eq. (17), depicted with dashed (vertical) lines on the Figure.

Both sealed ends and open ends dampers show an increase of damping ratio ( $\zeta$ ) with increasing BC amplitude ( $\bar{Z}_{MAX}^{dyn}$ ) and the static eccentricity ( $e_s$ ) albeit ( $\zeta$ ) for sealed ends dampers increases sharply with  $\bar{Z}_{MAX}^{dyn}$  than that of open ends SFD.

The sealed ends SFD provides ten to fifteen more damping ratio than the open ends configuration, i.e., the end seals enable the BC response to decay faster when subjected to impact load.

The magnitude of  $\beta(= \bar{Z}_{MAX}^{dyn} / \bar{F}_{MAX})$  only decreases ~46% with the sealed end damper configuration (see Fig. 43). This is not surprising because the initial peak  $\bar{Z}_{MAX}^{dyn}$  is largely

influenced by the initial kinetic energy  $\dot{Z}_0 = \frac{\int_0 F dt}{M}$  as opposed to the damping ratio  $\zeta$ .

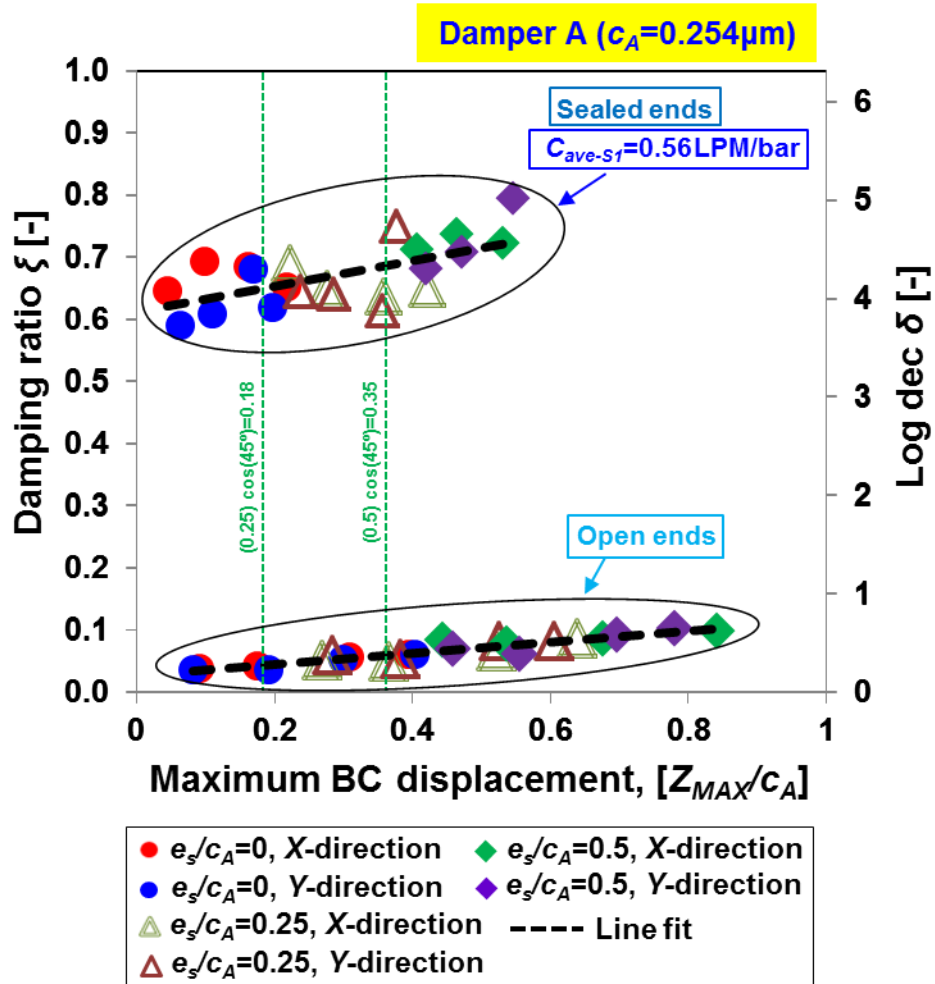


Figure 45. System damping ratio ( $\xi$ ) and logarithmic decrement ( $\delta$ ) versus peak BC ( $Z_{MAX}/c$ ) displacement. Data for one impact load and motions departing from various static eccentricity. Open and sealed ends SFDs with  $c_A=0.254 \text{ mm}$  ( $L/D=0.2$ ).

Ref. [28] also reports measurements of system transient response due to a single impact load of increasing magnitude and motions starting at the centered position ( $e=0$ ). In Ref. [28], however, the open ends test damper has a radial clearance of  $c_B=267 \mu\text{m}$ . Table 8 lists the distinct operating conditions for the two test SFDs with identical film land length  $L=25.4 \text{ mm}$  and diameter, as well as lubricant inlet and temperature. However, the damper A has end grooves and chamfered lips that add up to total wetted length  $L_{tot}=36.83\text{mm}$  (see Fig. 40) where the dynamic pressure generation at the end grooves are significant (see Fig. 20).

**Table 8. Open ends SFD configurations and operating conditions for two film clearances**

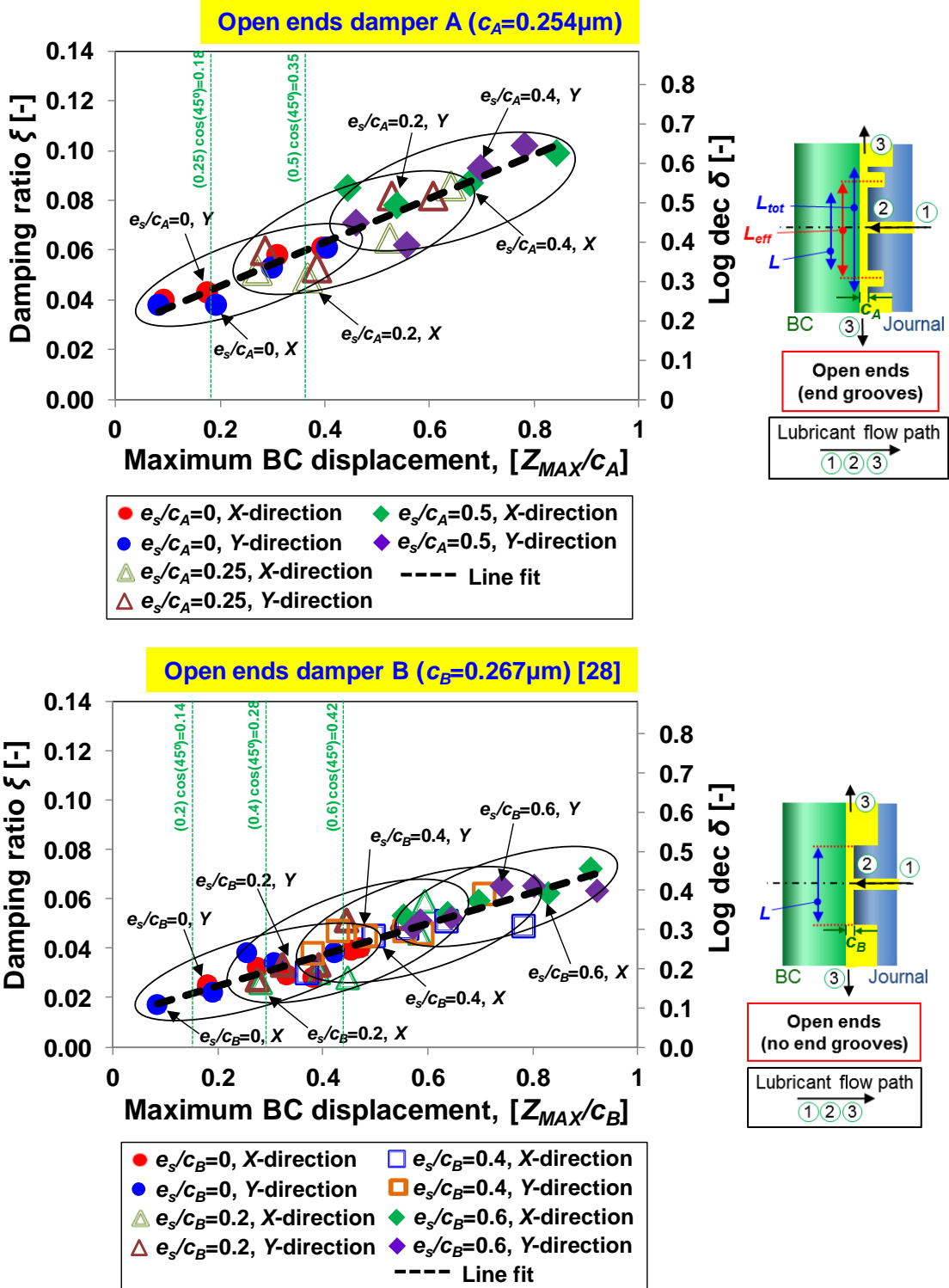
Parameter	Damper A	Damper B [28]
Radial clearance	254 $\mu\text{m}$	267 $\mu\text{m}$
Land length	$L_{eff}=2.97^*$	$L=2.54$
Static inlet pressure, $P_{in}$	0.35 bar(g)	0.34 bar(g)
Inlet flow rate, $Q_{in}$	5.03 LPM	5.21 LPM

\*Denotes the effective film land length ( $L_{eff}$ )

Figure 46 shows comparisons of the damping ratio ( $\zeta$ ) estimated from both damper A and B differing in clearance and land length. The estimated SFD damping ratio for the small film clearance ( $c_A$ ) damper is  $\sim 1.6$  times larger than the damping ratio ( $\zeta$ ) obtained with a larger clearance ( $c_B$ ) damper. That is,  $(\zeta_B/\zeta_A) \sim 1.6$  to  $\sim 1.7$ , which appears to scale with the square of the film clearances, i.e.

$$\frac{\zeta_A}{\zeta_B} = \left(\frac{c_B}{c_A}\right)^2 \left(\frac{L_{eff}}{L_B}\right)^2 = \left(\frac{0.267}{0.213}\right)^2 \left(\frac{2.97}{2.54}\right)^2 = 1.76 \quad (20)$$

As detailed in Ref.[5] the simple formulas use an effective film length  $L_{eff}=1.17 L =29.7 \text{ mm}$  that is larger than the design film land length  $L= 25.4 \text{ mm}$  and shorter than the actual wetted length,  $L_{tot} = 36.8 \text{ mm} > L_{eff} > L$ . The effective film land length ( $L_{eff}$ ) is estimated by curve fitting the recorded pressure profile as a parabolic function of the axial coordinate. Furthermore, Ref. [36] details the comparisons for single frequency dynamic load experimental results with open ends damper A and B.



## Conclusions: Single Impact Load Test

This section presented single impact load tests for both open and sealed ends SFDs. The SFD transient response decays faster with the sealed ends damper, i.e., larger log dec for sealed ends SFD. The damping ratio ( $\zeta$ ) derived from a single impact load shows an increase with the peak displacement  $Z_{MAX} = Z_{MAX}^{dyn} + Z_s$ . Interestingly enough,  $\bar{Z}_{MAX}^{dyn}$  appears linear with respect to the maximum dynamic impact load  $\bar{F}_{MAX}$  for both open and sealed ends dampers.  $\bar{Z}_{MAX}^{dyn} / \bar{F}_{MAX}$  only decreases ~46% with the sealed end damper configuration while the sealed ends SFD provides ten to fifteen times larger damping ratio than the open ends configuration, since  $\bar{Z}_{MAX}^{dyn}$  is largely affected by the initial kinetic energy  $\dot{Z}_0$ .

The damping ratio for a small film clearance ( $c_A = 0.254$  mm) SFD is ~1.6 times larger than the damping ratio ( $\zeta$ ) obtained with the larger clearance damper B ( $c_B = 0.267$   $\mu\text{m}$ ).

The experimental results due to a sudden impulsive load that produces transient displacements extend the prior work in Ref.[28] on the same SFD test rig, but with open ends SFD. These comprehensive experiments serve to characterize a sealed ends SFD experiencing stringent operating conditions such as a hard landing.

## Conclusions and recommendations

The reports consolidates measurements and analyses of force performance obtained with short length SFDs ( $L/D=0.2$ ) for open and sealed ends configurations, respectively. The various dynamic load tests include single frequency and sine-sweep frequency dynamic loads and single impact load. These various dynamic load tests allow estimating experimentally the forced performance of the SFDs under various operating conditions. The major conclusions drawn in this work are:

(i) Measurements of single frequency dynamic load tests for open and sealed ends SFDs

a. Effect of lubricant supply pressure on sealed ends SFD force coefficients:

For sealed ends SFD, upon increasing the lubricant supply pressure by four times ( $P_{in-1} \sim 0.69 \rightarrow P_{in-2} \sim 2.76$  barg), the SFD added mass coefficients show a large increase, whereas the SFD direct damping coefficients do not show a significantly increase.

b. Effect of flow conductance on sealed ends SFD Force coefficients:

At fixed lubricant supply pressure  $P_{in-1} \sim 0.69$  barg, for the sealed ends SFD with smaller flow conductance  $C_{ave-S1}$  ( $0.63 \cdot C_{ave-S2}$ ) the damping coefficients sharply increase with increasing whirl amplitude ( $r/c_A$ ) while sealed damper with larger  $C_{ave-S2}$  provides more or less constant damping with  $r$ .

c. Comparison between open and sealed ends dampers A:

SFD direct damping coefficients are 11-13 times greater for the sealed end damper than those for open ends SFD. For the ends sealed damper SFD, direct added masses are ~two times greater than the BC actual mass ( $M_{BC}=15.2$  kg) and ~11 times greater than the fluid film added masses for the open-ends damper.

d. Comparison between predictions and experimental results

Numerical predictions from computational program [7] agree very well with the experimental damping while under predicting the inertia coefficients.

(ii) Measurements of sine-sweep frequency dynamic load tests for sealed ends SFDs

e. Experiments with a sine-sweep frequency dynamic load confirmed the findings made in the Ref.[23]; namely the SFD force coefficients with a low rate of change

in excitation frequency ( $\alpha$ ) agree with the coefficients obtained from a single-frequency dynamic load over the same test conditions.

(iii) Measurements of single impact load tests for open and sealed ends SFDs

- f. The SFD transient response decays faster with both large amplitude applied impact load ( $F$ ) and when departing from a high static eccentricity ( $e_s$ ).
- g. Similarly, the damping ratio ( $\zeta$ ) derived from a single impact load increases linearly with the peak displacement  $Z_{MAX} = \bar{Z}_{MAX}^{dyn} + Z_s$ .
- h. The sealed ends SFD provides a ten to fifteen larger damping ratio than the open ends configuration.
- i.  $\bar{Z}_{MAX}^{dyn} / \bar{F}_{MAX}$  decreases ~46% with the sealed end damper configuration compared to open ends damper.  $\bar{Z}_{MAX}^{dyn}$  is largely affected by the initial kinetic energy  $\dot{Z}_0$ .
- j. The damping ratio for a small film clearance ( $c_A=0.254$  mm) SFD is ~1.6 times larger than the damping ratio ( $\zeta$ ) obtained with the larger clearance damper B ( $c_B=0.267$   $\mu\text{m}$ ).

This report presents comprehensive dynamic load tests on the open and sealed ends SFDs that allow characterizing the SFD due to single and sine-sweep frequency dynamic loads and to an impact load. The experimentally identified force coefficients for single and sine-sweep frequency dynamic loads allow performing reliability analysis of high performance rotor-bearing system. Furthermore, the test results for impact load on sealed ends SFD provide engineers credence to determine the performance of a SFD during transient events such as in hard landing and takeoff.

## Acknowledgement

The financial support the Turbomachinery Research Consortium (TRC) is gratefully acknowledged. Thanks to Pratt & Whitney for providing the piston ring seals. Special thanks to Sean Den, Scott Tran and Adrian Rangel for reviewing the report.

## References

- [1] San Andrés, L., 2012, *Modern Lubrication Theory*, “Squeeze Film Dampers: Operation, Models and Technical Issues,” Notes 13, Texas A&M University Digital Libraries, <http://oaktrust.library.tamu.edu/handle/1969.1/93197>
- [2] Vance, J., Zeidan, F., Murphy, B., 2010, *Machinery Vibration and Rotordynamics*, “Bearings and Their Effect on Rotordynamics”, Chapter 5, John Wiley & Sons, Inc., New York, pp. 216-238.
- [3] San Andrés, L., Jeung, S.-H., Den, S., Savela, G., and Nagaraj, C., 2016, “Squeeze Film Dampers: An Experimental Appraisal of Their Dynamic Performance,” *Proceedings of the 2016 Asia Turbomachinery & Pump Symposium*, Marina Bay Sands, Singapore.
- [4] Zeidan, F. Y., Vance, J. M., and San Andrés, L., 1996 “Design and Application of Squeeze Film Dampers in Rotating Machinery,” *Proceedings of the 25th Turbomachinery Symposium*, Texas A&M University, Houston, TX, pp. 169–188.
- [5] Jeung, S.-H., San Andrés, L., and Bradley, G., 2016, “Forced Coefficients for a Short Length, Open-Ends Squeeze Film Damper with End Grooves: Experiments and Predictions,” *ASME J Gas Turb Pwr*, **138**(2), p. 032502.
- [6] San Andrés, L., and Jeung, S.-H., 2015, “Response of an Squeeze Film Damper to Large Amplitude Impact Loads,” 2015 STLE Annual Meeting & Exhibition, May 18-21, Dallas, TX, USA.
- [7] San Andrés, L., and Jeung, S.-H., 2016, “Orbit-Model Force Coefficients for Fluid Film Bearings: A Step Beyond Linearization,” *ASME J Gas Turb Pwr*, **138**(2), p. 022502.
- [8] Diaz, S., and San Andrés, L., 2001, "Air Entrainment Versus Lubricant Vaporization in Squeeze Film Dampers: An Experimental Assessment of Their Fundamental Differences," *ASME J Gas Turb Pwr*, **123**(4), pp. 871-877.
- [9] Levesley, M., and Holmes, R., 1996, “The Effect of Oil Supply and Sealing Arrangements on the Performance of Squeeze-Film Dampers: An Experimental Study,” *Proc. Inst. Mech. Eng., Part J: J. Eng. Tribol.*, **210**(4), pp. 221–232.
- [10] Kim, K., and Lee, C., 2005, “Dynamic Characteristics of Sealed Squeeze Film Damper With a Central Feeding Groove,” *ASME J. Tribol.*, **127**(1), pp. 103–111.
- [11] Miyachi, T., Hoshiya, S., Sofue, Y., Matsuki, M., and Torisaki, T., 1979, “Oil Squeeze Film Dampers for Reducing Vibration of Aircraft Gas Turbine Engines,” *ASME Paper No. 79-GT-133*.

- [12] De Santiago, O., and San Andrés, L., 1999, "Imbalance Response and Damping Force Coefficients of a Rotor Supported on End Sealed Integral Squeeze Film Dampers," ASME Paper No. 99-GT-203.
- [13] Defaye, C., Arghir, M., and Bonneau, O., 2006, "Experimental Study of the Radial and Tangential Forces in a Whirling Squeeze Film Damper," *STLE Tribol. Trans.*, **49**(2) pp. 271-278.
- [14] Meng, G., San Andrés, L., and Vance, J., 1991, "Experimental Measurement of the Dynamic Pressure and Force Response of a Partially Sealed Squeeze Film Damper," Proceedings of the 13th Biennial Conference on Mechanical Vibration and Noise, Miami, FL, September 22–25, Rotating Machinery and Vehicle Dynamics, ASME, **35**, pp. 251–256.
- [15] San Andrés, L., and Seshagiri, S., 2013, "Damping and Inertia Coefficients for Two End Sealed Squeeze Film Dampers with a Central Groove: Measurements and Predictions," *ASME J Gas Turb Pwr*, **135**(12), p. 112503.
- [16] San Andrés, L., 2012, "Damping and Inertia Coefficients for Two Open Ends Squeeze Film Dampers With a Central Groove: Measurements and Predictions," *ASME J. Eng. Gas Turbines Power*, **134**, p. 102506.
- [17] Delgado, A., and San Andrés, L., 2010, "A Model for Improved Prediction of Force Coefficients in Grooved Squeeze Film Dampers and Oil Seal Rings," *ASME J. Tribol.*, **132**(3), p. 032202.
- [18] San Andrés, L., and Delgado, A., 2012, "A Novel Bulk-Flow Model for Improved Predictions of Force Coefficients in Grooved Oil Seals Operating Eccentrically," *ASME J Gas Turb Pwr*, **134**, p. 052509.
- [19] Stallone, M.J., Gallardo, V., Storace, A.F., Bach, L.J. and Black, G., 1983, "Blade Loss for Transient Dynamic Analysis of Turbomachinery", *AIAA J.* **21**(8), pp. 1134–1138.
- [20] Zhang, S. P., Yan, L. T., and Li, Q. H., 1991, "Development of Porous Squeeze Film Damper Bearings for Improving the Blade Loss Dynamics of Rotor-Support Systems," *ASME J. Vib., Acoust.*, **114**, pp. 347–353.
- [21] Walton, J. F., and Heshmat, H., 1993, "Rotordynamic Evaluation of an Advanced Multi-Squeeze Film Damper-Imbalance Response and Blade-Loss Simulation," *ASME J Gas Turb Pwr*, **115**, pp. 347-352,
- [22] Sun, G., Palazzolo, A., Provenza, A., Lawrence, C., and Carney, K., 2008, "Long Duration Blade Loss Simulations Including Thermal Growths for Dual-Rotor Gas Turbine Engine," *J. Sound Vib.*, **316**, pp. 147–163.
- [23] San Andrés, L., Den, S., and Jeung, S.-H., 2016, "Transient Response of an Open Ends Elastically Supported Squeeze Film Damper: Startup and Steady (Constant) Whirl Frequency Operation," Proceedings of the 2016 ASME Turbo Expo, Seoul, South Korea, ASME Paper No. GT2016-56492.
- [24] Hori, Y, Kato, T., 1990, "Earthquake-Induced Instability of a Rotor Supported by Oil Film Bearings," *ASME J. Vibr. Acoust.*, **112**, pp.160–165.
- [25] Roberts, J. B., Holmes, R., and Mason, P. J., 1986 "Estimation of Squeeze-Film Damping and Inertial Coefficients from Experimental Free-Decay Data," Proceedings of the Institution of Mechanical Engineers, Engineering Sciences Division, **200**(2C), pp. 123-133.

- [26] Ramli, M. D., Roberts, J. B., and Ellis, J., 1987, "Determination of Squeeze Film Dynamic Coefficients from Experimental Transient Data," *ASME J. Tribol.*, **109**, pp. 155–163.
- [27] Lee, A., Kim, B., and Kim, Y., 2006, "A Finite Element Transient Response Analysis Method of a Rotor-Bearing System to Base Shock Excitations Using the State-Space Newmark Scheme and Comparisons With Experiments," *J. Sound Vib.*, **297**(3–5), pp. 595–615.
- [28] San Andrés, L., and Jeung, S.-H., 2016, "Response of a Squeeze Film Damper-Elastic Structure System to Multiple and Consecutive Impact Loads," Proceedings of the 2016 ASME Turbo Expo, Seoul, South Korea, ASME Paper No. GT2016-56695.
- [29] San Andrés, L., and Jeung, S.-H., 2015, "Experimental Performance of an Open Ends, Centrally Grooved Squeeze Film Damper Operating with Large Amplitude Orbital Motions," *ASME J Gas Turb Pwr*, **137**(3), p. 032508.
- [30] Mahecha, P., 2011, "Experimental Dynamic Forced Performance of a Centrally Grooved, End Sealed Squeeze Film Damper," M.S. Thesis, Texas A&M Univ., College Station, TX., USA.
- [31] San Andrés, L., 2012, "Liquid Cavitation in Fluid Film Bearings" Modern Lubrication Theory, Notes 6, Texas A & M University Digital Libraries, <http://repository.tamu.edu/handle/1969.1/93197> [02/05/209].
- [32] Xing, C., and Braun, M., 2010, "Experimental Investigation of the Development of Cavitation in a Squeeze Film Damper," Proceedings of the STLD/ASME 2010 International Joint Tribology Conference, San Francisco, CA, October 17-20, IJTC2010-41144, pp. 1-3.
- [33] Lang, G., F., 1997, "Electrodynamic Shaker Fundamentals," *J. Sound and Vibration*, April
- [34] Lang, G., F., and Snyder, D., 2001, "Understanding the Physics of Electrodynamic Shakers," *J. Sound and Vibration*, October
- [35] Ginsberg, J. H., 2001, *Mechanical and Structural Vibration – Theory and Application*, John Wiley & Sons, New York, pp. 79–85.
- [36] Den, S., 2015, "Analysis of Force Coefficients and Dynamic Pressures for Short-Length ( $L/D=0.2$ ) Open-Ends Squeeze Film Dampers," M.S. Thesis, Texas A&M University, December.
- [37] Fritzen, C. P., 1985, "Identification of Mass, Damping, and stiffness Matrices of Mechanical System," *ASME J. Vib., Acoust.*, **108**, pp. 9-16

## Appendix A. Description of test system and components<sup>9</sup>

This section provides a description of the journal, the bearing cartridge (BC) and the test rig components.

**Journal** Figure A.1 shows a photograph of a feed orifice of diameter  $\phi = 2.5$  mm machined into a hexagonal socket bolt inserted in the journal. The design minimizes the discontinuity in the film land area around the lubricant inlet. The small socket holds  $\sim 0.13$  cm<sup>3</sup> in volume. Hence, the three orifices contain about  $\sim 15\%$  of the lubricant volume in the film land,  $\pi DLc_A = 2.57$  cm<sup>3</sup> for damper A [5]. Note that the journal has a central through hole that acts as a lubricant flow path.

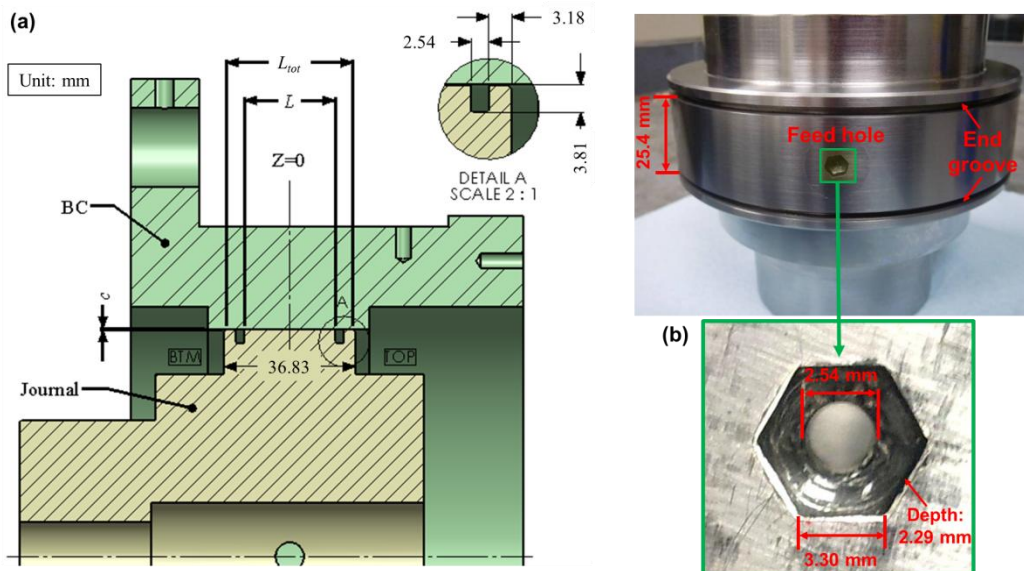


**Figure A.1. (a) Cross-section of SFD journal and BC showing the film land length ( $L$ ) and side end grooves and lip sections. Total wetted length  $L_{tot}$  noted. Photograph of (b) test journal (Material: AISI 1018 carbon steel) and (c) its feed orifice with hex socket [5].**

**Bearing Cartridge** Figure A.2 depicts views of the bearing cartridge (BC). The BC does not have a central groove and the inner surface of the BC creates the outer surface of the squeeze film land with uniform thickness axially. The BC interfaces with four support rods and accommodates instrumentation including REBAM® sensors, load cells, accelerometers and pressure sensors.

<sup>9</sup> Portions of this section reproduce ad-verbatim information described in Ref. [5].

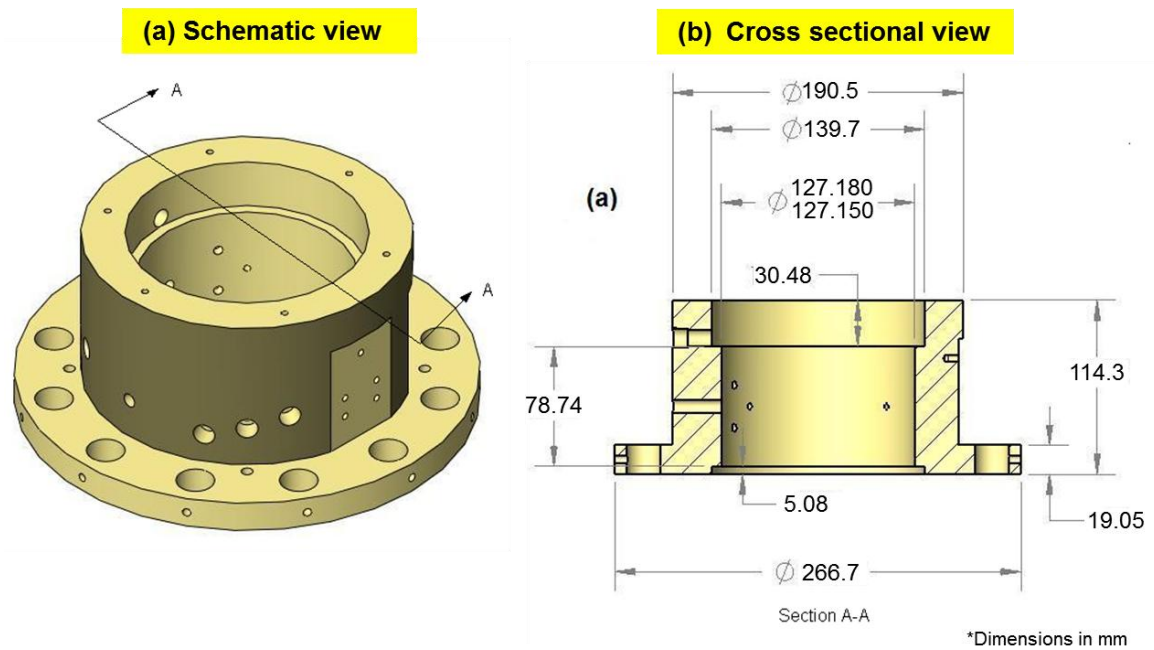


**Figure A.2. Bearing cartridge (a) isometric view, and (b) cross sectional view. (Material: AISI 1018 carbon steel)**

### Measurement of journal outer diameter

The radial clearance of the squeeze film damper is a critical design value. Half of the difference between the journal outer diameter and the BC inner diameter is the nominal clearance. A micrometer (uncertainty  $\pm 2.54 \mu\text{m}$  (0.1 mil)) measures the specified axial planes and angles of the journal and BC as shown in the Figure A.3. Table A.1 lists the measured outer diameter of the journal at each plane and measurements of the BC inner diameter. Note that the micrometer and bore gauge are based on the English unit. The average SFD radial clearance is

$$c_A = \frac{1}{2}(D_{BC\_ID} - D_{J\_OD}) = 254 \mu\text{m} (10 \text{ mil}) \pm 10 \mu\text{m}$$

The average clearance agrees with the design value 10.0 mil. However, note that the journal OD at the axial mid plane (A2) has a bulge  $\sim 1.2$  mil (0.03 mm) larger than the OD top plane (A1) and  $\sim 2.4$  mil (0.06 mm) larger than the bottom plane (A3). Hence, the clearance axial profile is not as uniform as expected. That is, the average radial clearance at the top, mid and bottom planes equal 10.0 mil (0.254 mm), 9.4 mil (0.239 mm) and 10.6 mil (0.269 mm), respectively.

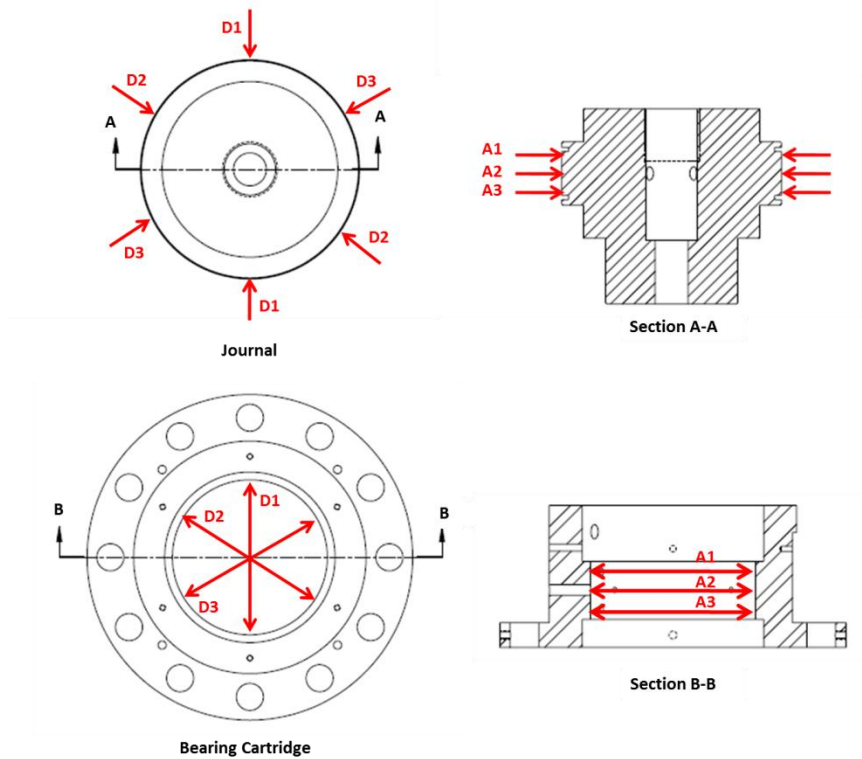


**Figure A.3. Measurement planes for journal outer diameter and BC inner diameter (D planes are radial lines with constant spacing of 45° apart)**

**Table A.1. Journal outer diameter measured at three axial planes and three radial lines.**

Measurement Plane	A-1 (Top) [mm (in)]	A-2 (Mid) [mm (in)]	A-3 (Btm) [mm (in)]
D1 (0-deg)	126.659 (4.9866)	126.695 (4.9880)	126.629 (4.9854)
D2 (60-deg)	126.665 (4.9868)	126.695 (4.9880)	126.634 (4.9856)
D3 (120-deg)	126.647 (4.9861)	126.675 (4.9872)	126.619 (4.9850)
Average	126.657 (4.9865)	126.686 (4.9877)	126.627 (4.9853)
Total Grand Average:		126.657 (4.9865)	mm (in)
Total Uncertainty: +/-		0.010 (0.0004)	mm (in)

Bearing cartridge ID (average) = 127.165 mm (5.0065 in)

Measurement Plane	Radial Clearance [mm (in)]
A-1 (Top)	0.254 (0.0100)
A-2 (Mid)	0.239 (0.0094)
A-3 (Btm)	0.269 (0.0106)
Average Clearance	0.254 (0.0100)

## Appendix B. Measurement of Lubricant Physical Properties

The SFD test rig uses ISO VG 2 grade oil as its lubricant. A Brookfield DV-E rotary viscometer measures the viscosity of a lubricant by measuring the shear (drag) stress on a rotating spindle fully submerged in a lubricant bath. In the apparatus, a water jacket heated the vessel holding the lubricant. The ASTM standard viscosity-temperature relation is

$$\mu = \mu_R e^{-\alpha_v(T-T_R)} \quad (\text{B.1})$$

where  $\mu_R = 2.60$  cPoise (0.377 micro-Reyn) is the measured viscosity at room temperature ( $T_R = 23^\circ\text{C}$ ). The oil viscosity coefficient,  $\alpha_v$ , is given as

$$\alpha_v = \frac{-\ln(\mu_2 / \mu_R)}{(T_2 - T_R)} = 0.016 \frac{1}{^\circ\text{C}} \quad (\text{B.2})$$

where  $\mu_2$  and  $T_2$  are the last viscosity and temperature measurements, respectively.

Figure B.1 shows the current and previous measurements of lubricant viscosity along with the ASTM standard curve fit. The ASTM standard viscosity-temperature relation for the current measurements shows high correlation ( $R^2=0.997$ ). The viscosity measurements throughout 2014 to 2016 show the similar results. Routine inspection of lubricant density and viscosity ensure no significant changes in lubricant properties have occurred.

The measurements give 2.4 cSt (1.90 cPoise) at  $40^\circ\text{C}$  whereas the lubricant manufacturer specifies 2.0 cSt (1.60 cPoise) at the same temperature (see Table C.1). The difference, amounting to  $\sim 16\%$ , is most likely due to entrapped air in the lubricant from numerous tests performed using the identical oil tank during the past research programs. Note that a 10% of entrained air (volume) can increase viscosity by up to 15%. In addition, the blend of multiple batches of the same lubricant brand purchased at various times could also explain the difference in viscosity.

At ambient condition of  $23^\circ\text{C}$ , the lubricant density was also determined, by weighing a known volume of lubricant oil. The oil density obtained is  $\rho=800 \text{ kg/m}^3$ .

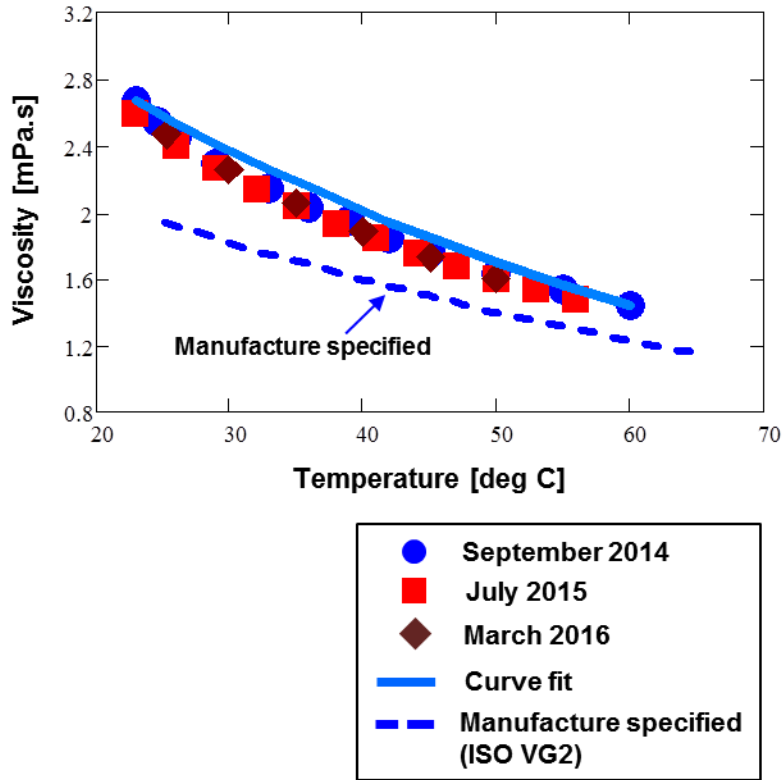


Figure B.3. ISO VG 2 measured viscosity versus temperature for three separate measurements.

Table B.1. Mobil Velocite™ No 3 (ISO VG 2) Manufacturer specification [B1]

Mobil Velocite Oil Numbered Series No 3 (ISO VG 2)	
cSt @ 40°C	2.1
cSt @ 100°C	0.95
Pour Point, °C	-36
Flash Point, °C	84
Density @ 15° C, kg/L	0.802

## References

- [B1] “Mobil Velocite™ No 3 (ISO VG 2) Manufacturer specification sheet”, Hydraulic oils Typical Properties, Mobil, Accessed October 2013, [http://www.mobil.com/USAEnglish/Lubes/PDS/GLXXENINDMOMobil\\_Velocite\\_Oil\\_Numbered.aspx](http://www.mobil.com/USAEnglish/Lubes/PDS/GLXXENINDMOMobil_Velocite_Oil_Numbered.aspx)

## Appendix C. Identification of (Dry) Test System Structure Parameters

Circular orbit load tests are performed with a dry system (without lubricant) to identify the test system structural parameters [structural stiffness ( $K_s$ ), system remnant mass ( $M_s$ ), and structural damping ( $C_s$ )]. Two electromagnetic shakers deliver single frequency loads, 90° out of phase, over a designated frequency range of 10 – 100 Hz. The amplitude of journal motion is set to  $r/c_A=0.05$ .

The Instrumental Variable Filter (IVF) method [37] estimates the force coefficients for the dry system ( $K_s$ ,  $C_s$ ,  $M_s$ ) from the mechanical impedances

$$H_{XX,YY} = [K_s - \omega^2 M_s + i\omega C_s]_{XX,YY} \quad (C.1)$$

where  $\omega$  is the excitation frequency. Note that the real and imaginary parts of an impedance ( $H$ ),

$$\text{Re}(H) = K_s - \omega^2 M_s \quad \text{and} \quad \text{Im}(H) = C_s \omega \quad (C.2)$$

reveal the structural stiffness ( $K_s$ ) and system remnant mass ( $M_s$ ) and an (assumed) viscous damping coefficient ( $C_s$ ).

Table C.1 lists the identified test system structural parameters ( $K_s$ ,  $C_s$ ,  $M_s$ ) over a excitation frequency range from  $f_{\text{start}}=10$  to  $f_{\text{end}}=100$  Hz. The results show the test system is orthotropic with little structural cross-coupling. The structure stiffnesses are  $K_{SX}=12.0$  MN/m and  $K_{SY}=11.9$  MN/m along the  $X$  and  $Y$  directions..

The damping ratios are  $< \sim 4\%$ , which are typical of steel structures. However, note that the damping is most likely not viscous in nature, as Fig. C.1 depicting the imaginary part of the test impedances,  $\text{Im}(H)$ , most vividly demonstrates.

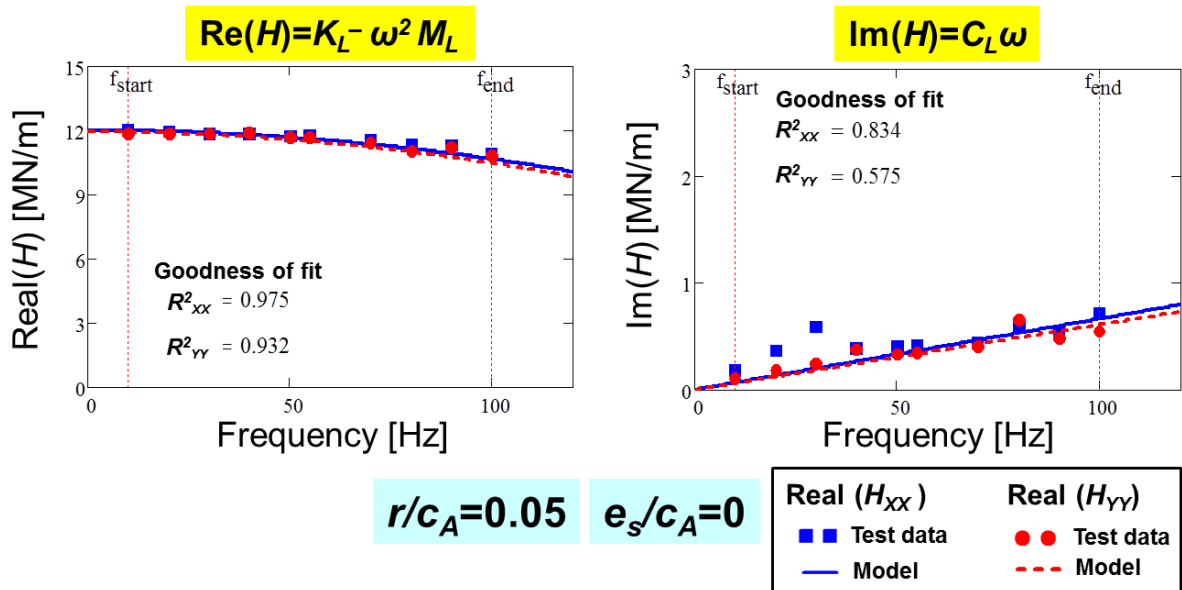
Note that an accurate measurement of the structural stiffness is required to distinguish the SFD reaction forces from the reaction forces arising from the support structure; albeit the SFD dynamic force coefficients are independent of the structural stiffness of the BC [3].

Figure C.1 shows the experimental data and physical model fits in real and imaginary parts of  $H$ . The goodness of physical model fits shows  $R^2 > 0.9$  for the real part of  $H$  implying the model represent well the test structural system. On the other hand, the correlation for the imaginary part of  $H$  are relatively low indicating the structural damping ( $C_s$ ) is not of viscous type.

**Table C.1. System structural parameters obtained from circular orbit tests under a dry condition (no lubricant). Parameters identified in frequency range 10 – 100 Hz. Orbit amplitude  $r/c_A=0.05$  and static eccentricity  $e_s/c_A=0.0$ .**

Structural parameter			Direct		Cross-coupled	
			XX	YY	XY	YX
Stiffness	$K_s$	[MN/m]	12.0	11.9	-0.31	-0.25
Damping	$C_s$	[kN.s/m]	0.6	0.5	-0.05	-0.02
Mass	$M_s$	[kg]	3.4	3.7	0.17	0.27
System Mass	$M_{BC}$	[kg]	15.15			
Natural Frequency	$f_n$	[Hz]	128	126		
Damping Ratio	$\zeta_n$		0.020	0.018		

Eq. (18) is based on the transient free-response of an underdamped ( $\zeta < 1$ ) one degree of freedom mechanical system, where  $\zeta = \frac{C}{2\sqrt{K_s M}}$  is the damping ratio and  $\omega_n = \sqrt{\frac{K_s}{M}}$  is the system natural frequency. Above,  $M = M_{BC} + M_{SFD}$ , where  $M_{BC}=15.15$  kg and  $M_{SFD}$  is the SFD added mass, and  $K_s = 12.0$  MN/m is the support structural stiffness.



**Figure C.1. Real and imaginary parts of direct impedances ( $H$ ) obtained from circular orbit test on a dry (without lubricant) system.**

## Appendix D. Uncertainty in identified force coefficients<sup>10</sup>

This section outlines the calculation of uncertainty in identified SFD force coefficients. The total uncertainty consists of a bias (instrument) uncertainty, a precision (curve fit) uncertainty and measurement variability. These types of uncertainty are outlined, along with the combination of bias, precision and variability into total uncertainty for each force coefficient ( $K$ ,  $C$ ,  $M$ )<sub>SFD</sub>. Bias, precision, variability and total uncertainty denoted as  $B$ ,  $P$ ,  $V$  and  $U$ , respectively.

### Bias uncertainty

The data acquisition (DAQ) board has a rated resolution of  $B_{DAQ} = 0.1\%$  in the recording of voltage [D1]. The DAQ board samples 16,384 samples/second, stores 4096 samples and giving an uncertainty in the output frequency of  $B_{\omega} = 1\text{Hz}$  for the entire frequency range [D1]. This is equivalent to  $B_{\omega} = 10\%$  at the lowest frequency of 10 Hz,  $B_{\omega} = 1\%$  at the largest frequency of 100 Hz, and an average of  $B_{\omega} = 2.9\%$  across the entire frequency range. Note, the following analysis considers the average  $B_{\omega}=2.9\%$ , because the force coefficients are best fit over the entire range. Note that actual uncertainty may be less than 2.9% since a Fourier series is used to express the recorded data in the frequency domain.

The uncertainty of  $X$  and  $Y$  – REBAM® (displacement) sensors are  $B_x = 0.04\%$  and  $B_y = 0.04\%$ , respectively. The load cell uncertainty is  $B_{LOAD} = 0.01\%$ . With these individual uncertainties, the propagation of uncertainty into the measurements of displacement and force, respectively, are

$$B_{DISP} = \sqrt{(B_{REBAM})^2 + (B_{DAQ})^2} = 0.11\% \quad (\text{D.1})$$

$$B_{FORCE} = \sqrt{(B_{LOAD})^2 + (B_{DAQ})^2} = 0.1\% \quad (\text{D.2})$$

Knowledge of frequency domain relations  $K \sim F/D$ ,  $C \sim (F/D)\omega$ , and  $M \sim (F/D)\omega^2$  aids to determine the total bias uncertainty in force coefficients as

$$B_K = \sqrt{(B_{DISP})^2 + (B_{FORCE})^2} = 0.15\% \quad (\text{D.3})$$

$$B_C = \sqrt{(B_{DISP})^2 + (B_{FORCE})^2 + (B_{\omega})^2} = 2.9\% \quad (\text{D.4})$$

---

<sup>10</sup> Portions of this appendix reproduce ad-verbatim information presented in Ref.[36].

$$B_M = \sqrt{(B_{DISP})^2 + (B_{FORCE})^2 + (2 \cdot B_\omega)^2} = 5.8\% \quad (D.5)$$

Recall, determination of the SFD force coefficient requires subtraction of dry system coefficients from lubricated system coefficients, i.e.

$$(\mathbf{K}, \mathbf{C}, \mathbf{M})_{SFD} = (\mathbf{K}, \mathbf{C}, \mathbf{M}) - (\mathbf{K}, \mathbf{C}, \mathbf{M})_S \quad (D.6)$$

Therefore, propagation of the bias uncertainty from two measurements into the SFD coefficient's bias is

$$B_{K_{SFD}} = \sqrt{(B_{K_S})^2 + (B_K)^2} = 0.21\% \quad (D.7)$$

$$B_{C_{SFD}} = \sqrt{(B_{C_S})^2 + (B_C)^2} = 4.1\% \quad (D.8)$$

$$B_{M_{SFD}} = \sqrt{(B_{M_S})^2 + (B_M)^2} = 8.2\% \quad (D.9)$$

### Precision uncertainty

Precision uncertainty deals with the repeatability of measurements. However, only one set of tests were conducted at each test condition ( $r, e_s$ ). This set of tests consisted of individual tests at several pre-selected frequencies ( $\omega$ ). Plotting the real and imaginary part of the measured impedance versus frequency and using an IVFM curve fit (variation of least squares) gives plots as those shown in Figure E.1. The stiffness coefficient ( $K$ ) is estimated as the  $Y$ -intercept and the mass coefficient ( $M$ ) are estimated as the curvature of the real part of the measured mechanical impedance. The slope of the imaginary part of the measured mechanical impedance is the estimated damping coefficient ( $C$ ).

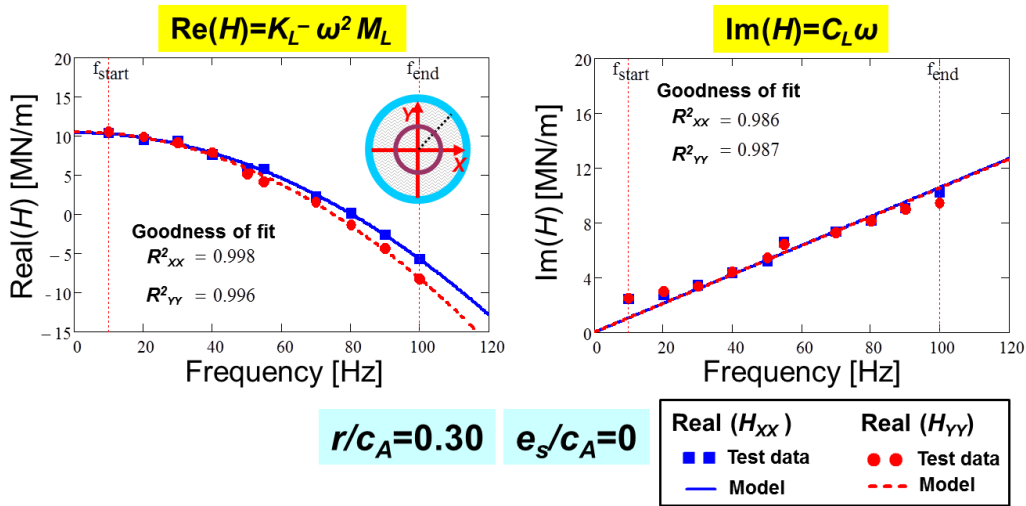


Figure D.1. Plots real (a) and imaginary (b) parts of mechanical impedance versus frequency ( $\omega$ ). Curve fit and measured data shown.

For the estimation of precision uncertainty in a single measurement, Ref. [D2] gives

$$P = 1.96 \cdot S \quad (D.10)$$

where  $S$  is the estimated standard deviation based upon engineering knowledge. Ref [D3] gives relations for estimated standard deviation of the intercept and slope of a least squares fit line as

$$S_{Intercept} = \sqrt{\frac{1}{N(N-2)} \frac{1-r^2}{r^2}} \quad (D.11)$$

$$S_{Slope} = \sqrt{\frac{1}{(N-2)} \frac{1-r^2}{r^2}} \quad (D.12)$$

where  $N$  is the number of points used for the curve fit and  $r^2$  is the curve fit correlation. Using the relations given in E.11 and E.12 with  $N=10$  and  $r^2=0.95$ , the propagation into the uncertainty of SFD coefficients gives

$$P_{K_{SFD}} = 1.6\% \quad (D.13)$$

$$P_{C_{SFD}} = 5.3\% \quad (D.14)$$

$$P_{M_{SFD}} = 9.9\% \quad (D.15)$$

### **Uncertainty due to variability**

Uncertainty from variability deals with the repeatability of measurements. In an effort assess the repeatability of the identified  $K$ ,  $C$ ,  $M$  coefficients, several of the operating conditions included three sets of experiments to calculate the standard deviation of the force coefficient among the three experiments. Note that a weighted average (a function of  $r/c$  and  $e_s/c$ ) of the measured standard deviations delivered those for the operating conditions without three experiments.

The estimation of uncertainty pertaining to the variability of the force coefficients from the averaging of multiple test results is [D2]:

$$\varphi_{var} = t \cdot S \quad (D.16)$$

where  $t$  is the student's  $t$ -distribution value 1.96 corresponding to a 95% confidence interval [D2], and  $S$  is the precision index of the averaged result and follows given by Ref. [D2]:

$$V_{K_{SFD}} = \frac{\varphi_{K_{XX SFD}}}{K_{XX SFD}} = 0.4\% \quad (D.17)$$

$$V_{C_{SFD}} = \frac{\varphi_{C_{XX SFD}}}{C_{XX SFD}} = 3.3\% \quad (D.18)$$

$$V_{M_{SFD}} = \frac{\varphi_{M_{XX SFD}}}{M_{XX SFD}} = 6.1\% \quad (D.19)$$

### **Total uncertainty**

The total uncertainty in each SFD force coefficients are

$$U_{K_{SFD}} = \sqrt{(B_{K_{SFD}})^2 + (P_{K_{SFD}})^2} = 2.3\% \quad (D.20)$$

$$U_{C_{SFD}} = \sqrt{(B_{C_{SFD}})^2 + (P_{C_{SFD}})^2} = 9.2\% \quad (D.21)$$

$$U_{M_{SFD}} = \sqrt{(B_{M_{SFD}})^2 + (P_{M_{SFD}})^2} = 17.4\% \quad (D.22)$$

### **References**

- [D1] “NI cDAQ – 917x User Manual,” User manual for NI CompactDAQ9171/9174/9178 USB Chassis, National Instruments, July 2011, Appendix A. Specifications.
- [D2] Beckwith, T., Marangoni, R., and Lienhard, J. 1993, “Mechanical Measurements”, Prentice Hall, 5<sup>th</sup> edition, pp. 82
- [D3] Coleman, H.W., and Steele, G.W., 1998, *Experimentation and Uncertainty Analysis for Engineers*, John Wiley & Sons, New York.